

105577
7-356
P-221

X-Ray Attenuation Measurements for High-Temperature Materials Characterization and In-Situ Monitoring of Damage Accumulation

George Y. Baaklini
Lewis Research Center
Cleveland, Ohio

March 1992



(NASA-TM-105577) X RAY ATTENUATION
MEASUREMENTS FOR HIGH-TEMPERATURE MATERIALS
CHARACTERIZATION AND IN-SITU MONITORING OF
DAMAGE ACCUMULATION Ph.D. Thesis - Cleveland
State Univ., 1991 (NASA) 221 p

N92-25996

Unclas
G3/24 0092886

**X-RAY ATTENUATION MEASUREMENTS FOR HIGH-TEMPERATURE
MATERIALS CHARACTERIZATION AND IN-SITU MONITORING OF DAMAGE
ACCUMULATION**

GEORGE Y. BAAKLINI

National Aeronautics and Space Administration
Lewis Research Center
Cleveland, Ohio 44135

ABSTRACT

**ORIGINAL CONTAINS
COLOR ILLUSTRATIONS**

The scope of this dissertation is to develop and apply x-ray attenuation measurement systems that are capable of 1) characterizing density variations in high-temperature materials, e.g., monolithic ceramics, ceramic and intermetallic matrix composites and 2) noninvasively monitoring damage accumulation and failure sequences in ceramic matrix composites under room temperature tensile testing.

This dissertation results in the development of 1) a point scan digital radiography system and 2) an in-situ x-ray material testing system. The former is used to characterize silicon carbide and silicon nitride specimens and the latter is used to image the failure behavior of silicon carbide fiber reinforced reaction bonded silicon nitride matrix composites. Further, state of the art x-ray computed tomography is investigated to determine its capabilities and limitations in characterizing density variations of subscale engine components, e.g., a silicon

carbide rotor, a silicon nitride blade, and a silicon carbide fiber reinforced beta titanium matrix rod, rotor, and ring. Microfocus radiography, conventional radiography, scanning acoustic microscopy, and metallography are used to substantiate the x-ray computed tomography findings.

Point scan digital radiography is a viable technique for characterizing density variations in monolithic ceramic specimens. But it is very limited and time consuming in characterizing ceramic matrix composites. Precise x-ray attenuation measurements, reflecting minute density variations, are achieved by photon counting and by using micro collimators at the source and the detector. X-ray computed tomography is found to be a unique x-ray attenuation measurement technique capable of providing cross sectional spatial density information in monolithic ceramics and metal matrix composites. X-ray computed tomography is proven to accelerate generic composite component development.

Radiographic evaluation before, during and after loading shows the effect of preexisting volume flaws on the fracture behavior of composites. Results from one-ply, three-ply, five-ply and eight-ply ceramic composite specimens, shows that x-ray film radiography can monitor damage accumulation during tensile loading. Matrix cracking, fiber-matrix debonding, fiber bridging, and fiber pullout are imaged throughout the tensile loading of the

specimens. Further in-situ film radiography is found to be a practical technique for estimating interfacial shear strength between the silicon carbide fibers and the reaction bonded silicon nitride matrix. It is concluded that pre-test, in-situ, and post-test x-ray imaging can provide for greater understanding of ceramic matrix composite mechanical behavior.

ACKNOWLEDGEMENTS

I thank my advisor Dr. John H. Hemann for the helpful advice and the supportive encouragement. Thanks are also extended to the advising committee members: Dr. Paul X. Bellini, Dr. Louis J. Ghosn, Dr. James A. Lock, and Mr. Alex Vary for the beneficial suggestions and the constructive comments.

The CT evaluation support that Mr. Robert N. Yancey and Mr. Michael E. Hughes from Advanced Research and Applications Corporation (at Wright-Patterson Air Force Base under contract F33615-88-c-2823) is gratefully acknowledged. I am grateful to Mr William J. Doehnert for the helpful discussions and for supplying Pratt and Whitney metal matrix composites hardware. I am also grateful to all the individuals at NASA Lewis Research Center, at Sverdrup Technology Inc., and at the U.S. Army Aviation Systems Command, who provided helpful assistance.

| TABLE OF CONTENTS | | Page |
|---|--|------|
| ABSTRACT | | i |
| ACKNOWLEDGEMENTS | | iv |
| TABLE OF CONTENTS | | v |
| SYMBOLS AND ABBREVIATIONS | | xi |
| I. INTRODUCTION | | 1 |
| II. REVIEW, DEFINING NDE REQUIREMENTS AND GOALS FOR | | |
| CHARACTERIZING HIGH-TEMPERATURE MATERIALS | | 8 |
| Introduction | | 8 |
| Materials and Subscale Engine Components | | 8 |
| Silicon carbide rotor | | 8 |
| Silicon nitride disks and blade | | 9 |
| Silicon carbide fiber reinforced | | |
| silicon nitride | | 10 |
| Silicon carbide fiber reinforced titanium base | | |
| composites | | 11 |
| Novel NDE Techniques | | 12 |
| X-Ray film radiography and microradiography | | 12 |
| Digital x-radiography | | 23 |
| X-ray Computed Tomography | | 28 |
| Ultrasonics | | 36 |
| NDE Role in Materials Development and | | |
| Characterization | | 40 |
| Monolithic Ceramics | | 41 |
| Composites | | 43 |

| | | |
|-------|--|-----|
| III. | POINT SCAN DIGITAL RADIOGRAPHY | 45 |
| | Introduction | 45 |
| | System Buildup | 46 |
| | Results and Discussion | 72 |
| | Conclusion | 89 |
| IV. | CHARACTERIZATION OF CERAMIC DISKS AND ENGINE COMPONENTS USING X-RAY COMPUTED TOMOGRAPHY | 91 |
| | Introduction | 91 |
| | Materials and Experimental Procedures | 92 |
| | Results and Discussion | 136 |
| | Conclusion | 144 |
| V. | CHARACTERIZATION OF MMC SUBSCALE ENGINE COMPONENTS USING X-RAY COMPUTED TOMOGRAPHY | 145 |
| | Introduction | 145 |
| | Materials and Experimental Systems | 147 |
| | Results and Discussion | 153 |
| | General Discussion | 179 |
| | Conclusion | 182 |
| VI. | IN-SITU X-RAY MONITORING | 183 |
| | Introduction | 183 |
| | Experimental | 185 |
| | Results | 193 |
| | Discussion | 227 |
| | Conclusion | 231 |
| VII. | GENERAL DISCUSSION | 233 |
| VIII. | CONCLUSIONS | 238 |

| | | |
|-----|--|-----|
| IX. | FUTURE RESEARCH | 242 |
| X. | BIBLIOGRAPHY | 245 |
| XI. | APPENDICES | |
| | APPENDIX A: SLURRY-PRESSING OF NITRIDES | 257 |
| | APPENDIX B: SINTERING OF NITRIDES | 260 |
| | APPENDIX C: FABRICATION OF INJECTION-MOLDED SINTERED SILICON NITRIDE BLADE | 261 |
| | APPENDIX D: FABRICATION OF SCS-6 FIBER REINFORCED MMC ROD, RING, AND ROTOR | 263 |
| | APPENDIX E: X-RAY RADIOGRAPHY RELATED TOPICS | 267 |

SYMBOLS AND ABBREVIATIONS

Symbols are defined where they first appear in the text.

Following are most of the symbols for easy reference:

| | |
|----------------|--|
| // | parallel |
| $[0]_1$ | One-ply unidirectional composite |
| $[0]_3$ | Three-ply unidirectional composite |
| $[0]_5$ | Five-ply unidirectional composite |
| $[0]_8$ | Eight-ply unidirectional composite |
| τ_f | Interfacial shear stress |
| σ_E | Engineering stress |
| $\sigma(x)$ | Quantum noise |
| ψ | Energy flux density |
| λ | X-ray wavelength |
| ϵ | Axial strain |
| μ | Total linear attenuation coefficient |
| μ/ρ | Total mass attenuation coefficient |
| $(\mu/\rho)_c$ | Total mass attenuation coefficient of a compound |
| ρ | Density |
| σ_c^m | Composite stress at first matrix cracking |
| A | Atomic weight |
| a | Source-to-object distance |
| b | Object-to-detector distance |
| C | Radiographic film contrast |
| c | Velocity of light |
| C_{res} | Resultant radiographic contrast |

| | |
|-----------------------------|--|
| C_{sub} | Subject radiographic contrast |
| D_f | Diameter of fiber |
| E | Modulus |
| E_{elect} | Energy of electromagnetic field |
| E_m | Modulus of matrix |
| E_f | Modulus of fiber |
| E_{pc} | Primary modulus of composite |
| $E_{(\text{rom})c}$ | Rule of mixtures composite modulus |
| f_{elect} | Frequency of electromagnetic field |
| G_r | Film gradient |
| h | Plank's constant |
| I | X-ray tube current |
| M | Magnification |
| N | Number of transmitted photons |
| N_o | Number of incident photons |
| N_A | Avogadro's number |
| N_{eff} | Effective number of photons |
| N_p | Number of primary photons |
| N_s | Number of scattered photons |
| R | Geometric resolution |
| s | Total cross section atomic attenuation coefficient |
| S_{fs} | Focal spot size |
| SNR | Signal to noise ratio |
| $\text{SNR}_{\text{ideal}}$ | Ideal SNR |
| U_g | Geometric unsharpness |
| V | X-ray tube voltage |

| | |
|-----------|--|
| V_f | Fiber volume fraction |
| V_m | Matrix volume fraction |
| W_i | Proportion by weight of the i th constituent |
| x | Matrix spacing |
| \bar{X} | Mean crack spacing |
| X_m | Material thickness |
| Z | Atomic number |
| AGT | Advanced gas turbine |
| ASDR | Area scan digital radiography |
| ATTAP | Advanced turbine technology applications project |
| BSE | Back scattered electron |
| CATE | Ceramic application in turbine engines |
| CT | Computed tomography |
| CMC | Ceramic matrix composite |
| DR | Digital radiography |
| DQE | Detection quantum efficiency |
| EDAX | Energy dispersive analysis x-ray |
| GPIB | General purpose interface bus |
| HITEMP | NASA high temperature material's program |
| ID | Inside diameter |
| IMC | Intermetallic matrix composite |
| IXMTS | In-situ x-ray and materials testing system |
| LAM/DE | Laminography/dual energy |
| LES | Light-weight engine structure |
| LSDR | Line scan digital radiography |
| MMC | Metal matrix composite |

| | |
|------|--------------------------------|
| NDE | Nondestructive evaluation |
| OD | Outside diameter |
| PSDR | Point scan digital radiography |
| SN | Silicon nitride |
| SC | Silicon carbide |
| XCT | X-ray computed tomography |

CHAPTER I

INTRODUCTION

High-temperature engine materials e.g., ceramics, intermetallic matrix composites (IMCs), metal matrix composites (MMCs), and ceramic matrix composites (CMCs) are being developed mainly for aeronautic propulsion components (HITEMP Review 1988). High-temperature materials offers good oxidation resistance, low density, and high-temperature strength, in addition to operating at significantly higher temperatures than metals and superalloys. The use of these composites reduces engine cooling requirements, engine weight, and consequently fuel consumption (HITEMP Review 1989). Payoffs in engine performance and cost savings are expected. MMCs and IMCs can be used over the temperature range of 800 to above 1370 °C (1475 to above 2500 °F), CMCs can be used in the range of 1100 °C (2000 °F) to 1650 °C (3000 °F). IMCs and MMCs are targeted as compressor and turbine disks materials whereas CMCs are targeted for

extreme high temperature applications such as turbine vanes, blades, and disks (Stephens 1990).

Monolithic structural ceramics are limited by detrimental inherent defects (Evans et al. 1977; Evans 1984), low fracture toughness, low strain tolerance, and reliability assurance (Harper 1983; Baaklini 1987; Structural Ceramics 1986). In order to overcome the limitations of monolithic structural ceramics, CMC development is being pursued aggressively to improve fracture toughness and strength, and to minimize the sensitivity to detrimental flaws.

Limiting factors for IMCs include fiber-matrix coefficients of thermal expansion (CTE) mismatch, analytical modeling in conjunction with composite development, and ductility/toughness of the matrix (Stephens 1990). Limiting factors for CMCs include fiber-matrix interface, development of high strength and small diameter fibers, and analytical modeling for life prediction. In addition to developing high CTE fibers for IMCs and small diameter/high strength fiber for CMCs, one critical issue is to identify failure and damage mechanisms so that better modeling and life prediction can be done on these emerging composites.

Progress in the processing of high temperature materials has not been matched by detailed mechanical and nondestructive testing efforts which are needed to support designing new materials and related generic components. A

definite need exists for experiments that identify the failure mechanisms and follow the damage progression. Upgrading the capabilities of existing NDE techniques for characterizing density variations and recognizing detrimental defects in the new material systems is also needed. Innovative experiments that monitor specimens under loading are needed before mechanical models can be fully developed.

The processing of new and innovative high-temperature materials requires concurrent development of new and innovative nondestructive evaluation (NDE) technologies. Sanders and Baaklini (1988) demonstrate that nondestructive materials characterization and proper feed-back help optimize the processing procedures. Nondestructive quality inspection where specific ASTM standards procedures are applied assures materials reliability. Vary (1991) suggests that new NDE standards and methodologies should mature simultaneously with advancements in materials development. Similarly, manufacturing of high-temperature generic engine component calls for simultaneous development of creative NDE techniques and for upgrading existing NDE technologies.

The purpose of this dissertation is to develop and apply x-ray attenuation measurement systems that are capable of characterizing density variations and of monitoring damage accumulation and failure mechanisms in high temperature materials and components. This work should

accelerate generic monolithic and composite components development and provide for greater understanding of related mechanical behavior.

Many researchers have evaluated monolithic ceramic coupon type materials by using conventional and advanced NDE technologies but very little work has been done in the high temperature composite areas (Vary and Klima 1991). Nuclear magnetic resonance imaging is a feasible NDE modality for quantifying organics in injection-molded green (unfired) ceramics (Ellingson et al. 1987a and 1989; Gopalsami et al. 1990). Automated visual examinations (Bowman and Batchelor 1985) are routinely used to detect surface-connected anomalies in fired objects. Conventional film radiography and immersion scanning ultrasonics are methodically used to detect sizeable (greater than 0.5 mm in diam.) surface and volume flaws in specimens and components. Flaws down to 25 μm in diameter can be resolved by acoustic microscopy and microfocus radiography (Nikoonahad 1984; Baaklini et al. 1986a, 1986b, 1987, 1990), scanning laser acoustic microscopy (Roth et al. 1986 and 1987), and x-ray tomography (Yancey et al. 1990 and 1991) under stringent conditions e.g., moderate material thickness and good surface finish. Ultrasonic attenuation and velocity (Generazio 1985; Generazio et al. 1987; Baaklini et al. 1989), acousto-ultrasonics (Kautz and Lerch 1991a; Kautz and Bhatt 1991b; Vary 1978 and 1988; Hemann and Baaklini 1986), backscatter

ultrasonics (Goebbels 1980) were successfully used to quantitatively characterize the microstructure and to experimentally deduce correlations between NDE parameters and mechanical and physical properties of materials.

NDE of emerging subscale engine components is very limited. The ceramic application in turbine engines (CATE 1981 and 1984) programs included NDE applications on blades and rotors. The advanced gas turbine technology project (AGT 1988) and the advanced turbine technology applications project (ATTAP 1990) also include NDE applications for material processing optimization. NDE capabilities are being uncovered in high temperature composite components as NDE programs are integrated early on in the development program. But the role of NDE is still not clearly defined.

Defining NDE requirements and goals for high-temperature materials is reviewed and assessed in chapter II. Chapter II briefly describes the fabrication of selected high-temperature materials, concisely surveys candidate novel NDE techniques for characterizing emerging materials, and succinctly explores the role of NDE in materials development.

In chapter III the buildup of a point scan digital radiography system is described. Objectives for building this system are explained. Capabilities and limitations of this system for materials characterizations are defined.

In chapter IV an extensive study of NDE capabilities and limitations for characterizing monolithic ceramic components is pursued. The work in this chapter is a step forward toward validating x-ray computed tomography (XCT) results via metallography, radiography, and ultrasonics. This effort represents an extension of the early effort (CATE 1984; AGT 1988) in NDE of ceramic monolithic components.

In chapter V the capabilities and limitations of XCT for characterizing MMC specimen and subscale engine components are defined. This work provides new data and composite calibration data, helps identify fabrication related problems, and guides geometric and stiffness modeling of composite constituents.

Proposed CMC components are not yet available. However, related CMC specimens are obtainable and procurable. CMC mechanical behavior is not well understood. In chapter VI in-situ x-ray monitoring, a new and unique capability, noninvasively monitors damage accumulation and failure sequences in unidirectional silicon carbide fiber reinforced reaction bonded silicon nitride matrix (SiC/RBSN). This work provides greater understanding of SiC/RBSN mechanical behavior, and consequently helps in the validation of newly developing analytical models.

Chapters VII and VIII bind, discuss, and conclude the dissertation as a whole. Chapter IX highlights future

research needed to advance state-of-the-art NDE technology in order to fulfill emerging technology requirements in high-temperature materials and advanced engine component development.

CHAPTER II

REVIEW, DEFINING NDE REQUIREMENTS AND GOALS FOR CHARACTERIZING HIGH-TEMPERATURE MATERIALS

Introduction

In this chapter the fabrication of selected high-temperature materials and related components are briefly described. Selected NDE techniques are concisely surveyed. The role of NDE in materials development is succinctly explored.

Materials and Subscale Engine Components

Silicon carbide rotor

The turbine rotor was fabricated at Sohio via injection molding of sintered alpha silicon carbide material (AGT 1988). Carbide injection molding involves plastic forming of mixtures of powder and organic additives (binders) which deform under pressure and heat into desired complex shapes

(Richerson 1982). The binders have low enough viscosity to allow flow of the mixture at specified temperatures and pressures. The viscous material is forced into a shaped tool cavity until the cavity is filled and the material has fused together under pressure and temperature to produce the homogeneous part. The major problems in plastic-forming processes are binder removal before firing and achieving high enough green density. Inadequate removal of binders results in cracking, substantial shrinkage, bloating, and nonuniform densification. Hot isostatic pressing (HIP) was used to improve microstructural homogeneity. Pores in the large hub area of the rotor are the flaws which dominate failure.

Silicon nitride disks and blade

The silicon nitride composition for the disks contains 5.8 wt % SiO_2 and 6.4 wt % Y_2O_3 . Disks were slurry-pressed (Sanders et al. 1989) under 9 MPa, dried, and cold isostatically pressed under 414 MPa to increase the green density (Appendix A). Thereafter, the disks were sintered (Appendix B) at 2140 °C for 3 hours under 5 MPa N_2 . Boron nitride setters separated the disks from each other during sintering. X-ray diffractometer scans of polished surface of disks show beta silicon nitride to be the only detectable crystalline phase.

The silicon nitride blade was injection molded and sintered by General Telephone and Electronics (GTE) laboratories (CATE report 1981 and 1984). The process routing outline is shown in Appendix C.

Silicon carbide fiber reinforced silicon nitride

The composites are consolidated by hot pressing and reaction bonding processes. Fiber mats are prepared by winding the fiber at a specified spacing on a cylindrical mandrel, spraying polymer binders to reserve fiber spacing, and cutting the mats to required size. Matrix tapes are prepared by blending the silicon powder with a polymer binder, then the mixture is rolled into tapes of specified thickness. Setting the fiber spacing and matrix mat thicknesses controls the fiber volume fraction of the composite. Alternate layers of silicon tapes and fiber mats are stacked in a metal die and pressed in vacuum hot-press between 800 to 1000 °C for one hour at pressures between 50 to 100 MPa. Finally, the SiC/Si preforms are heat treated in nitrogen between 1000 to 1400 °C for up to 100 hours to convert silicon to silicon nitride as the matrix material. Composite panels containing 9 to 24% fiber volume fraction are fabricated with typical dimensions of 125 by 50 by 2 mm. Only one 8-ply specimen is nitrided at 1350 °C in $N_2 + 4\% H_2$ for 80 hours in comparison to all

other specimens which are nitrided at 1200 °C in N₂ for 40 hours.

RBSN matrix was chosen because dimensional changes do not occur during nitridation (it is a matter of filling in the pores). This makes it an ideal matrix for complex shape component development. Further, the technique results in high purity matrix material which possesses good high-temperature properties with high resistance to creep.

Silicon carbide fiber reinforced titanium base composites

The fabrication procedures of the fiber reinforced rod and ring are schematically shown in Appendix D (Figs. D.1 and D.2). A bundle of SCS-6 (142 μm in diameter) filament is spirally wound with titanium ribbon, then the filament bundle is inserted in a titanium alloy C cylinder to fabricate the rod and in a slotted alloy C disk to fabricate the ring. Titanium caps are welded to each end of the cylinder and to the top of the slotted disk for sealing. The sealed cylinder and disk are consolidated by hot isostatic pressing. The consolidated composite cylinder and disk are then machined into a rod and a ring.

The fabrication procedures of the subscale integrally bladed rotor are schematically shown in figure D.3 of Appendix D. Powder coated SCS-6 fibers are transversely wound and consolidated in hard (graphite type) tooling to make the

composite ring. Thereafter the ring is inserted into a slotted disk, capped and vacuum-hot-pressed (VHP) bonded. The bonded composite disk is then machined into an integrally bladed rotor.

Novel NDE Techniques

In this section, x-ray attenuation measurement and selected ultrasonic measurement are the only NDE techniques stressed because of their ability to characterize the densified materials under consideration.

X-Ray film radiography and microfocus radiography

X-rays, i.e., photons are a form of electromagnetic radiation with wavelengths ranging from 10 \AA to 0.0001 \AA (Appendix E). Roentgen discovered x-rays in 1895. The energy E of a photon is proportional to the frequency f_{elect} of the electromagnetic field by $E_{\text{elect}} = hf_{\text{elect}}$, where h is the Plank's constant. The minimum wavelength, λ_{min} , of the x-ray is given by $c/f_{\text{elect}} = ch/E_{\text{elect}} = ch/eV$, where c is the velocity of light, e is the charge on the electron, and V is the voltage across the x-ray tube:

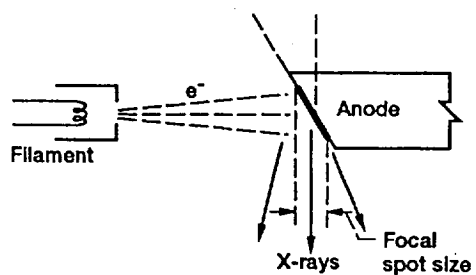
$$\lambda_{\min} (\text{in } \text{\AA}) = \frac{12395}{V(\text{in volts})} \quad (2.1)$$

X-rays of different energies are emitted from an anode (Fig. 2.1 (a)) creating a continuous x-ray spectrum as shown in figure 2.2 (a). The intensity, (energy flux density in $\text{J/m}^2=\text{W/m}^2$) of x-rays, is defined as the number of photons per unit of area multiplied by their energy. The energy flux density is proportional to the tube current, I , to the atomic number of the anode material, Z , and to the square of the tube voltage, V^2 :

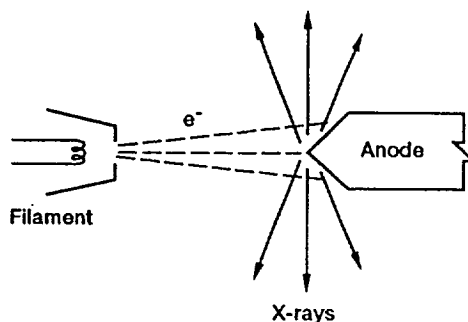
$$\psi \sim IZV^2 \quad (2.2)$$

Figures 2.2 (b) and 2.3 show the effect of the tube voltage, the tube current, the inherent filtration in the anode, and the additional filtration on the intensity of x-rays.

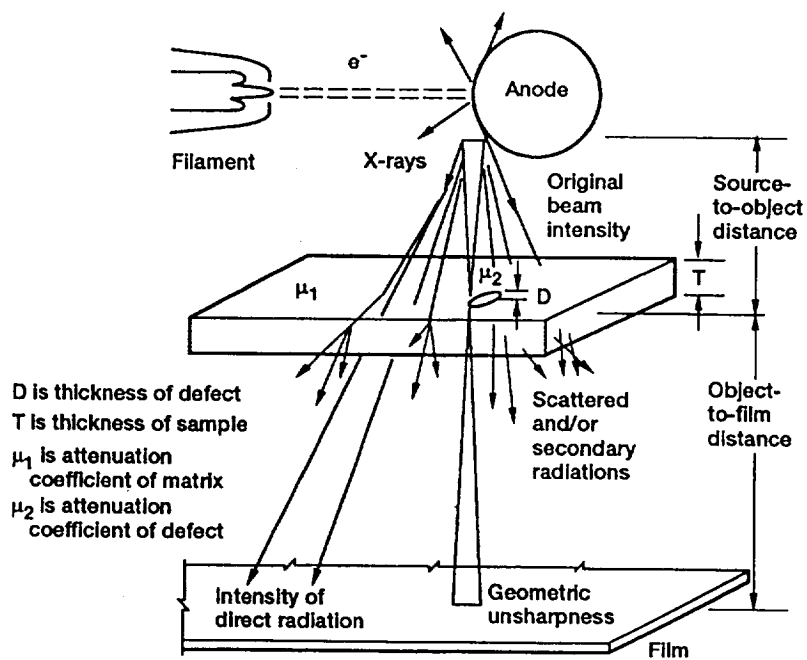
The intensity of a beam of x-rays is attenuated as it interacts with matter via absorption and scattering mechanisms. The number of photons dN passing through a thin layer of the matter depends on the number of incident photons N , and decreases proportionally to the thickness dx of the layer and the total linear attenuation coefficient μ of the material:



(a) Conventional tube.



(b) Panoramic tube.



(c) Microfocus tube.

Figure 2.1.—Schematic configurations of x-ray tubes and of microfocus projection radiography.

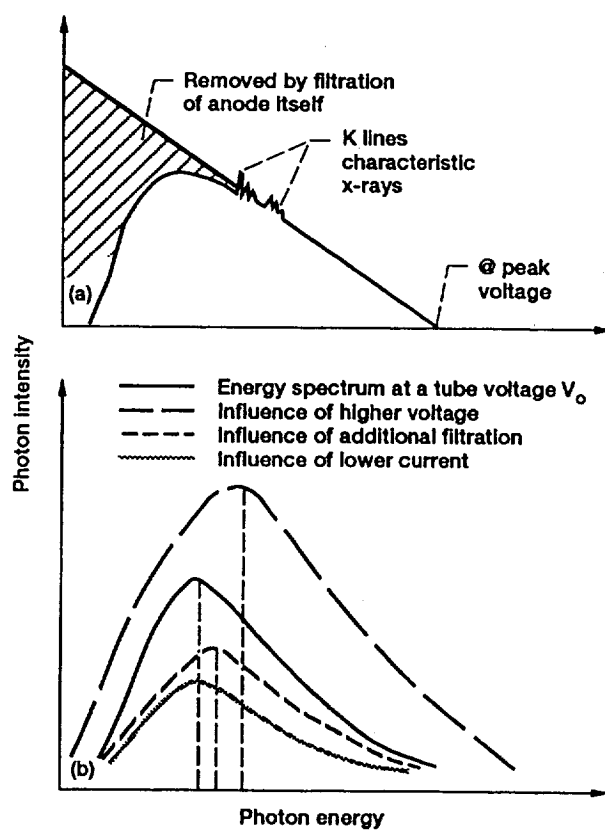


Figure 2.2.—Spectrums of x-ray energies leaving an x-ray tube.

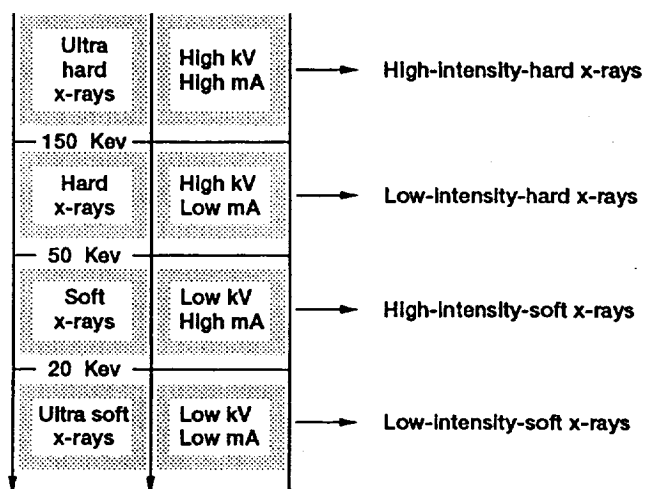


Figure 2.3.—Effects of tube potential (kV) and tube current (mA).

$$dN = - \mu N dx \quad (2.3)$$

By dividing with N and integrating over N and x the exponential law of attenuation is obtained:

$$N = N_0 e^{-\mu x_m} \quad (2.4)$$

where N_0 is the number of incident photons, N the number of transmitted photons, and x_m is the thickness of the material. In actual application a spectrum of N_0 (hf_{elect}) exists which calls for integration over hf_{elect} . The attenuation process is a very complex one which includes photoelectric absorption, Rayleigh scattering, Compton scattering, and pair production as shown in figure 2.4. Detailed information on the attenuation mechanisms can be found in Halmsaw (1982) and Siemens (1990), and information on linear attenuation coefficient dependency on Z and energy can be found in the Nondestructive Testing Handbook (Vol. 3, 1985). Briefly, the attenuation coefficient varies directly with Z for the Compton effect, between Z^4 and Z^5 for the photoelectric effect, and $Z(Z+1)$ for pair production.

Linear attenuation coefficients are proportional to the material density, ρ , which depends on the physical state of the material. Hence, most tables list mass attenuation coefficient, μ/ρ , to eliminate the density dependence. μ

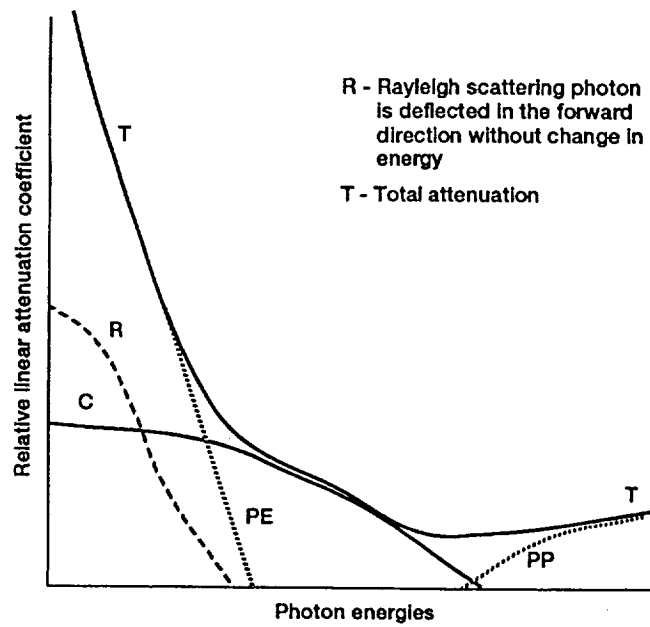
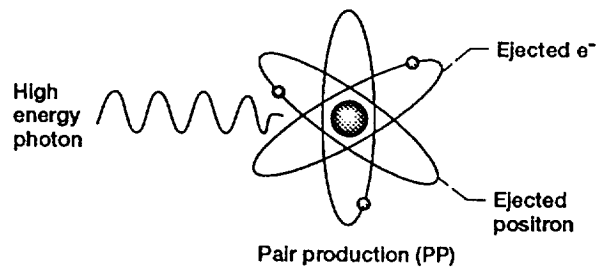
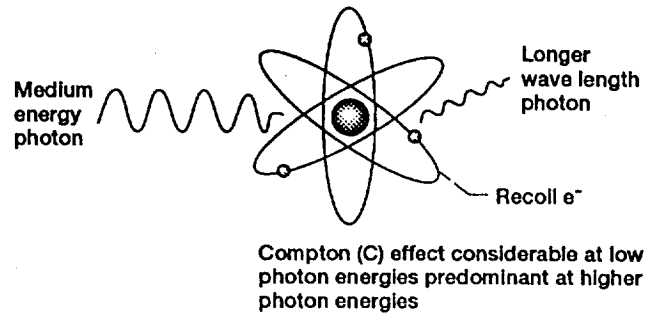
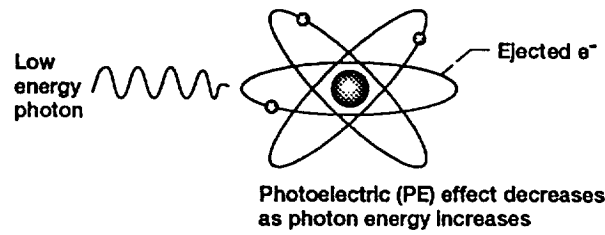


Figure 2.4.—Typical interaction of x-rays with matter.

is in cm^{-1} and ρ is in g/cm^3 , this makes the ratio μ/ρ in cm^2/g . By rewriting equation (2.4) as follows:

$$N = N_0 e^{-\mu/\rho(\rho x_m)} \quad (2.5)$$

and by using an equivalent attenuation law

$$N = N_0 e^{-n \cdot s \cdot x_m} \quad (2.6)$$

where n , the number of atoms per cm^3 , is given by $(N_A \rho)/A$, s is the total cross section atomic attenuation coefficient (proportionality constant), N_A is Avogadro's number, and A is the atomic weight; the mass attenuation coefficient μ/ρ is shown to be proportional to the total photon cross section, i.e., to the sum of all the cross sections from the scattering and absorption mechanisms, and to Avogadro's number, and inversely proportional to the atomic weight A as shown below:

$$\mu/\rho = (N_A s/A) \quad (2.7)$$

The total mass attenuation coefficient of a compound, $(\mu/\rho)_c$, can be approximately calculated from the mass

attenuation coefficients of the constituents element μ_i/ρ_i according to their relative abundance by weight

$$(\mu/\rho)_c = \sum_i w_i (\mu_i/\rho_i) \quad (2.8)$$

where w_i is the proportion by weight of the i th constituent. For example, for SiC:

$$\begin{aligned} (\mu/\rho)_{\text{SiC}} = & [28.086/(28.086+12.01115)] (\mu/\rho)_{\text{Si}} \\ & + [12.01115/(28.086+12.01115)] (\mu/\rho)_c \end{aligned} \quad (2.9)$$

For energies above 10 keV this rule of mixture introduce errors of less than 5% due to changes in the molecular, chemical, or crystalline environment of an atom (Hubbell 1969).

Several means of detecting differentials in photon attenuation exist for x-rays passing through matter. Film radiography is the most widely used technique for recording radiation as a variation in the silver deposit of an exposed and then processed film. Fluoroscopy, image intensifiers, television systems, scintillation counters, and matrix scintillator or semiconductor detectors are also used to record radiographic information.

Radiographic detectability depends on the spatial

resolution and type of energy of the radiographic system, and on the image contrast and its spatial resolution as recorded on the radiographic detector. In film radiography the spatial resolution is a function of the film graininess, which governs signal-to-noise ratio, and of the geometric resolution R given by

$$R \geq U_g / M \quad (2.10)$$

where M is the x-ray image magnification given by $M = (b+a)/a$, where a is the source-to-object distance and b is the object-to-film distance (Fig. 2.1 (c)). The geometric unsharpness U_g is given by

$$U_g = S_{fs} (b/a) \quad (2.11)$$

where S_{fs} is the focal spot size. It follows that R can be given as

$$R = S_{fs} [b/a+b]. \quad (2.12)$$

The radiographic image contrast (Parish, 1979) is given by

$$C = [0.43(\mu_1 - \mu_2)(\Delta X)G_r] / (1 + N_s/N_p) \quad (2.13)$$

where μ_1 is the total attenuation coefficient of the

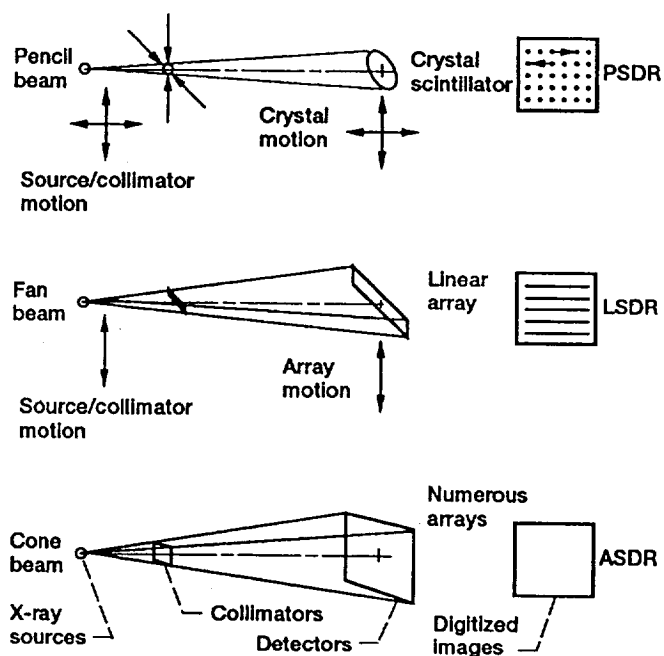
matrix, μ_2 is the total attenuation coefficient of the defect, ΔX is the dimension of the defect in the direction of the x-ray beam, G_f is the film gradient, N_s is the number of scattered photons, and N_p is the number of direct image forming radiation (primary photons).

In conventional radiography S_{fs} is on the order of 400 μm to 3mm and $a \gg b$. In microfocus radiography S_{fs} is on the order of 10 to 50 μm and $b > a$. This implies that scattered radiation are minimal in microradiography and sizeable in conventional radiography. Further, large S_{fs} in conventional radiography limits projection capabilities because of deterioration in geometric unsharpness (equation 2.11). As shown in equation (2.13), a smaller ratio of N_s/N_p and a larger difference $(\Delta\mu) = \mu_1 - \mu_2$ are needed to improve the image contrast. Microfocus radiography maximizes detectability because 1) in general it possesses an anode with a lower atomic number which increases the contrast by presenting greater differences in $(\Delta\mu)$ (Radiological Health Handbook 1970), 2) it permits projection which prevents scattered radiation from fogging the image, and 3) it has small focal spot size.

Digital x-radiography

Reviews of digital radiography (DR) are available in the literature, e.g., Reiderer (1985), Arnold, et al. (1981 and 1982), Smathers, et al. (1985), and Kereiakes, et al. (1986). Most of the DR research and applications have been in the medical community, even though digital radiography has been evolving since the late seventies. DR has profited from the digital techniques that were developed for computerized x-ray tomography applications after its invention by Hounsfield (1973).

In DR two-dimensional projection images are digitally acquired and recorded with various detector technologies and related readout procedures. DR systems include point-scan digital radiography (PSDR), line scan digital radiography (LSDR), and area scan digital radiography (ASDR) (Fig. 2.5). The first digital radiographs were digitized x-ray films read using backlighting and digitizing cameras or videcons or using densitometric scanners. Regardless of the detector technologies and the modes of conversion from analogue to digital format, digital acquisitions are ideal for (1) mass image storage, i.e., optical disks, (2) dual energy subtraction, (3) temporal subtraction, (4) compensation in wide dynamic ranges, (5) energy selective imaging, and (6) other functions including spatial and frequency filtering, contrast stretching, etc. Digital image and



PSDR = Point scan digital radiography

LSDR = Line scan digital radiography

ASDR = Area scan digital radiography

Figure 2.5.—Digital radiographic modalities.

digital signal processing can enhance and improve x-ray display capabilities (Openheim, et al., 1975; Preston, et al., 1976; Gonzalez, et al., 1977; Pratt, 1978; Capellini, et al., 1978, 1980; Simon, et al., 1980; and Macovsky, 1983).

Many critical factors that affect digital radiographic systems should be considered before any advanced digital image processing can be applied. These factors include: (1) x-ray spectrum, energy, and intensity of the source, (2) quantum detection efficiency of the source-detector system, (3) signal-to-noise (SNR) ratio (Tapiovaara and Wagner, 1985), (4) spatial resolution, (5) integration time depending on the source-detector-scanning designs, and (6) scatter reduction at the detector (Pfeiler, et al. 1985; Macovsky, 1983).

DR images are composed of square pixels. Each pixel has coordinates and an integer value representing its brightness or photon counts. An 8-bit pixel brightness ranges from 0 to 255. A typical 1024 by 1024 image consists of approximately a million pixels. Digitization of a 14 by 17 inch continuous radiographic image film requires a digital radiographic image consisting of 4 million pixels. Pixel size and field of view limit image resolution, because the highest spatial frequency that can be imaged is one cycle per two pixels according to the Nyquist criterion. Combining projection radiography (higher magnification) with

a large matrix detector improves region of interest spatial resolution. DR images are not inherently contrast-limited because brightness levels can be digitized virtually indefinitely, e.g., 256, 512, 1024, etc. But display contrast sensitivity is limited as in film radiography by (1) video display type (2) the subject contrast C_{sub} (ideal contrast neglecting scatter), and (3) the scattered radiation (Rzeszutarski and Sones, 1989):

$$C_{\text{res}} = C_{\text{sub}} [1 / (1 + \text{SPR})] \quad (2.14)$$

where, SPR is the ratio of the scattered radiation to the primary radiation, and C_{sub} is $\mu\Delta X$ if $\mu\Delta X \ll 1$. Equation 2.14 is a general form of the contrast equation 2.13.

The signal-to-noise-ratio (SNR) and the contrast are interdependent

$$\text{SNR} = (K \cdot C_{\text{res}}) / \sigma(X) \quad (2.15)$$

where, K is a proportionality constant (for example K is $0.43(G_r)$ in equation 2.13), $K C_{\text{res}}$ is the radiographic contrast of a specific feature to-be-imaged, and $\sigma(X)$ is the quantum noise. $\sigma(x)$ has a Poisson distribution that is a function of the quantum efficiency of the detector or screen η , the number of transmitted photons, and the sampling area A_s :

$$\sigma(X) = K/\sqrt{{}^nA_s N} \quad (2.16)$$

where ${}^nA_s N$, a dimensionless quantity, is the effective number of photons absorbed in the sampling area A_s .

The detection quantum efficiency (DQE) is a measure of efficiency of information transfer, given by

$$DQE = [SNR/SNR_{ideal}]^2 \quad (2.17)$$

where SNR_{ideal} is the SNR of the primary radiation N_p . Overall DQE is a product of all components of DQE. DQE is always between 0 and 1. The SNR from equation 2.15 can now be written as

$$SNR = C_{sub} \sqrt{N_{eff} \cdot A_s} \quad (2.18)$$

where N_{eff} is the product of DQE and N_p , the effective value of the primary photons.

PSDR possesses excellent scatter-elimination capabilities, low electronic noise, and high quantum detection efficiency. The beam geometry dictates spatial resolution, and time of exposure. A major disadvantage of PSDR is inefficient use of the x-ray tube flux. LSDR exhibits good scatter removal capabilities, low electronic

noise, wide dynamic range, and high contrast detectability. Disadvantages of LSDR are inefficient use of radiation and variations in sensitivity between detectors. ASDR is very efficient in using the full x-ray beam and allows near-real-time acquisition. ASDR resolution is dictated by the particular readout technology used and its contrast sensitivity is dictated by the material detector. The principal disadvantage of ASDR is poor scatter removal capabilities.

X-ray computed tomography

Equation 2.4 can be rewritten by applying the logarithm to the ratio N_0/N as follows in equation 2.19.

$$\ln(N_0/N) = \mu(E_{\text{elect}})x_m \quad (2.19)$$

In the case of inhomogeneous materials, equation 2.19 becomes the line integral along the x-ray beam that is the sum of the linear attenuation coefficients,

$$\ln(N_0/N) = \int_0^x \mu(X, E_{\text{elect}}) dx \quad (2.20)$$

This line integral is the foundation of x-ray computed tomography. Sums of line integrals for a systematic series

of angles and positions comprise the raw CT data. Most x-ray CT scanners use polychromatic radiation that can be treated as a large number of monochromatic beams (Pullan, et al., 1981), each with different energy. Then, the number of photons exiting a sample is given by

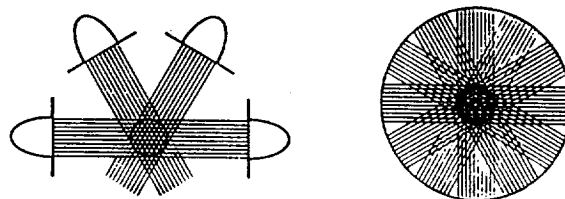
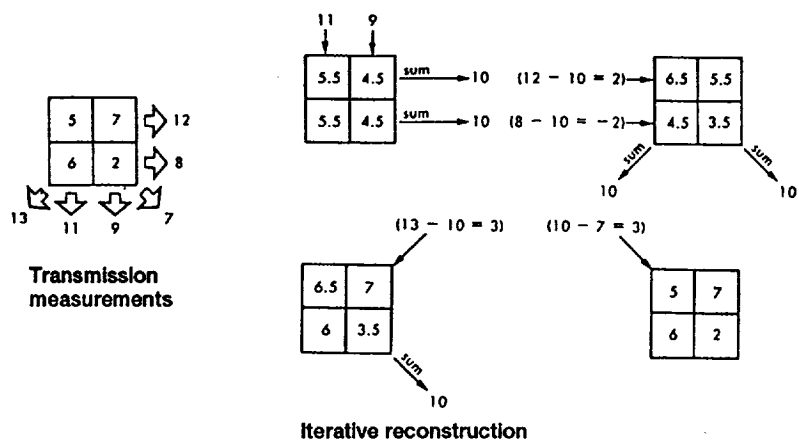
$$N(X, E_{elect}) = \int_0^{E_{max}} \left[N_0(X, E_{elect}) e^{-\int_0^X \mu(X, E_{elect}) dx} \right] dE \quad (2.21)$$

where E_{max} is the maximum tube energy. However, this polychromatic radiation introduces the following complications, (1) "beam-hardening" whereby high energy photons are less attenuated than the low energy photons as they pass through the sample, increasing the mean beam energy in an unpredictable manner, and (2) inaccurate transmission measurement readings by CT detectors that are in general proportional to the number of photons and their energy. Once beam hardening corrections are made, the linear attenuation coefficient is computed based on an effective transmission measurement where the μ is assumed constant within each voxel (a 3-dimensional pixel).

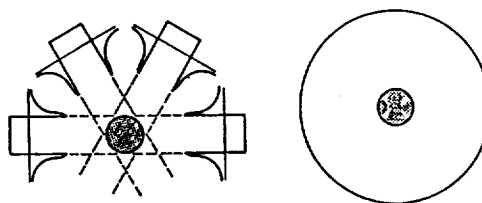
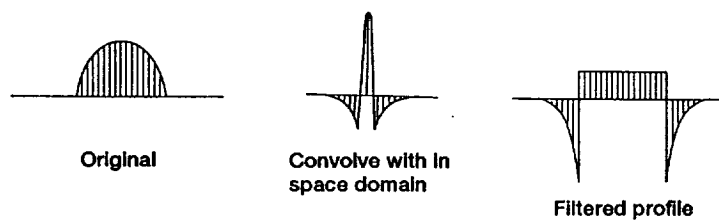
Cormack (1963, 1964) demonstrated in x-ray tomography the importance of finding a real function in a finite region of a plane by defining its line integrals along all straight lines intersecting the region, similar to the original mathematical problem of reconstructing a two dimensional

function from its projected line integrals (Radon, 1917). Similarly, Hounsfield (1973) obtained the solution to unknown x-ray attenuation coefficient in two dimensional domains by solving a set of simultaneous equations where the pixel value can be calculated with the assumption that it contains a percentage of the attenuated radiation as depicted in the iterative reconstruction of figure 2.6. The two scientist shared the Nobel Prize in 1979 for Physiology and Medicine. The line integral approach is valid in x-ray transmission tomography where the wavelength of the x-ray beam is much smaller than the size of the feature to be imaged, hence eliminating any x-ray diffraction complications (Azevedo, 1988).

In x-ray computed tomography, information regarding the innermost regions of an opaque object is provided by measuring the x-ray energy transmitted through that object and reconstructing individual cross-sections of it. Many simplifying assumptions are used in the reconstruction processes (Herman, 1981). These reconstruction processes, e.g., the ones depicted schematically in figures 2.6 and 2.7, permit solving for the CT number for each voxel within the object given the x-ray transmission attenuation values along a large number of lines in the cross-section. The CT number is related to the linear attenuation coefficient of the material,



Simple back projection



Filtered back projection

Figure 2.6.—Iterative reconstruction and back projection representations in x-ray computed tomography. (From Zatz 1981).

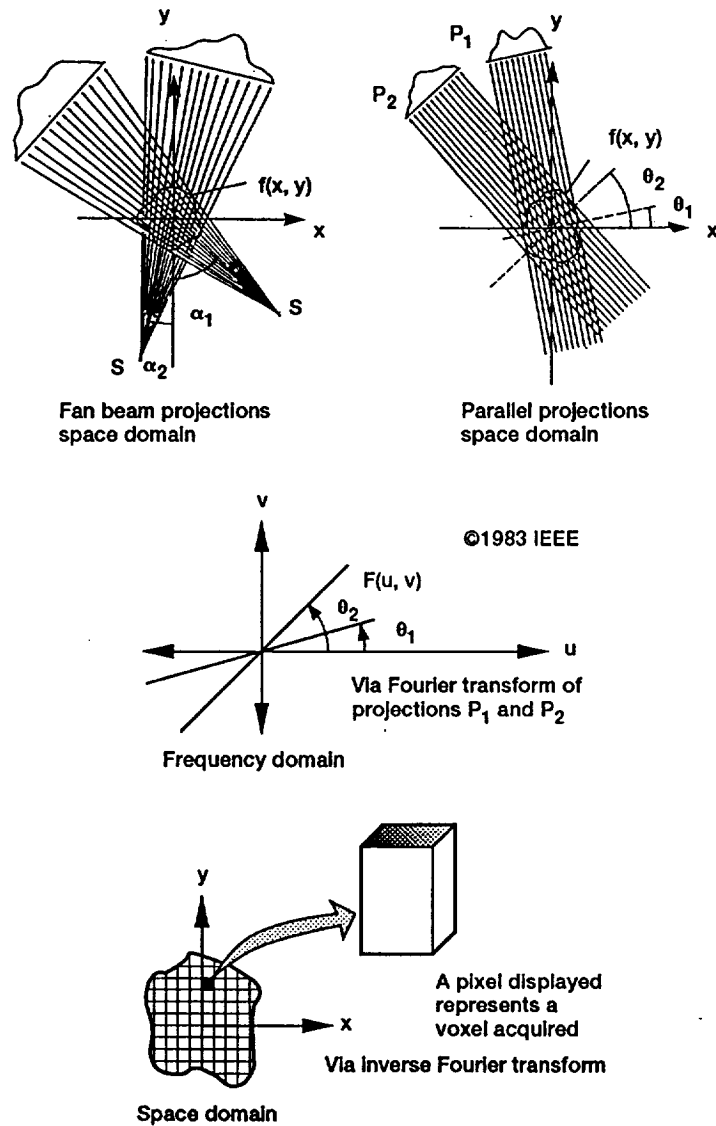


Figure 2.7.—Fourier transform of projections constructs the Fourier transform of the object that can be inverse Fourier transformed to reconstruct the object. (Modified from Kak and Slaney 1988).

$$CT \text{ number} = \frac{\mu_{\text{material}} - \mu_{\text{water}}}{\mu_{\text{water}}} \times 1000 \quad (2.22)$$

A CT number equal to zero corresponds to water, and a CT number of -1000 corresponds to $\mu = 0$ which is taken as identical to that of air. The precision of the CT number identifies the potential of the CT value for a single voxel in representing that of a homogeneous object made from the exact same material. The accuracy of the CT number identifies how close the measured CT number is to the true value, which is the total mass attenuation coefficient of the voxel converted into a CT number. As discussed earlier in this chapter the total mass attenuation coefficient varies with the effective x-ray beam energy. This effective energy depends on the tube potential settings, on the energy spectrum of the polychromatic source, and on the attenuating materials. Consequently, in order to use CT numbers for precise and accurate representation of the total mass attenuation coefficient, phantoms (Kropas et al., 1991) that contains the same chemical elements as the material under evaluation shall be used to calibrate the CT scanners.

Reconstruction algorithms are classified in two major categories (1) the transform algorithms which include convolution methods, and (2) the series expansion algorithms. Filtered back projection using a transform algorithm is the most commonly used method. The steps are

(1) measure the projections of $f(x,y)$, (2) Fourier transform them to obtain $F(u,v)$ in the frequency domain, (3) convolve with a weighting function, and (4) inverse Fourier transform to reconstruct the object. Detailed examples of the back projection algorithm for parallel beam, equiangular fan beam, and equispaced fan beam are treated in Kak and Slaney (1988). Series expansion algorithms are slow in comparison to transform methods because they converge too slowly, and the availability of fast array processors make back projection transform much more attractive.

All algorithms possess artifacts (Joseph, 1981; Azevedo, et al., 1988) e.g., point spread effect, streaking, and edge enhancement (density distortion at sharp edges). Artifacts in CT are numerous and can be due to the geometry of the scanner, nonlinearity of x-ray measurements, scatter, beam hardening, partial volume effect, aliasing, and insufficient angular sampling. Combined with image quality limitations (Zatz, 1981) due to noise, insufficient spatial and contrast resolution, image artifacts require a more detailed examination of capabilities and limitations of each specific CT system relative to specific material and objects.

Extensive reviews of XCT are available in the literature, e.g., entire issues of technical journals in IEEE Transactions on nuclear medicine and medical imaging during the late seventies and early eighties, Ter-Pogossian

(1977), Newton and Potts (1981), Kak (1988). Development of industrial versus medical XCT systems has been advanced by Scientific Measurement Systems Inc., Bio-Imaging Co., Innovative Imaging Systems Inc., Advanced Research and Applications Corporation, and General Electric.

Considerable research effort has been mounted for application of these CT systems in characterizing advanced ceramic materials, (Sawicka, et al., 1986, 1987; Ellingson, et al., 1987b, 1988; Yancey, et al., 1990a, 1990b; London, et al., 1990; Kinney, et al., 1990, 1991; Baaklini, et al., 1991). Chapters IV and V will present new data on the capabilities and limitations of a particular CT system for characterizing ceramic and metal matrix composite components.

Medical CT scanners are evolved into four generations/ types depending on the detector-source configurations. In the first generation the source and a single detector translate and rotate, in the second generation the source and a linear array detector translate and rotate, in the third generation the source and the fan beam array detector rotate, and in the fourth generation the source rotates with an encircling fixed 360 degree detector. For research and industrial application, the source and the detector are usually fixed and the object holder translates and rotates. The system described in chapters IV and V is schematically presented in figure 2.8 and a CT slice is shown depicting

the CT number variations within a composite object. The magnification is on the order of 1.6 for all the scans in chapters IV and V. The effective spatial resolution for the system is 250 μm . More detailed information on the system is provided in chapter IV.

Ultrasonics

The emphasis in this section is on acoustic microscopy. Acoustic microscopy is a pulse-echo ultrasonic immersion technique that uses focused transducers (Lemons et al., 1979; Nikoonahad, 1984; Khuri-Yakub et al., 1985). The sound is focused by using curved piezoelectric material, or ultrasonic lenses, e.g., a plano-concave lens glued to the piezoelectric crystal, or a biconcave lens attached to the front of the transducer (Birks and McIntire, 1991).

The lens concentrates the ultrasonic beam energy and the focal plane is set within the sample to reduce the effect of surface conditions on the reflected signal. The major advantage of using focused transducers is the ability to focus at different depths in the sample by adjusting the distance between the transducer-lens and surface of the sample. The reflected ultrasonic pulse is time-gated and changes in signal amplitude form an image of the sample volume at a preselected depth (Fig. 2.9). The image is

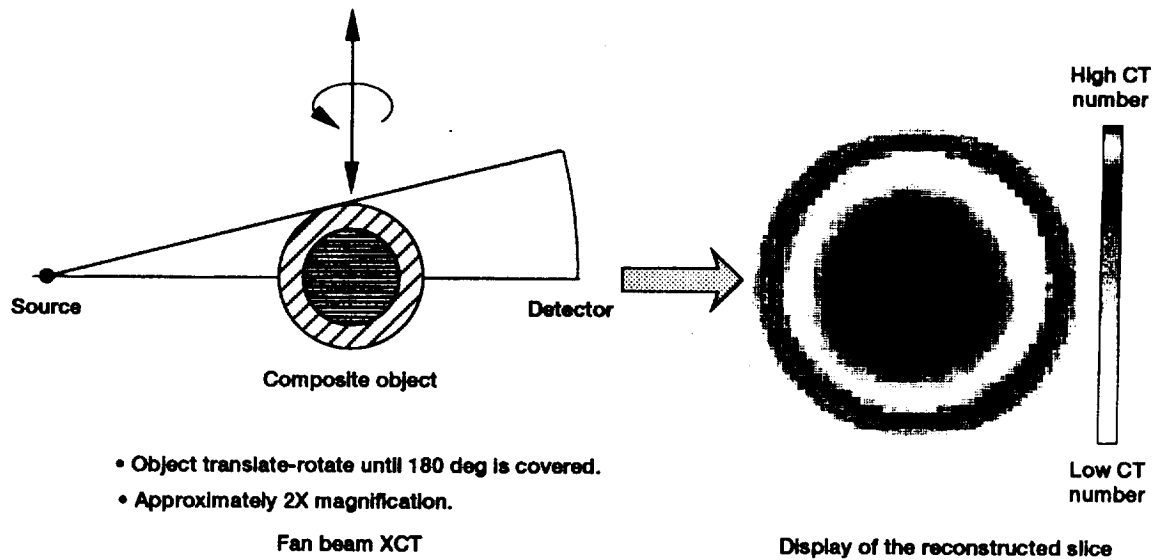


Figure 2.8.—A schematic of the LAM/DE scanning geometry and a display of the resulting CT slice.

ORIGINAL PAGE
COLOR PHOTOGRAPH

FIG 36 INTENTIONALLY BLANK

PRECEDING PAGE BLANK NOT FILMED

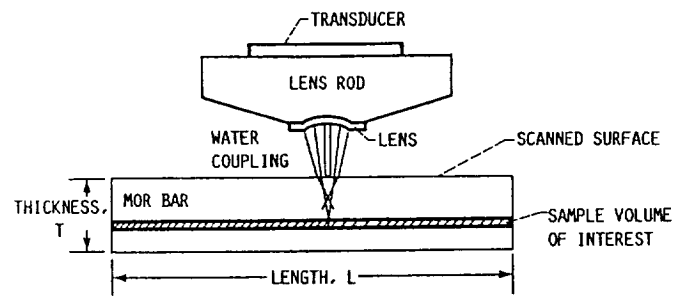
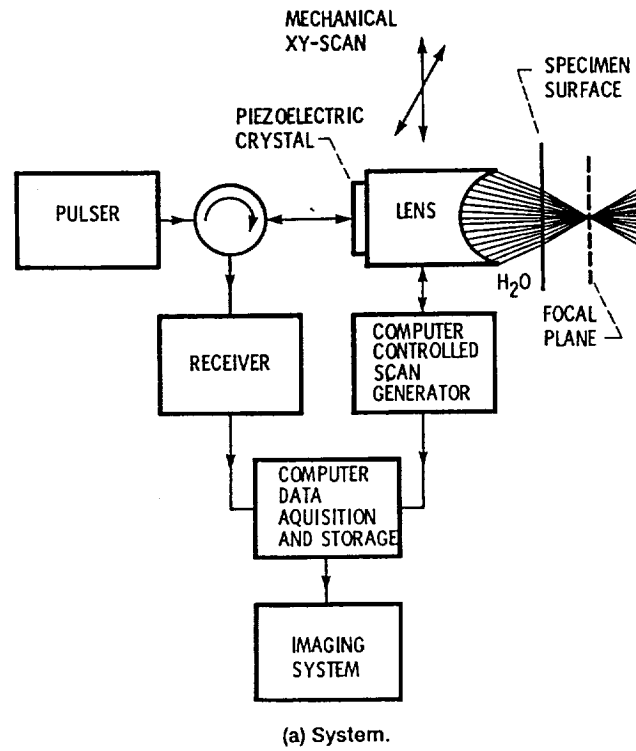


Figure 2.9.—Scanning acoustic microscopy.

PRECEDING PAGE BLANK NOT FILMED

216 38 INTENTIONALLY BLANK

acquired in scanning acoustic microscopy (SAM) similarly to a conventional ultrasonic C-scan using precision mechanical scans.

The signal amplitude will be affected by density variations, cracks, voids (Klima, et al., 1986), impurities, and delaminations in laminated composite structures (Khuri-Yakub, et al., 1985). Typically a 50 MHz system can detect 20 μm voids located 1 mm below the surface in monolithic silicon nitride ceramics (Klima, et al., 1986).

The system shown in figure 2.9 is used to corroborate the presence of density variations found by x-ray computed tomography, see Chapter IV.

NDE Role in Materials Development and Characterization

Brittle fracture in monolithic ceramics is dominated by minute defects and microstructural artifacts while composite fracture is dominated by fiber strength and fiber-matrix bond strength. The role of NDE in characterizing densified monolithic ceramics differs greatly from its role in densified metal and ceramic matrix composites. The NDE varies from defect detection and density characterization in monolithics to noninvasive failure monitoring and characterization of constituent integrity in composites.

Monolithic ceramics

Strength and toughness of monolithic ceramics are degraded by the presence of minute defects (Evans, 1984; Singh, 1988; Gyekenyesi, 1988). Thus, the principal role of NDE is to detect and size minute flaws, 10 μm to 100 μm in size, e.g., cracks, voids, high density impurities, hard and soft agglomerates, and large grains (Klima and Baaklini, 1986; Sanders and Baaklini, 1989; and Sanders, et al., 1989). It is essential to characterize the milieu of these discrete flaws because it is the surrounding material that hinders or facilitates the crack growth and fracture. Subtle variations in density and in phase composition may degrade material properties (Rice, et al., 1977; Nishida, 1983; and McCauley, 1987).

In materials development and characterization NDE of monolithics is well established in the green state and in the densified state. The following NDE methods are applicable to green state bodies: nuclear magnetic resonance to measure porosity and distribution of binders (Ackerman, et al. 1987), film radiography to study green density uniformity and its effect on sintered bodies (Sanders and Baaklini, 1988) and to evaluate reliability of flaw detection (Baaklini and Roth, 1986a), x-ray computed tomography to study density gradients (Ellingson, et al. 1987a and 1987b; and Friedman, et al. 1987), and ultrasonic

velocity to evaluate density changes (Kupperman, et al. 1984). NDE of densified state includes: gamma-ray computed tomography (Sawicka and Palmer, 1986; Sawicka and Ellingson, 1987), ultrasonics (Iwasaki, 1981; Klima, et al., 1981; Khuri-Yakub, et al., 1980, and 1982; and Tittman, et al., 1980; Generazio, 1985, 1987), scanning laser acoustic microscopy (Kessler and Yuhas, 1978; Yuhas, et al., 1979; Roth, et al., 1986), photoacoustic microscopy (Rosencwaig, 1982; Khandelwal, 1987), and x-radiography and x-tomography (Feldkamp and Jesion, 1986; Baaklini, et al., 1986b; and Kress and Feldkamp, 1983). These NDE techniques demonstrated applicability with certain limitations to flaw detection and to density interrogation in coupon type monolithic ceramic samples.

As discussed earlier, in chapter I, NDE of engine components is very limited. A vital role of NDE is to modify the existing NDE techniques that worked well in coupon type sample for a successful transfer into the component manufacturing and testing areas. Imaging modalities with quantitative assessment capabilities will be required to expose global variations in density, in chemical composition, and in flaw population. Chapter IV establishes capabilities and limitations of x-ray computed tomography as it applies to monolithic ceramic components.

Composites

NDE of high temperature composites is maturing as researchers learn how to overcome difficult inspection problems. These NDE problems include characterization of matrix anomalies, fiber-matrix interfaces, and fiber architecture peculiarities .

In CMCs the matrix possesses randomly distributed flaws. These flaws initiate microcracks that propagate and coalesce to form macro-cracks. These cracks can be rendered benign if they are bridged. Bridging occurs if the fiber-matrix interface is weak enough to deflect the cracks and is simultaneously strong enough for load transfer from matrix to fibers. An optimized fiber-matrix interface would effectively increase the toughness of the composite and its ultimate strength. Ceramic matrices are usually porous and this porosity permits fiber degradation particularly at high temperatures in an oxidizing environment.

Multiaxial fiber reinforcement using 2-D and 3-D weaves and braiding provide strengthening of the composite in principal directions and a relative ease in fabrication of complex shape composites. Braiding and weaving prevent delaminations. But poor matrix material infiltration in 2-D and 3-D preforms can result in density variations, poor densification, and thus decreasing the critical matrix cracking stress.

The mechanical behavior, damage accumulation, and fracture in CMCs must be better understood to establish appropriate objectives for NDE. Models for initiation of matrix cracks, stiffness degradation, and load redistribution need to be developed. On-line NDE is needed to help improve processing and help optimize interfaces via proper feedback. Quality control NDE is required to characterize and assure reliability of subscale components as they become available. Noninvasive monitoring of damage accumulation and failure sequences in loaded composites are urgently needed to provide greater understanding of composite mechanical behavior. Chapter VI describes an in-situ x-ray material testing system capable of visualizing damage accumulation and the failure sequence in CMC tensile specimens under load.

Aerospace engine companies are making MMC subscale engine components (Hartsel and Christopher, 1990; Hughes, 1991) concurrently with material development and optimization because these emerging material systems require considerable improvement and innovation in design and manufacturing technologies. Building a 21st century civil propulsion system can be very time consuming especially because of economical and environmental stringent constraints. Chapter V demonstrates the role of NDE in guiding the development of emerging high-temperature composite components.

CHAPTER III

POINT SCAN DIGITAL RADIOGRAPHY

Introduction

In this chapter a point scan digital radiography system is developed to mainly characterize density variations in monolithic ceramic materials and possibly to identify composite constituents in ceramic matrix composite materials. The objective is the development of a high resolution high contrast digital radiography system. The resolution is controlled by selection of appropriate source and detector micro-collimators (100 μm in diameter). The contrast is dictated by the intensity of the beam for photon counting statistics, by the energy spectrum of the x-ray source, by the DQE of the detector, and by the subject contrast.

If this system proves viable for characterizing ceramic matrix composites, the system can be upgraded to handle in-situ x-ray monitoring of these composites under tensile

loading. Further, a comparative analysis with an in-situ film radiographic technique (chapter VI) can be established. The capabilities and limitations of the system are discussed.

System Buildup

The PSDR consists of an x-ray generator/controller¹, an x-ray tube², an x-ray detector³, x-ray source and detector collimators, a source collimator positioner⁴, sample and detector positioning stages and controllers⁵, a photon counter⁶, a voltage generator for the detector, a digital multimeter and an oscilloscope, a Microvax II⁷ with general purpose interface bus (GPIB) capabilities, a VT 340 terminal, and an image display monitor. Figure 3.1 shows the digital radiographic work station and the x-ray generator/controller that is labeled low energy. Figure 3.2 shows a block diagram presentation of the system. Figures 3.3 and 3.4 highlight the major components of the system.

¹ XDR-5 by General Electric

² AEG Corporation Electronic Component Somerville, NJ.

³ Bicron Corporation, Newbury, Ohio

⁴ Oriel Corporation, Stratford, Conn.

⁵ Klinger Scientific Richmond Hill, New York.

⁶ John Fluke Mfg. Co., Inc., Everett, Washington.

⁷ Digital Equipment Corporation

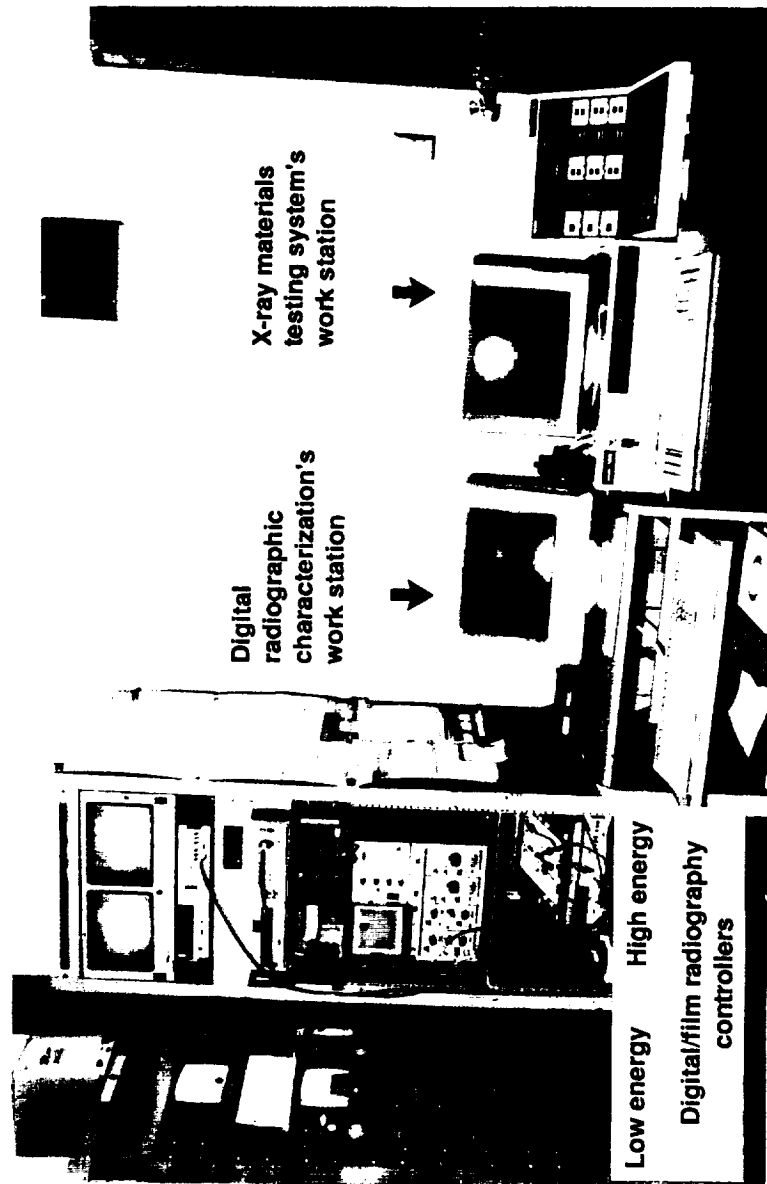


Figure 3.1.—Digital and film radiography control room.

ORIGINAL PAGE
COLOR PHOTOGRAPH

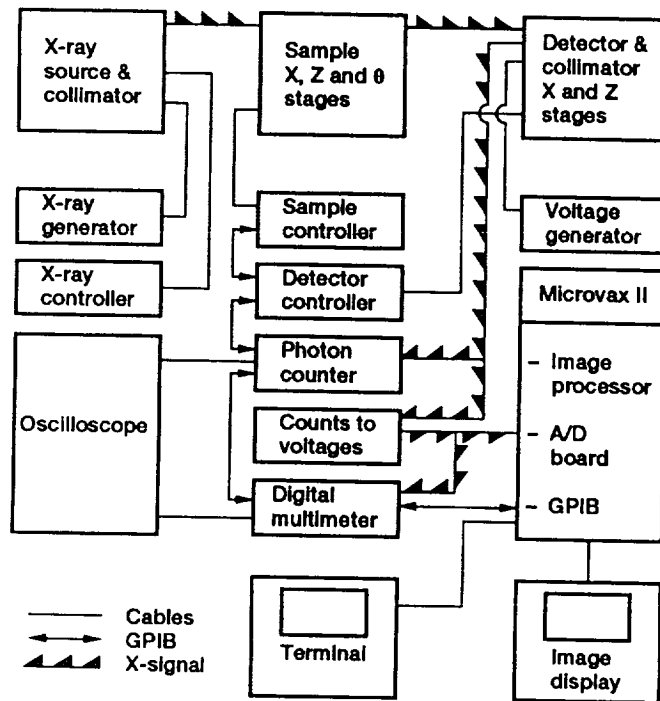


Figure 3.2.—Digital radiographic system block diagram.

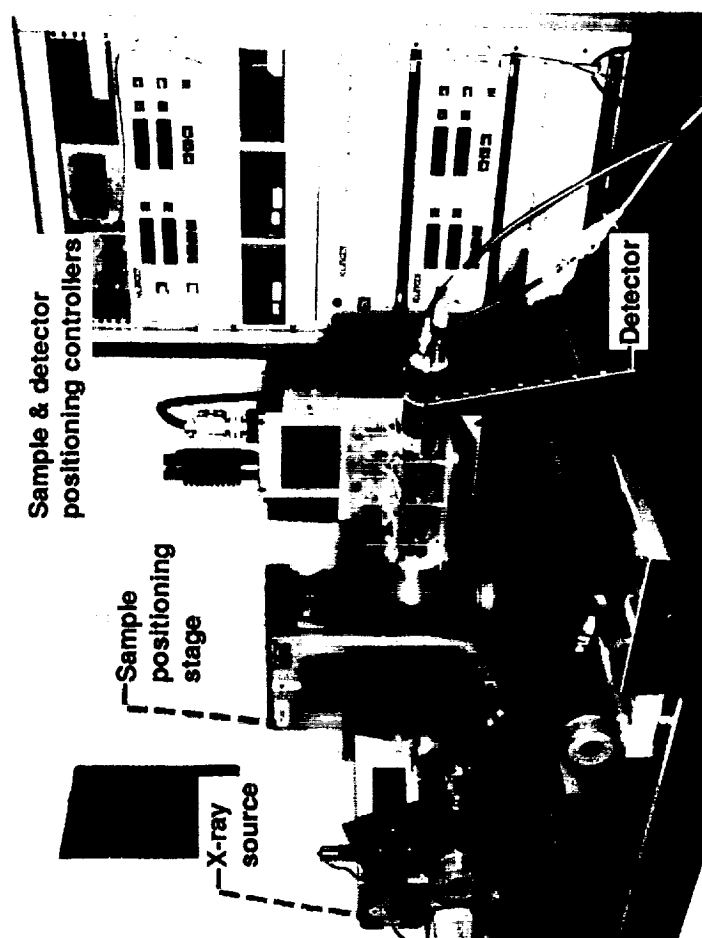


Figure 3.3.—Point scan digital radiography characterization system.

ORIGINAL PAGE
COLOR PHOTOGRAPH

PRECEDING PAGE BLANK NOT FILMED

50



Figure 3.4.—Point scan digital radiography characterization system close up.

ORIGINAL PAGE
COLOR PHOTOGRAPH

PRECEDING PAGE BLANK NOT FILMED

57

The x-ray generator/controller can produce continuously variable x-ray intensities in the range of 10 to 50 kV at tube currents from 1 to 50 mA. Full wave rectified operation rates the high voltage transformer at 50 kV and 50 mA maximum. The x-ray tube has a Cu anode which limit the tube power to 2 kW. The focal spot size at the anode is $1 \times 10 \text{ mm}^2$ and the filtration is a 0.4 mm beryllium (Be).

The collimators are $100 \text{ }\mu\text{m}$ in diameter. The resulting collimation is always less than or equal to $100 \text{ }\mu\text{m}$ due to aligning the source collimator and the detector collimator. The source collimator is positioned by using a motorized remote control encoder mike actuator that contains the bushing collimator mount. The detector collimator is fixed at the front end of the detector and is positioned by aligning the detector package.

The detector contains a 1 mm thick and 2.54 cm diameter thallium activated sodium iodide NaI (TL) crystal, a $125 \text{ }\mu\text{m}$ Be window, a voltage divider, a low noise photomultiplier tube and a solid state preamplifier. The detector signal offers capability for pulse counting (if connected to a photon counter) and for pulse amplitude and energy analysis (if connected to a multi-channel analyzer). The crystal light conversion efficiency is ten times that of $\text{Bi}_4\text{Ge}_3\text{O}_{12}$, four times that of CdWO_4 , and twice that of CsI(TL) . The crystal primary decay is $0.23 \text{ }\mu\text{sec}$ which is comparable to that of $\text{Bi}_4\text{Ge}_3\text{O}_{12}$, twenty times faster than that of CdWO_4 .

and four times faster than that of CsI(TL). The crystal scintillator is hygroscopic and has a relatively low afterglow. At the energy of operation the 1 mm thick crystal has 100% absorption efficiency. The use of an 125 μm beryllium, Be, radiation entrance window provides 100% transmission above 10 keV. This detector allows substantial accuracy at low count rates and produces one electric output pulse for every photon absorbed. Bellian and Dayton (1974) noted that the energy required to produce a photon of usable light in the NaI(TL) crystal is in the range of 40-50 eV.

The scintillation crystal absorbs the transmitted photons where subsequent excitation of fluorescent materials take place. The deexcitation of the fluorescent materials from a high energy state results in the emission of light photons. In the photomultiplier tube these light photons are collected and converted to electric pulses to be counted and analyzed.

The photon counter time gate is set to 0.1 sec. The photon count is always gated at 0.1 sec multiplied by 10 to give the count displayed per second. The trigger level is chosen based on monitoring the electrical pulses via an oscilloscope and changing the trigger level control based on a digital readout from a voltmeter connected to the rear panel of the counter.

The sample position stages have 0.1 μm step size capabilities in the horizontal and vertical directions and a 0.05 degree for a rotation step size around the vertical axis. The detector positioning stages have a 10 μm step size capability in the horizontal direction and a 1 μm step size capability in the vertical direction. The stages are controlled via IEEE-488 interface (also known as GPIB) by using programmable stepper motor controllers that "listen and talk." The source to object (sample) distance is 26 cm and the source to detector distance is 26 cm unless otherwise stated.

During the preprogrammed computer-controlled scanning process, the x-ray source and the detector are fixed, the x-ray source and the detector are on for the entire scan time, and the sample translates in the horizontal and vertical directions. X-rays pass through the sample as it traverses in a horizontal direction, line after line, stopping after every step, long enough for data acquisition and storage, until the end of the scan. The data is then averaged, scaled from 0 to 255, displayed, contrast stretched, and color coded.

Figure 3.5 shows the x-ray beam profile of the collimated Cu source. This is the result of keeping the source stationary and translating the collimated detector in a horizontal and vertical direction. The location of the global maximum count is identified and the detector is then

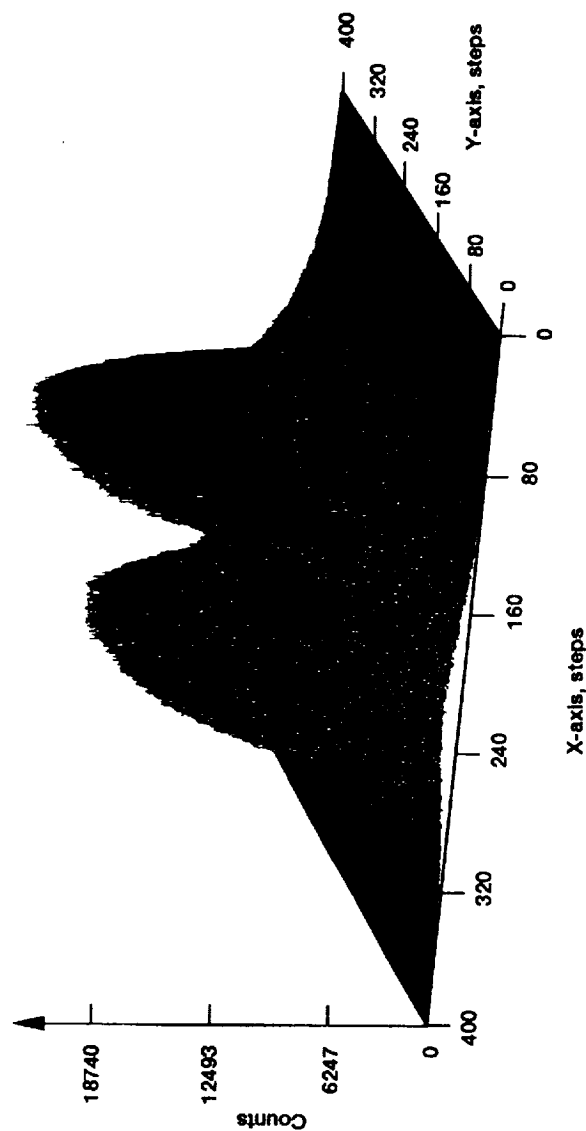


Figure 3.5.—X-ray beam profile of the collimated Cu tube.

ORIGINAL PAGE
COLOR PHOTOGRAPH

PRECEDING PAGE BLANK NOT FILMED

58 INTENTIONALLY BLANK

fixed at the optimized location for digital data acquisition. Figure 3.6 shows the beam stability over 15 hours span. Figure 3.6(a) displays photon counts versus time where data is acquired every 20 seconds. These data show that the x-ray beam reaches stability approximately one hour after startup. Startup is defined as the start of monitoring after one hour of tube/system warmup. Figures 3.6(b) shows photon occurrences versus photon counts, and figure 3.6(c) shows observations versus photon count where the span is one standard deviation wide.

The Cu tube bimodal profile is unexpected. In general the x-ray tube profile looks like the microfocus tube profile shown in figure 3.7. The bimodal profile may be due to the Cu tube filament design or to a defective filament. The bimodal profile did not affect the experiment because of collimation, at the source and detector, respectively. The Cu anode was chosen because of its energy spectrum where photons and characteristic x-rays are predominant in the low keV region. This is required by the contrast equation (2.14) where the difference in total mass attenuation coefficient controls subject contrast C_{sub} . The ratio of scattered to primary radiation in this setup is optimum because of the micro collimation used. It is evident from figure 3.8 that the only available energy window open for differentiating among silicon carbide, silicon nitride, and air is in the 10 to 20 keV region. From figure 3.9 a higher

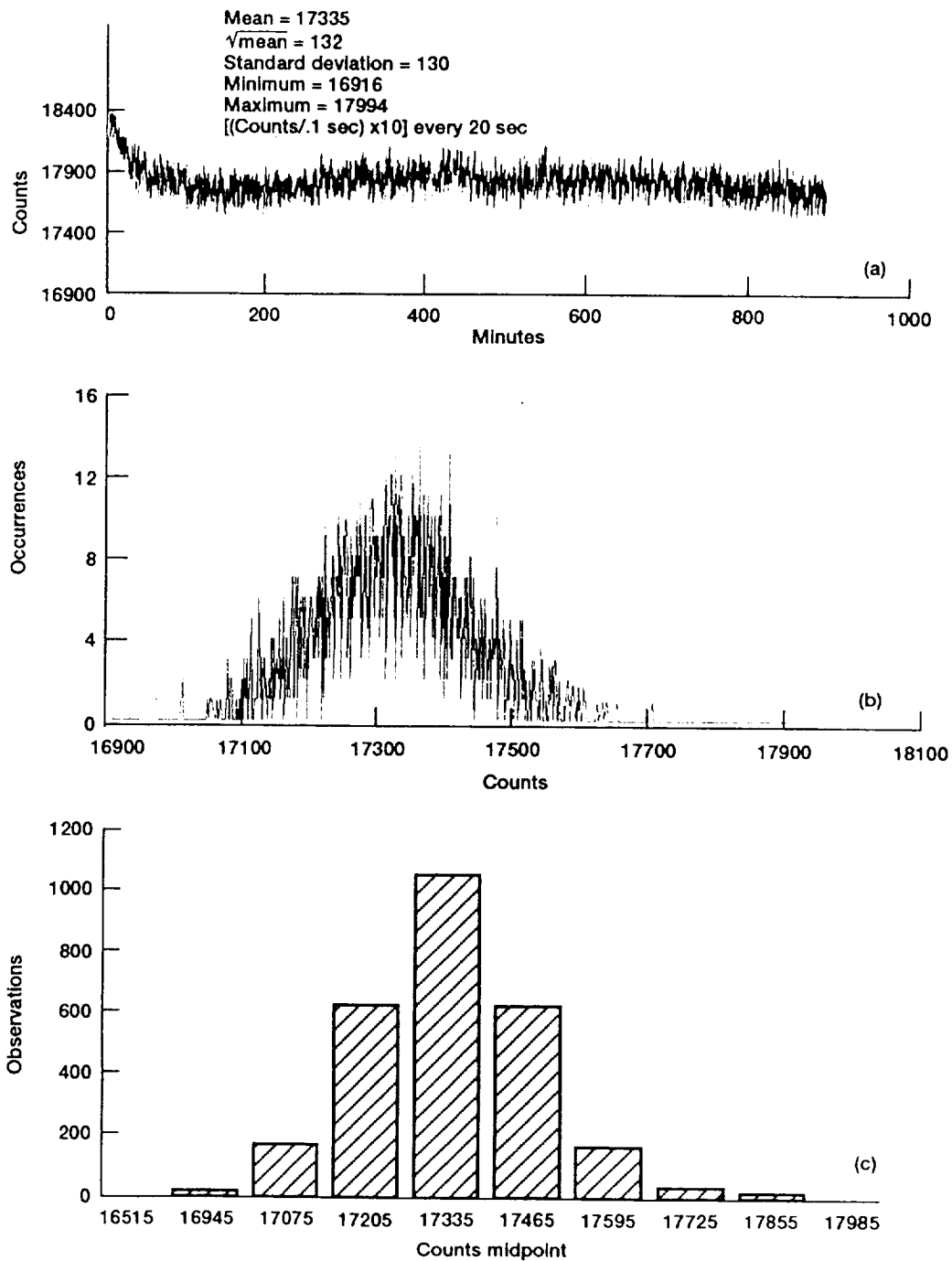


Figure 3.6.—Beam stability and related photon counts at optimized location for maximum photon counting.

62
 INTENTIONALLY BLANK

PRECEDING PAGE BLANK NOT FILMED

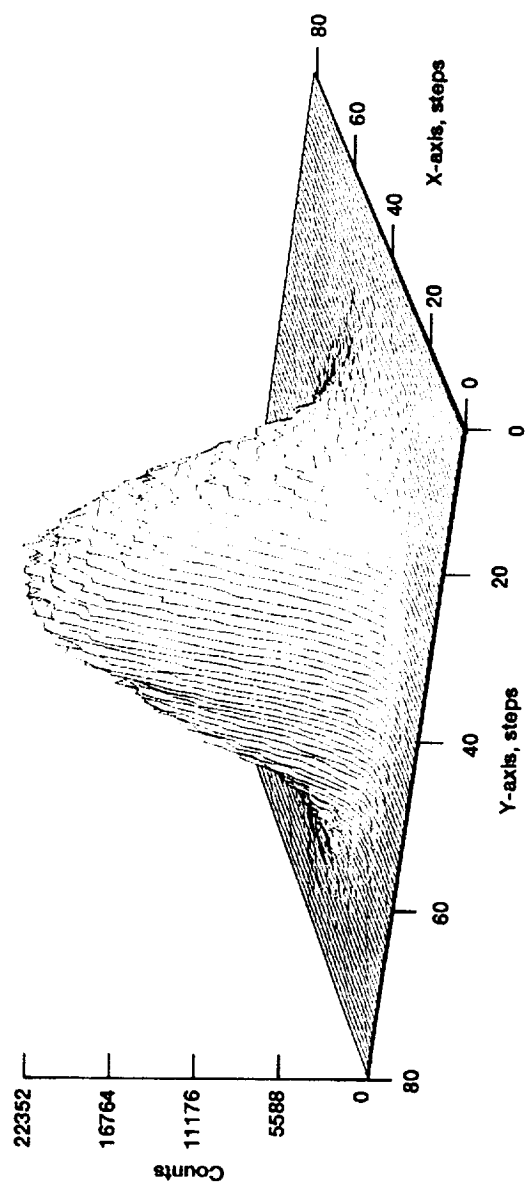
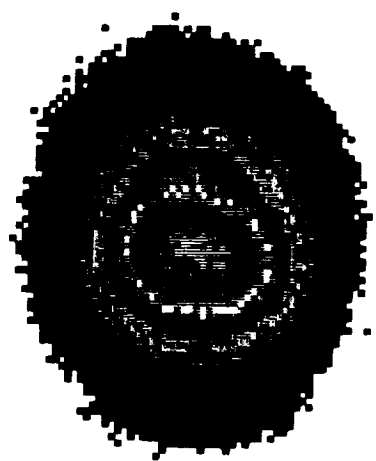


Figure 3.7.—X-ray beam profile of the microfocuss Mo system.

64

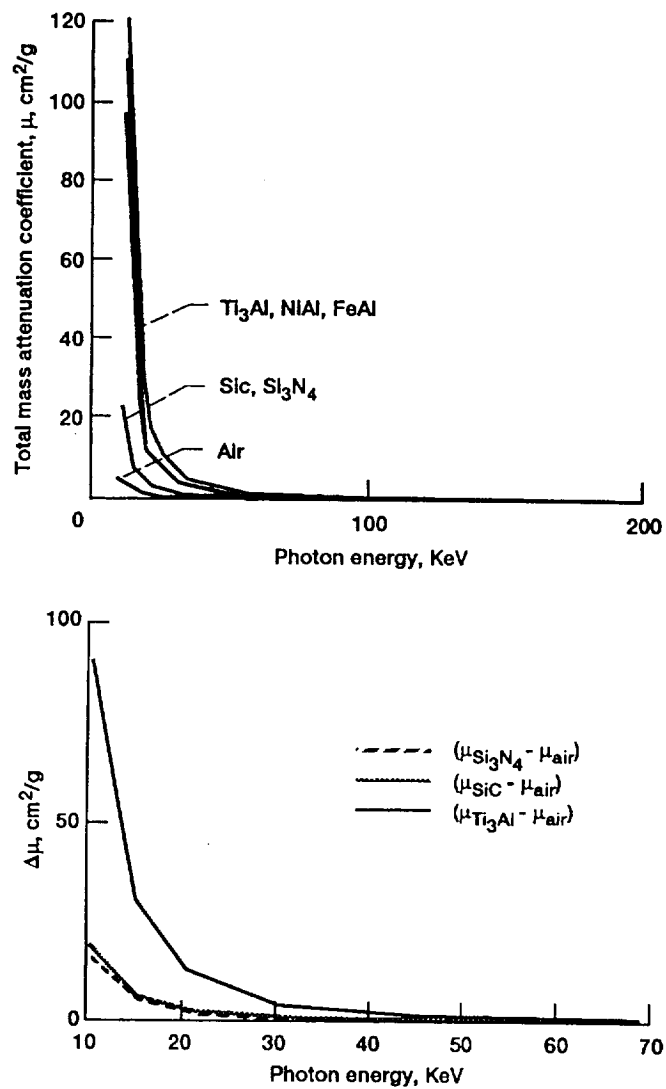


Figure 3.8.—Total mass attenuation coefficient and differential in total mass attenuation coefficient versus photon energies.

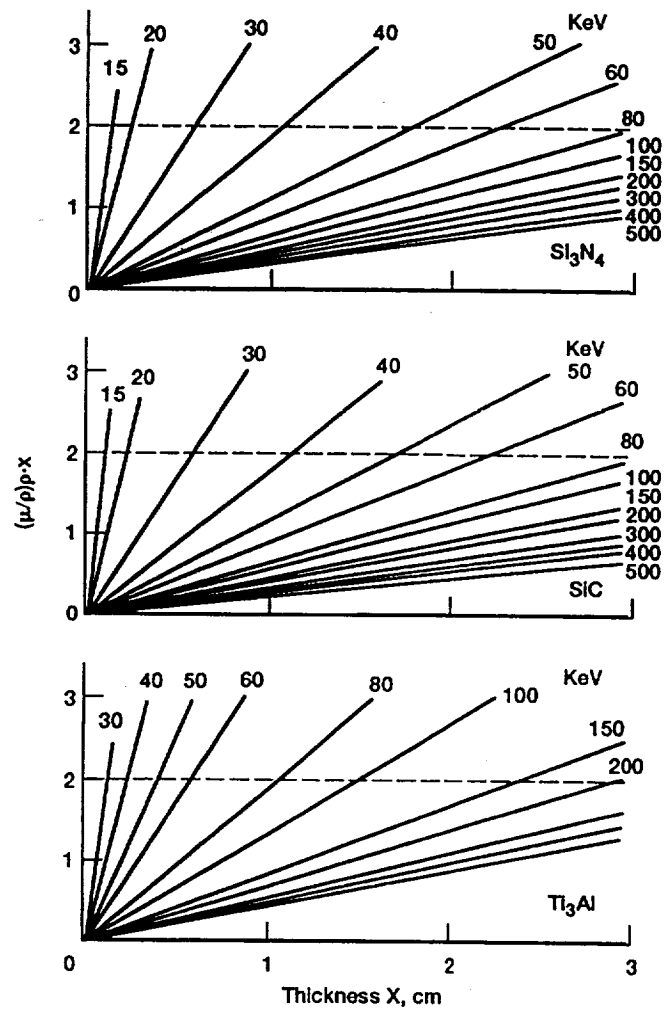


Figure 3.9.— μx versus thickness x for Si₃N₄, SiC, and Ti₃Al.

energy for increased specimen thicknesses is needed in order to obtain a μx_m between 1 and 2. μx_m between 1 and 2 assures an optimum energy (Gardner and Ely, 1967) minimizing errors due to statistical counting rate fluctuations and instrumentation characteristics. The data shown in figures 3.8 to 3.11 and listed in Tables E.1 and E.2, are calculated by extracting the total mass attenuation coefficients from Hubbell (1982) and using densities of 3.16, 3.21, 5.12, 5.8, 6.0, and 19.3 g/cm³, for Si₃N₄, SiC, Ti₃Al, FeAl, NiAl, and W, respectively.

Figure 3.10 shows the attenuation of photons as a function of thickness for silicon carbide, silicon nitride, and titanium aluminide. These values are computed based on equation 2.5 at 40, 50, 60, 80, and 100 keV. Figure 3.11(a) shows the attenuation of photons versus photon energy at a specified thickness of 0.5 cm, and figure 3.11(b) shows the attenuation of photons as a function of thickness at 50 keV for Si₃N₄, SiC, Ti₃Al, FeAl, and NiAl.

Figure 3.11 also indicates the need for using higher energies, between 30 to 100 keV, to discern differences in attenuation between silicon carbide and silicon nitride samples or within the samples. Consequently, the PSDR system was designed with the above considerations in mind to better characterize silicon carbide and silicon nitride samples and possibly silicon carbide fiber reinforced reaction bonded silicon nitride composite samples.

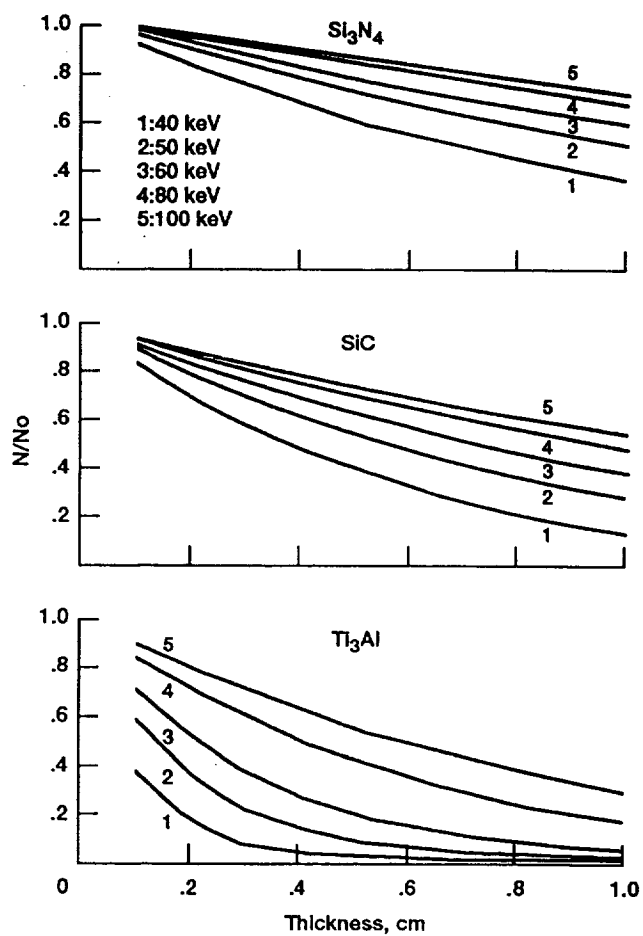


Figure 3.10.—Attenuation of photons versus thickness for Si_3N_4 , SiC , Ti_3Al

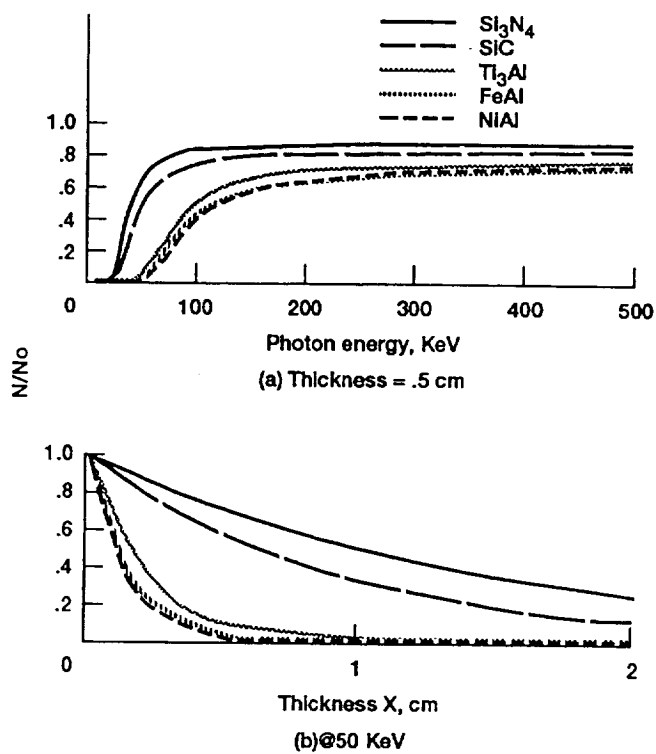


Figure 3.11.—Attenuation of photons (a) versus KeV for 0.5 cm thickness and (b) versus thickness at 50 keV.

Results and Discussion

Tungsten fiber

A 75 μm tungsten fiber with a lead spatial reference is scanned in air. The tube potential was 50 kV and the tube current is 34 mA. The source to fiber distance is 33 cm and the source to detector distance is 69 cm. The step size is 25 μm in the horizontal direction and 50 μm in the vertical direction. The scan (Fig. 3.12) included ten vertical steps and two hundred horizontal steps. A 3-D representation of the digital radiographic data and 2-D selected profiles are also shown in figure 3.12. Figure 3.13 shows one line profile of photon counts versus position exactly over the fiber.

The tungsten fiber and the lead reference are successfully imaged as shown in figure 3.12. Approximately 3000 photons are attenuated by the tungsten fiber over the background attenuation in air. Because of the cylindrical shape of the fiber the photon counts vary considerably over the fiber from a minimum of 13220 counts to a maximum of 15280 photons with a relatively high standard deviation of 639 photons.

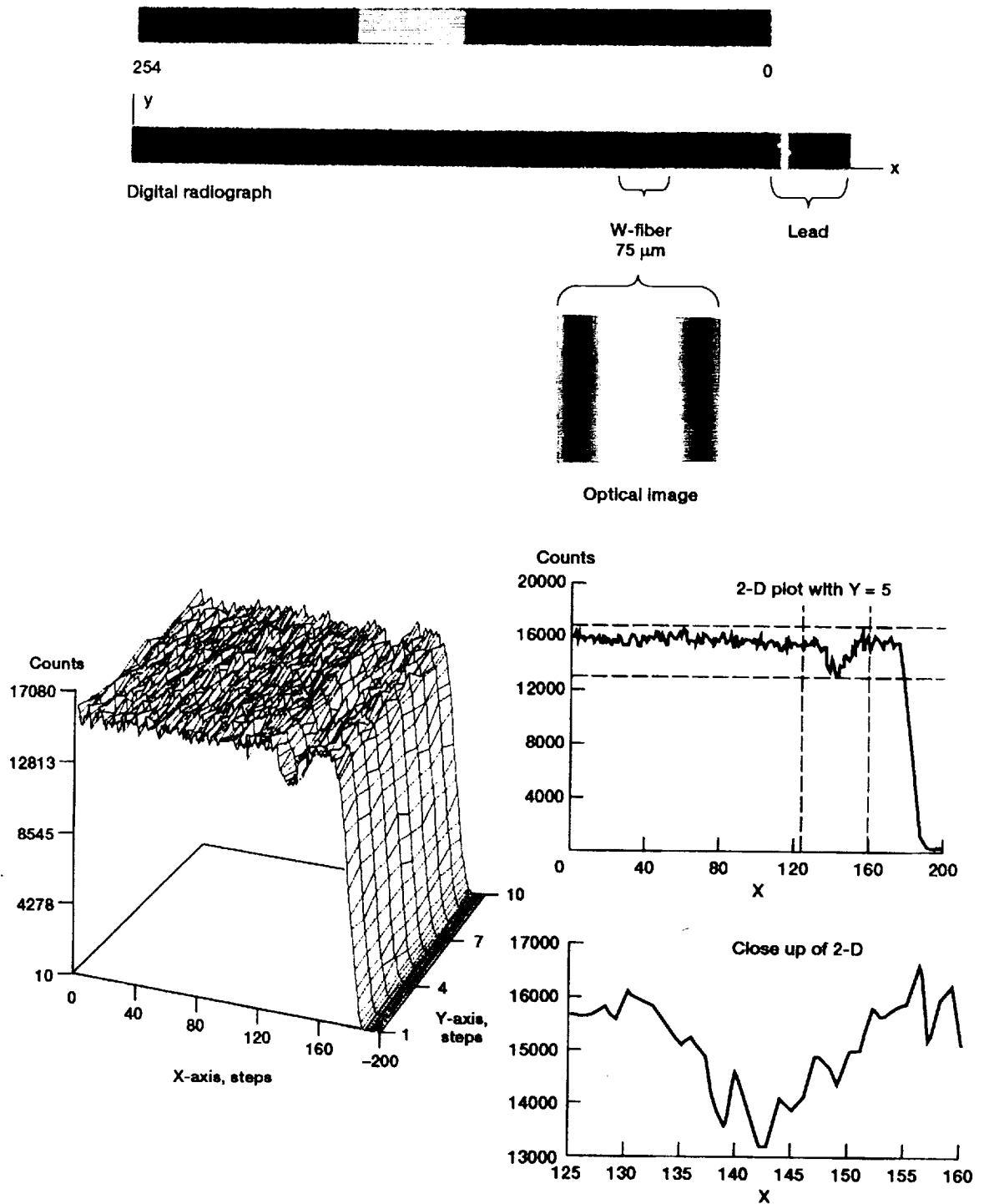


Figure 3.12.—Digital radiograph and 3-D and 2-D plots of a tungsten fiber in air.

ORIGINAL PAGE
COLOR PHOTOGRAPH

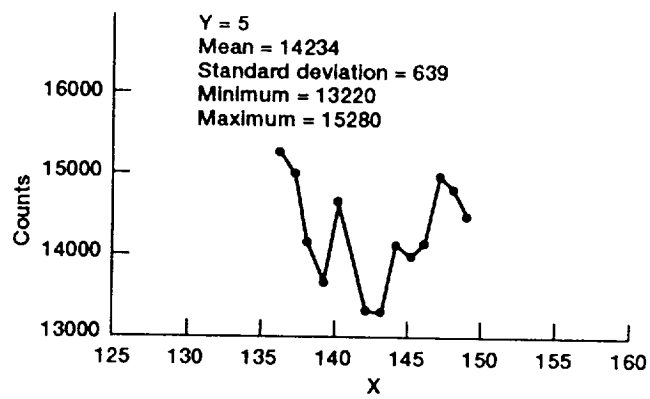


Figure 3.13.—2-D plot of photon counts passing through a tungsten fiber versus position.

Silicon carbide fibers

A silicon carbide fiber, 142 μm in diameter, with a lead frame serving as a spatial reference are scanned in air. Figure 3.14 shows the digital radiograph of the fiber area acquired at 45 kV tube potential and 35 mA tube current. Figure 3.15 shows a digital radiograph area of the fiber at 50 kV tube potential and 35 mA tube current. Figure 3.16 shows a digital radiograph of one W fiber and four SiC fibers in air. The scans for figures 3.14, 3.15, and 3.16 are of 300 horizontal steps by 100 vertical steps where the step size is 10 μm in both directions.

It is evident from figures 3.14 and 3.15 that the existing system does not have the capability of detecting a SiC fiber in air. The displayed data shows the presence of the lead reference and does not indicate the presence of the SiC fiber. Contrast stretching the area where the fiber is located does not enhance the fiber detection capability.

In addition, figure 3.16 emphasizes the inability of the system to differentiate between air and SiC fibers. This implies similar detection problems in the case of imaging SiC fibers in Si_3N_4 matrix. Voids in silicon nitride are more detectable than SiC fibers are because the $\Delta\mu$ is smaller in the fiber case, $[C_{\text{sub}}]_{\text{fiber}} = [\mu_{\text{matrix}} - \mu_{\text{fiber}}] [\text{fiber diameter}]$, than in the void case, $[C_{\text{sub}}]_{\text{void}} = [\mu_{\text{matrix}} - \mu_{\text{air}}] [\text{void diameter}]$.

PAGE 76 ~~INTERNATIONALLY BLANK~~

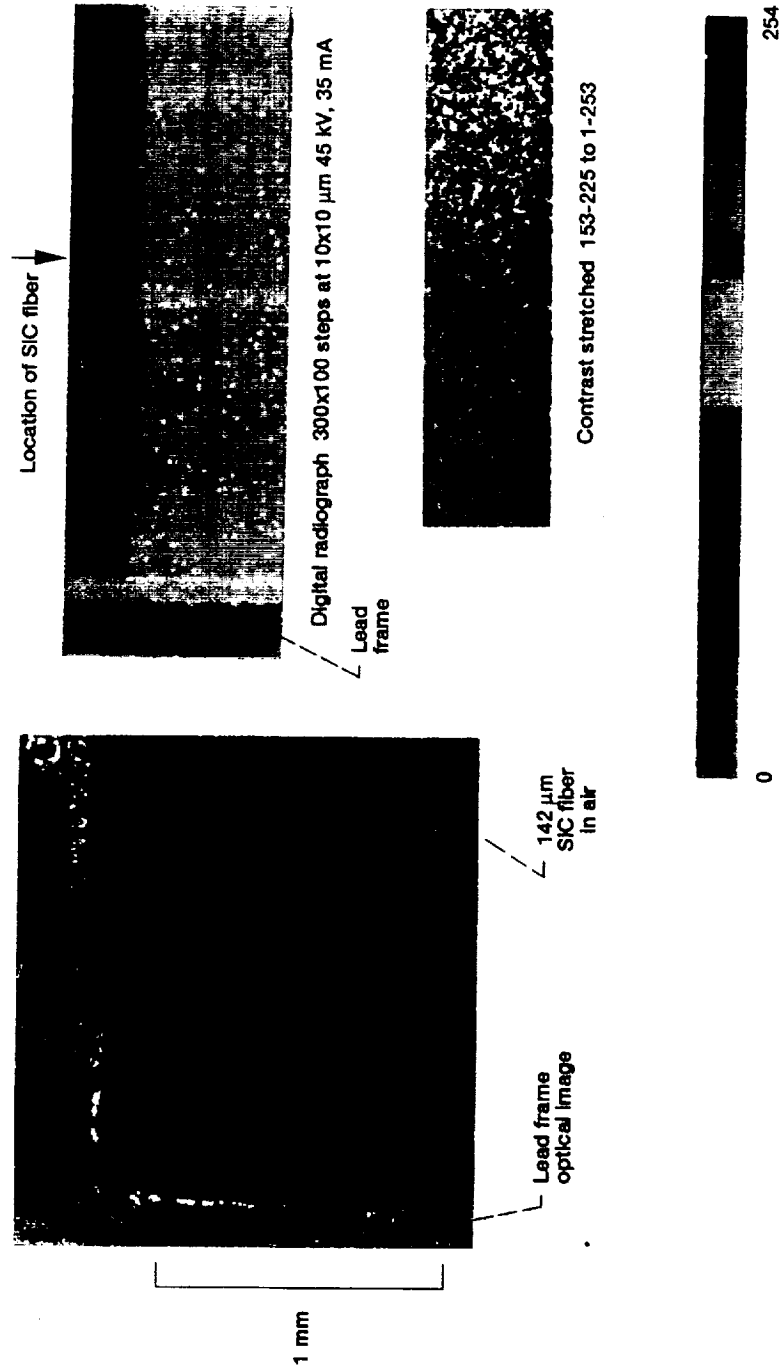


Figure 3.14.—Digital radiography Of a SIC (SCS-6, 142 μm) fiber in air at 45 kV tube potential.

ORIGINAL PAGE
COLOR PHOTOGRAPH

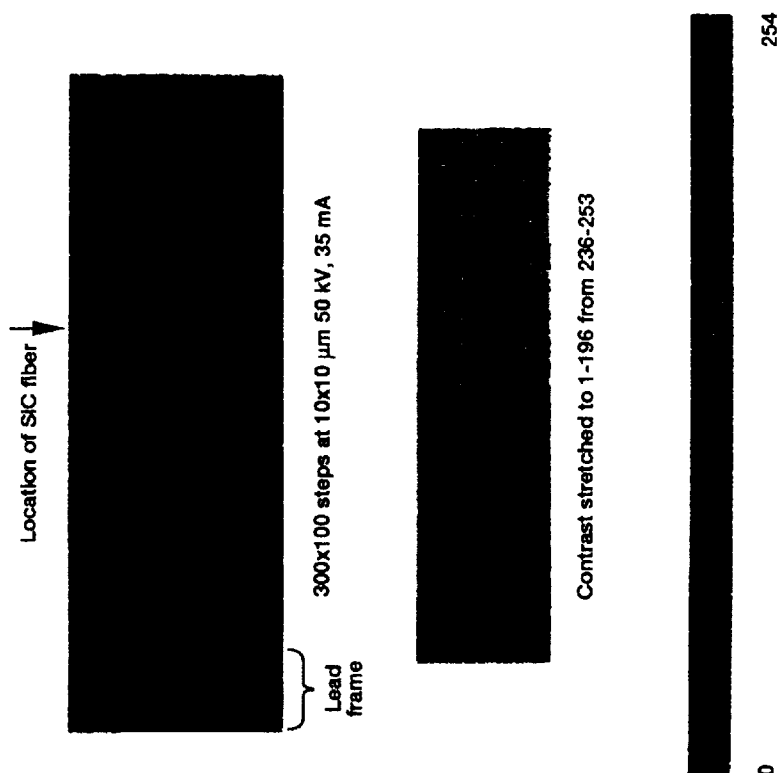
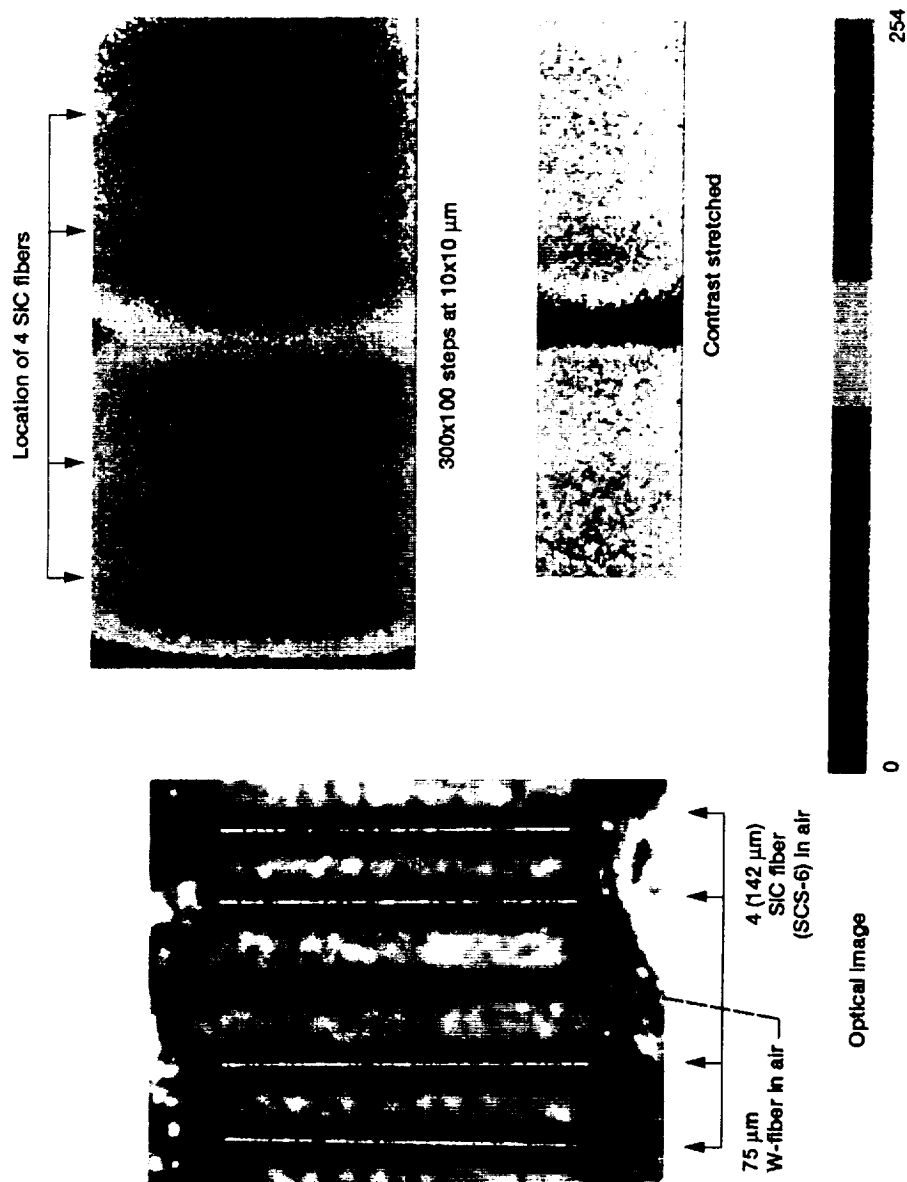


Figure 3.15.—Digital radiography of the same SIC fiber shown in figure 3.14 at 50 kV tube potential.

ORIGINAL PAGE
COLOR PHOTOGRAPH



ORIGINAL PAGE
COLOR PHOTOGRAPH

87 ~~REDACTED~~ INTENTIONALLY BLANK

Scans of the region of interests (couple mm^2), by varying the time from 5 to 14 hours with sampling photon counts over 0.5 seconds and averaging, did not show sufficient detectability improvement.

Silicon nitride bar

A silicon nitride modulus of rupture (MOR) bar is scanned. The bar dimensions are 0.6 cm wide, 0.35 cm thick, and 3.0 cm long. The tube potential is 50 kV and the tube current is 34 mA. The source to sample distance is 33 cm and the source to detector distance is 69 cm. The step size is 25 μm in the horizontal direction and 50 μm in the vertical direction. The scan (Fig. 3.17) includes part of the original scan where 200 vertical steps by 500 horizontal steps are traversed.

The digital radiograph successfully detected the steel spring holder, the silicon nitride sample, and the anticipated high density case-low density core within the silicon nitride sample (Sanders and Baaklini, 1988). Contrast-stretching further enhanced the density difference between the case and the core of the nitride sample.

From figure 3.17 the ratio $N_{\text{Si}_3\text{N}_4}/N_{\text{air}}$ is about 0.25 in the case region and about 0.42 in the core region. This observation is a markedly different result than that obtained with monochromatic radiation ($N/N_0 = 0.8$), (Figs. 3.10

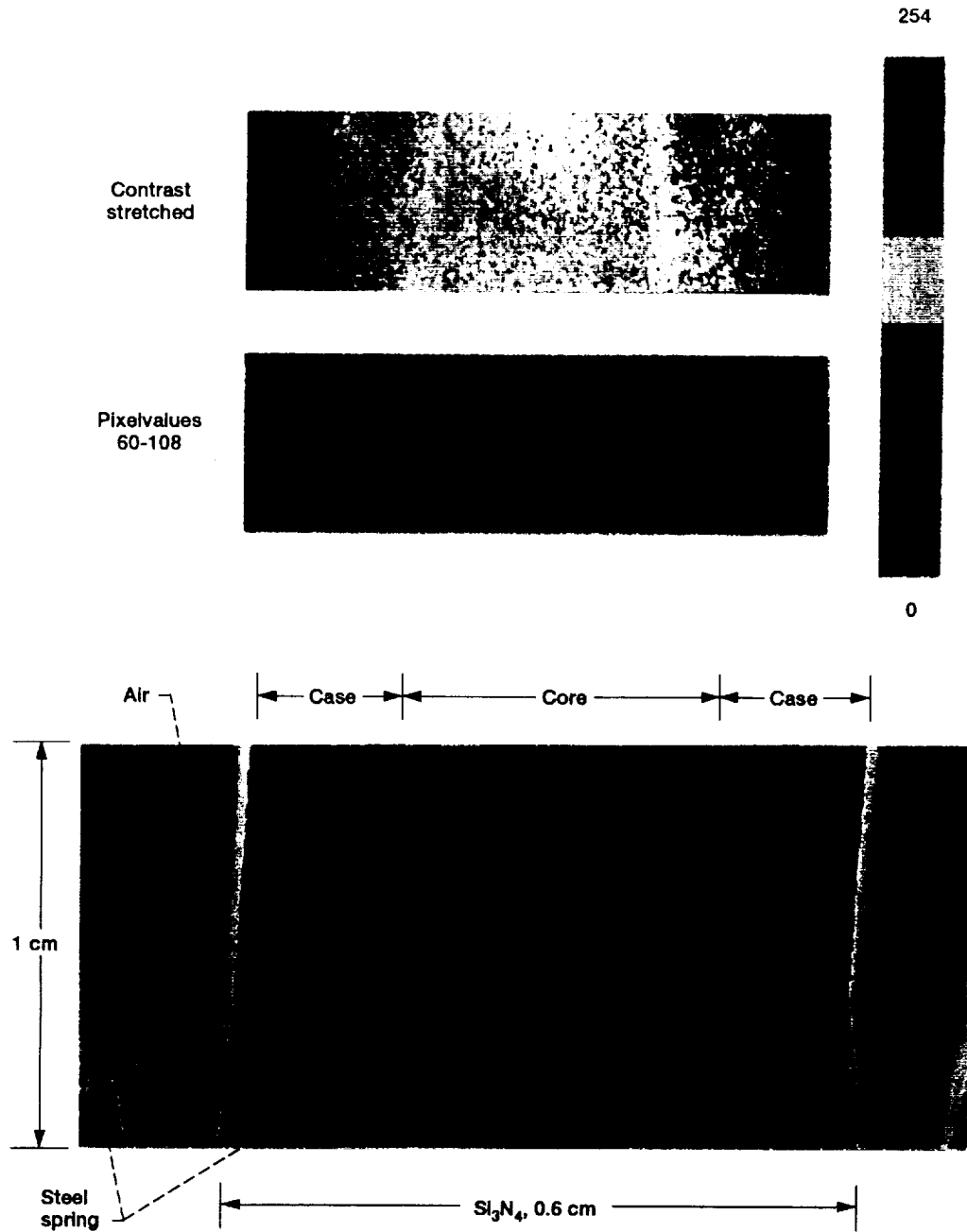


Figure 3.17.—Digital radiography of a Si_3N_4 sample in air.

ORIGINAL PAGE
COLOR PHOTOGRAPH

PRECEDING PAGE BLANK NOT FILMED

86 INTENTIONALLY BLANK

and 3.11). The PSDR system can be used to precisely study the attenuation mechanisms in polychromatic radiation experiments by incorporating a multichannel analyzer and a higher energy and flux density source.

The major limiting factors in the PSDR system are the focal spot size and beam profile. This was because it was necessary to choose an x-ray diffraction tube instead of the Cu or Mo radiographic tubes because of procurement restrictions.

It was shown that with minor modifications the PSDR system is a viable tool for imaging subtle density variations in monolithic ceramics. However, this system is not appropriate for in-situ monitoring of ceramic matrix composites under tensile loading because 1) data acquisition is too time consuming, and 2) a major modification to the system must be made before the necessary contrast sensitivity for imaging the composite constituents is possible.

Conclusion

A PSDR system was developed with microcollimation on the order of 100 μm . The system is viable for characterizing density variations in monolithic ceramic specimens, and for studying x-ray tube profiles. The

system, with minor modifications, can provide for detailed studies of x-ray attenuation mechanisms using polychromatic radiation sources. Modifications are needed before the PSDR system can be used for in-situ monitoring of CMC samples under tensile loading.

CHAPTER IV
CHARACTERIZATION OF CERAMIC DISKS AND ENGINE COMPONENTS
USING X-RAY COMPUTED TOMOGRAPHY

Introduction

In this chapter, the capabilities and limitations of XCT for characterizing monolithic ceramics are presented. XCT is applied to silicon nitride disks, a silicon nitride blade, and a silicon carbide rotor. The XCT findings are corroborated with microfocus radiography, scanning acoustic microscopy, and metallography.

Because overall density and density anomalies affect fracture strength and fracture toughness in monolithic ceramics, the emphasis in this chapter is on detecting density variations within selected regions of samples. At present, XCT is the only NDE technology that can adequately characterize the internal spatial density variations of fully densified objects.

Materials and Experimental Procedures

Materials

Silicon nitride disks, a prototype silicon nitride blade, and a prototype silicon carbide rotor were evaluated in this study. Silicon nitride disks (Fig. 4.1) and a blade (Fig. 4.2) were made by the ceramic sintering methodology described in chapter II. The silicon carbide rotor (Fig. 4.3) was fabricated by the injection molding technology described in chapter II.

Systems

X-ray computed tomography (XCT), microfocus radiography, scanning acoustic microscopy (SAM), and optical microscopy were the principal NDE methods applied.

The XCT system, i.e., a LAM/DE⁸ system, used in this investigation is a laminography/dual energy system. LAM/DE is a second generation CT scanner, i.e., a translate-rotate CT scan geometry system. For this geometry, the scanning process consists of translating the specimen or component past the x-ray beam, rotating, and translating past the x-ray beam again until the specimen has been rotated

⁸ Designed and built by Advanced Research and Applications Corporation for the Wright-Patterson Air Force Base, OH.

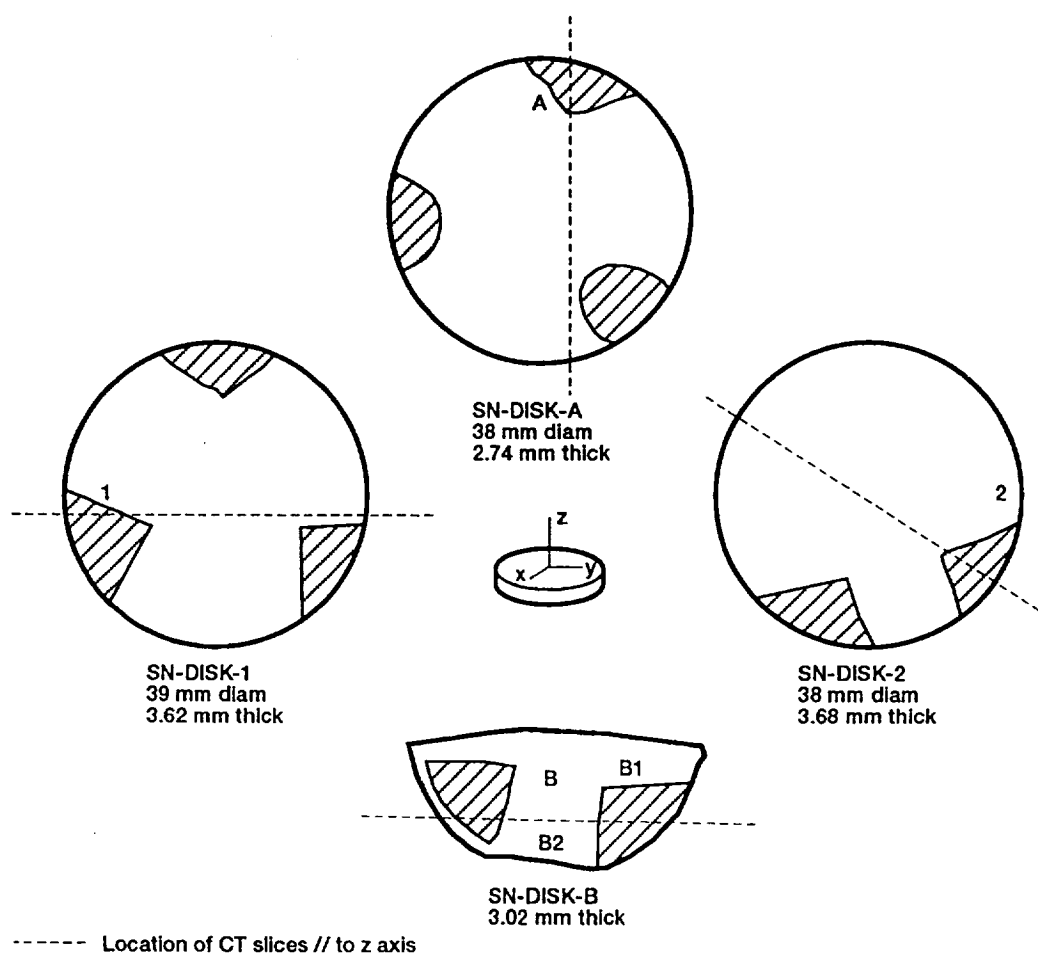


Fig. 4.1.—Schematic of the silicon nitride disks showing the location of the cross-sectional slices (// to z axis) of interest.

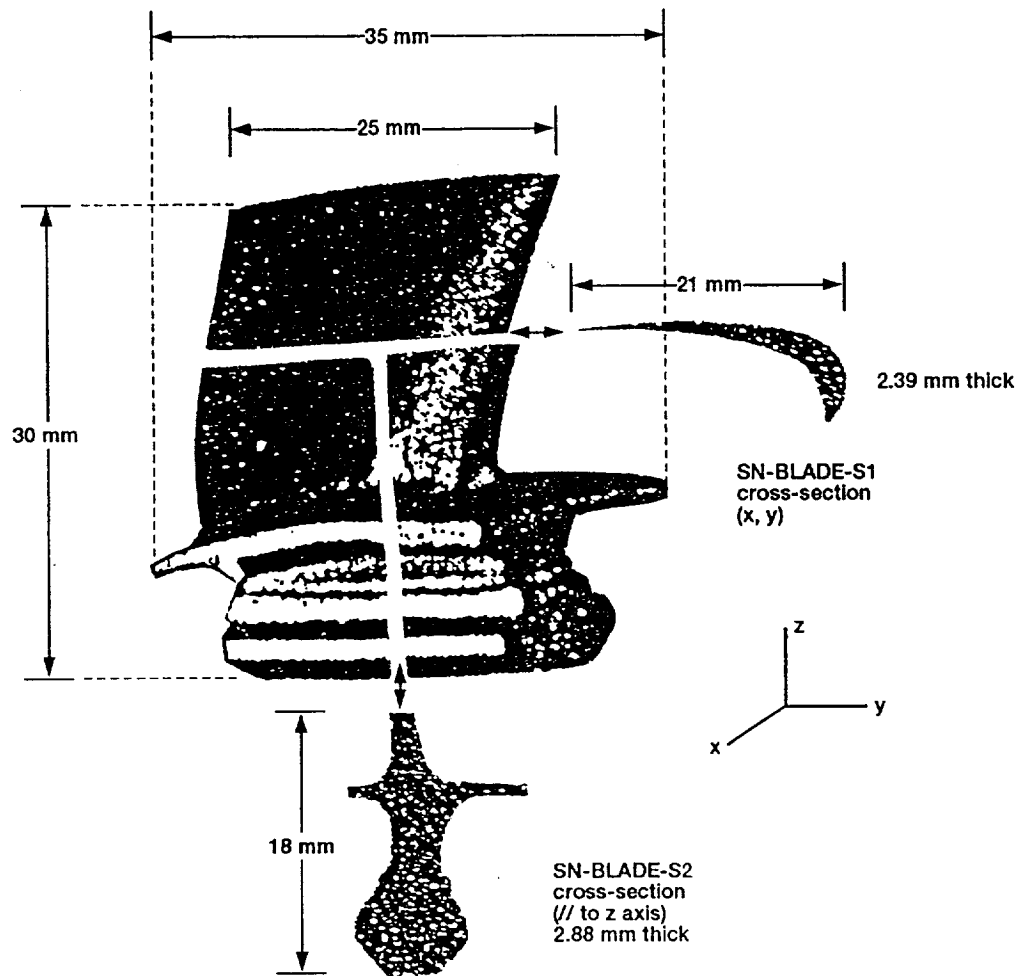


Fig. 4.2.—Sketch of the silicon nitride blade showing the cross-sectional slices of interest.

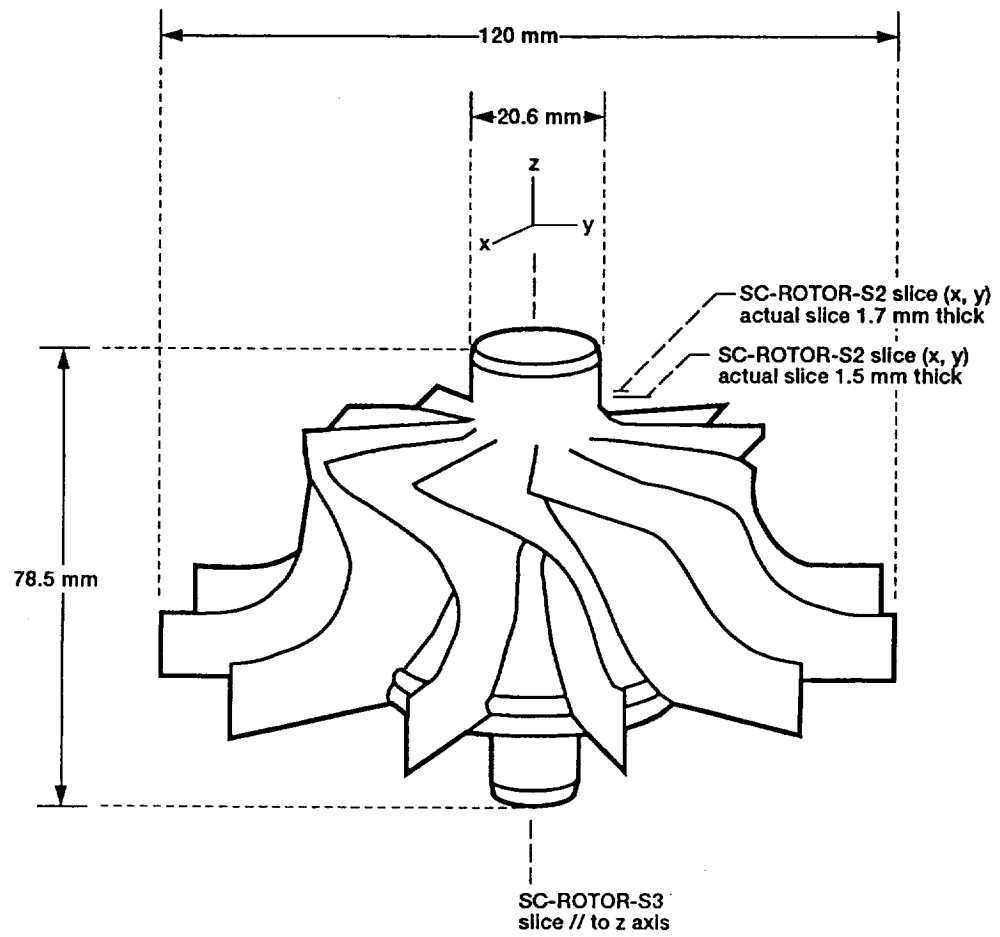


Fig. 4.3.—Schematic of the silicon carbide rotor showing the location of the cross-sectional slices of interest.

180 degrees. LAM/DE includes a 420 kV isovolt x-ray source and a CdWO_4 linear array detector with 128 mm field of view. The x-ray source is collimated to 91.44 cm in the horizontal direction and to 6.35 cm in the vertical direction generating a fan beam. The slice thickness can be adjusted from 1 mm to 15 mm. In this research the slice thickness was approximately 2 mm, the image pixel size was 250 μm , the pixel integration time was 55 ms, and the total scan time per slice was 20 to 30 minutes. A schematic configuration of the scanning geometry of the LAM/DE system is shown in figure 2.8

The microfocus radiographic system with low energy up to 10 W was used to evaluate actual cross-sectional slices. The microfocus system was operated in the projection mode (2 to 4x magnification) and in the 30 to 60 kV range with a beam current of 0.25 to 0.32 mA. The system had a molybdenum anode and a 10 μm focal spot. The detection medium was a Kodak film type M. The film was backlighted and was digitized. The digitized image was color coded to incrementally show radiographic density differences. A schematic of the microfocus projection radiography system is shown in figure 2.1 (c).

A pulse-echo/pulse-reflection scanning acoustic microscope (SAM) system was also applied to the samples using a reduced-aperture lens at a nominal 50 MHz center frequency. The acoustic lens was positioned above the

sample in a distilled water coupling bath. The transducer generated and detected ultrasonic pulses. Stepper motors drove the sample in a raster pattern as the reflected signal amplitude was digitally stored as a function of position. An adjustable delay time between pulse generation and signal digitization allowed imaging of either near surface or subsurface sample slices. A schematic diagram of the lens-specimen configuration is shown in figure 2.9.

Procedures

In-plane (x,y) CT evaluations (Fig. 4.4) are performed on sintered ceramic disks. In addition, selected CT slices parallel to the Z axis (Fig. 4.5) were imaged. One side of each disk was polished for metallographic examination. Thereafter, the disks were radiographically imaged as shown in figure 4.6 and selected optical micrographs were taken as shown in figure 4.7. SN-DISK-B was cut in two pieces B1 and B2 in order to expose the internal microstructure of the CT slice in a plane parallel to the Z axis. The B2 face was polished and selected micrographs were taken as shown in figure 4.8.

CT evaluations are performed on three selected cross sections of the silicon carbide rotor as identified in figure 4.3 and as shown in figures 4.9 through 4.11. Following the CT evaluation, the actual slices SC-ROTOR-S1

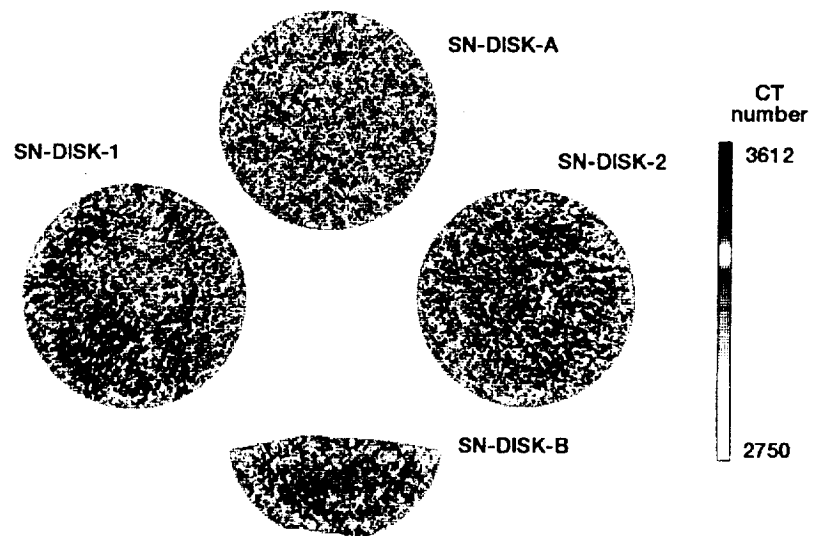


Fig. 4.4.—CT images of in-plane (x, y) slices from the silicon nitride disks.

ORIGINAL PAGE
COLOR PHOTOGRAPH

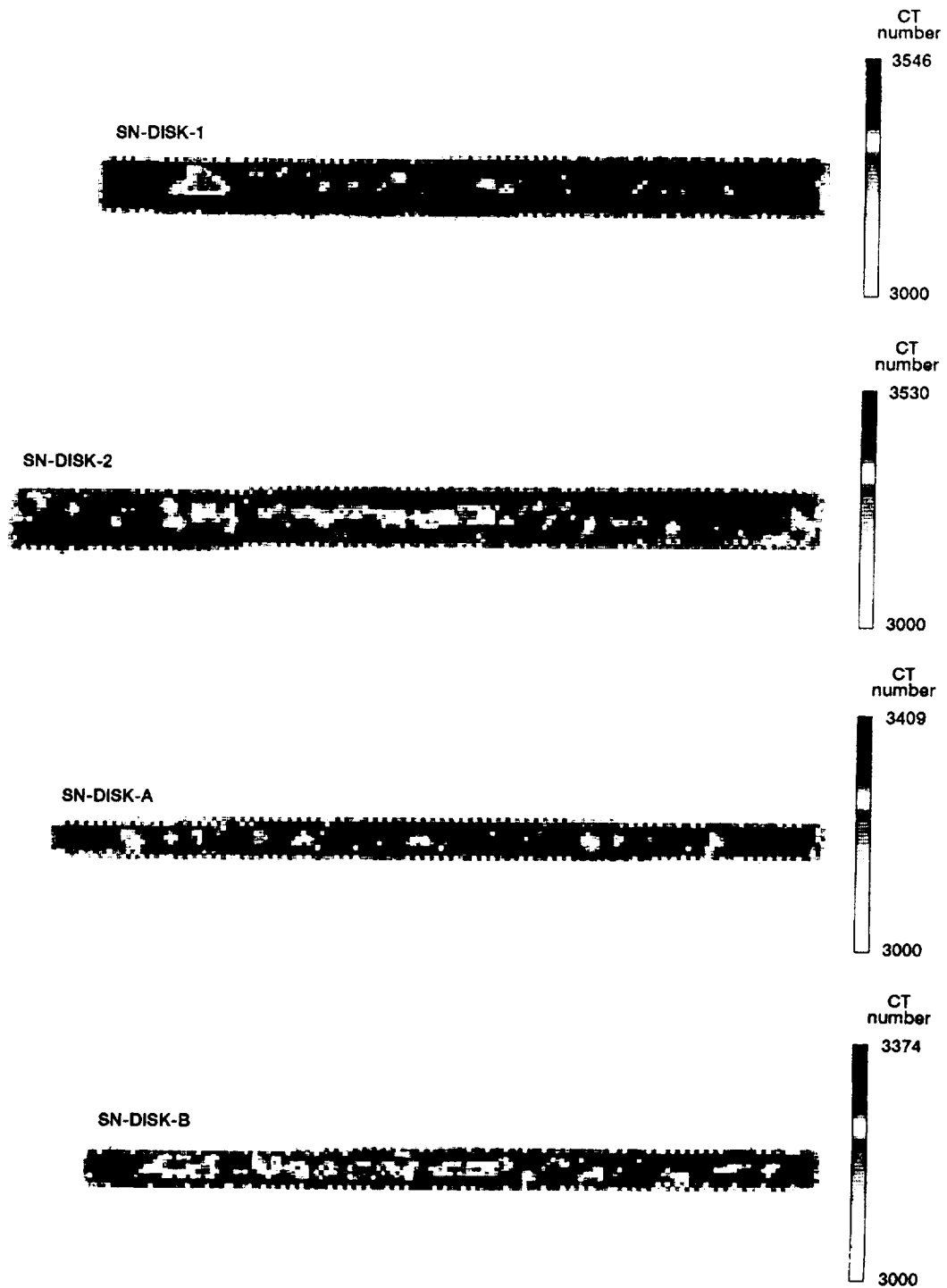


Fig. 4.5.—CT Images of selected slices (// to z axis) as indicated in figure 4.1.

ORIGINAL PAGE
COLOR PHOTOGRAPH

PRECEDING PAGE BLANK NOT FILMED

PAGE 100
UNCLASSIFIED

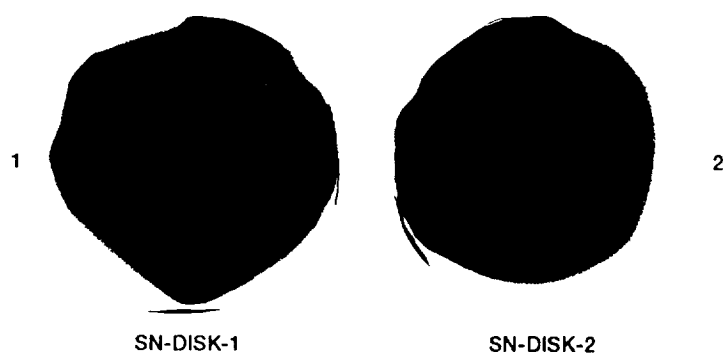


Fig. 4.6.—Through-the-thickness microfocus radiography of disks SN-DISK-1 and SN-DISK-2.

FIG-102 INTENTIONALLY BLANK

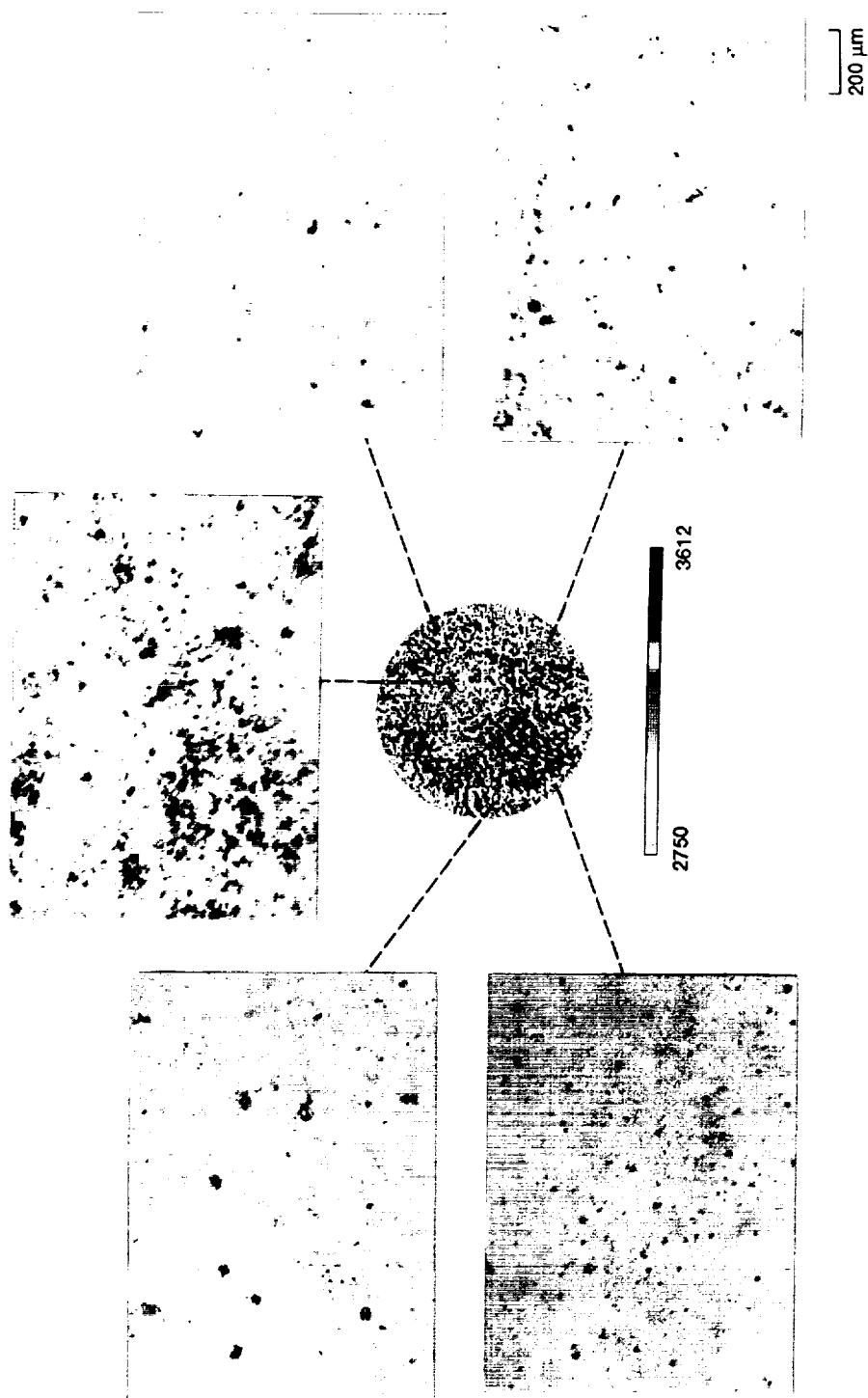


Fig. 4.7.—Optical micrographs highlighting the microstructure of different regions on the polished SN-DISK-1.

PRECEDING PAGE BLANK NOT FILMED

PAGE 104 INTENTIONALLY BLANK

ORIGINAL PAGE
COLOR PHOTOGRAPH

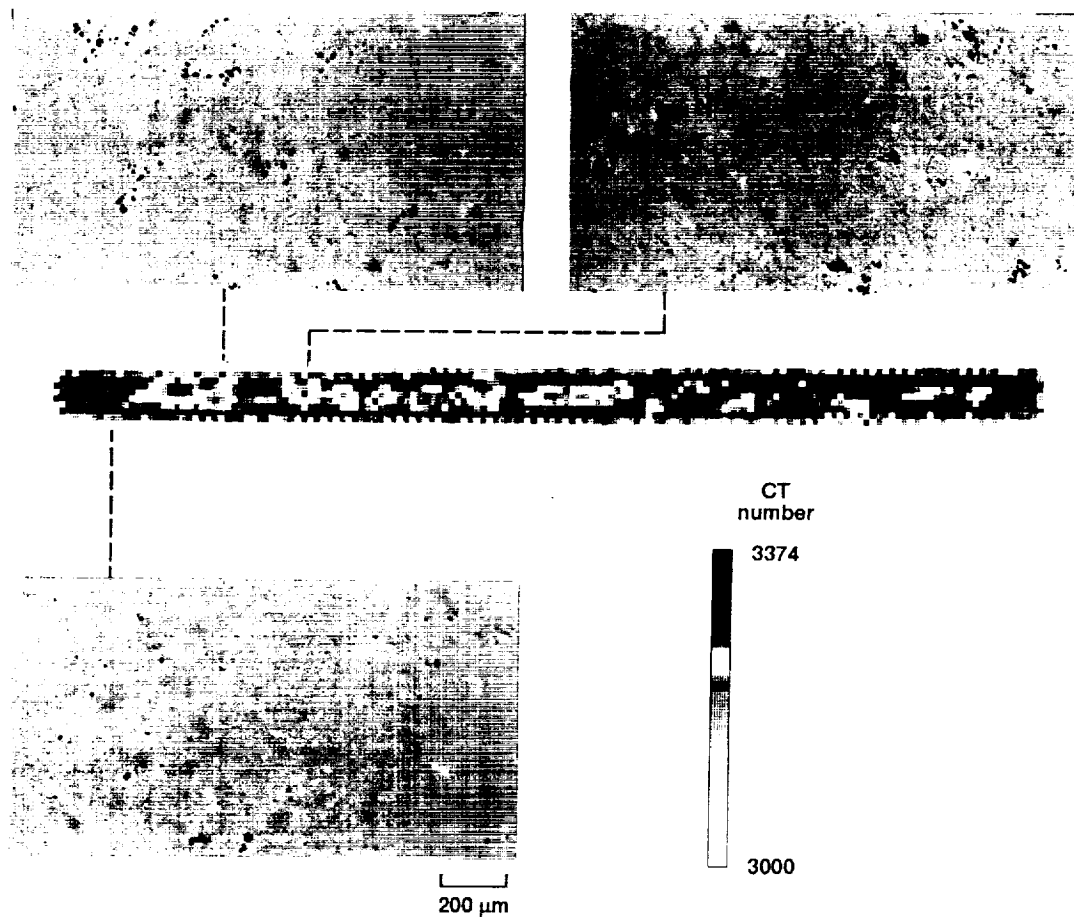


Fig. 4.8.—Optical micrographs highlighting the microstructure of different regions on the polished SN-DISK-B (// to z axis) slice.

ORIGINAL PAGE
COLOR PHOTOGRAPH

106 INTENTIONALLY BLANK

PREVIOUS PAGE BLANK NOT FILMED

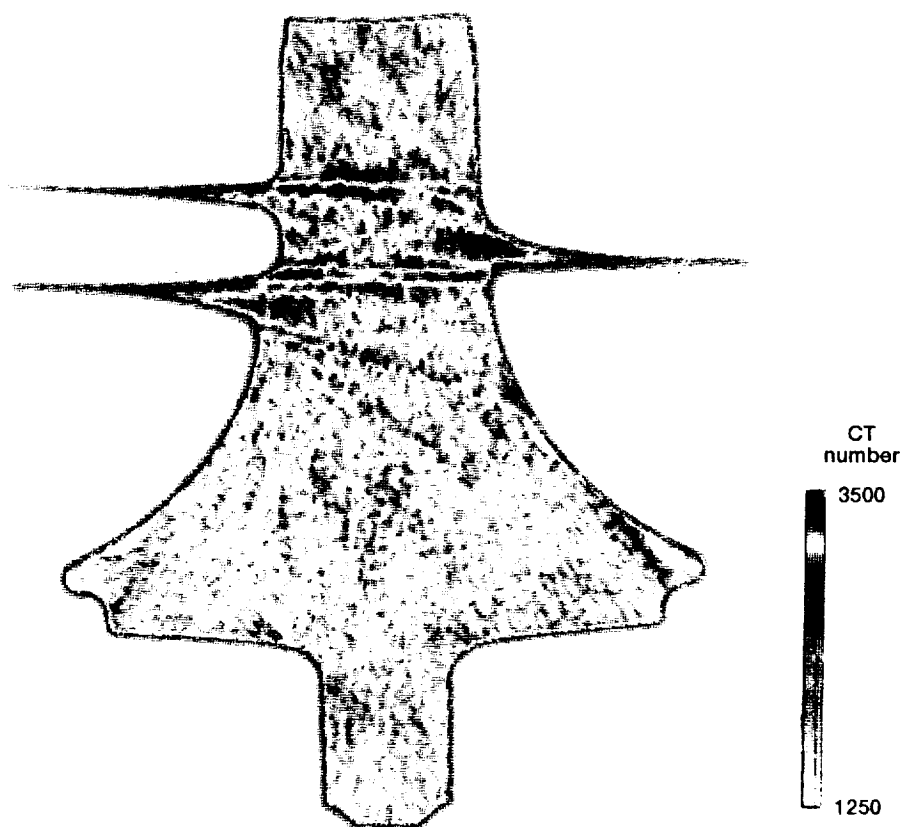


Fig. 4.9.—CT image of the cross-section slice (// to z axis) SC-ROTOR-S3.

ORIGINAL PAGE
COLOR PHOTOGRAPH

PRECEDING PAGE BLANK NOT FILMED

102 INTENTIONALLY BLANK

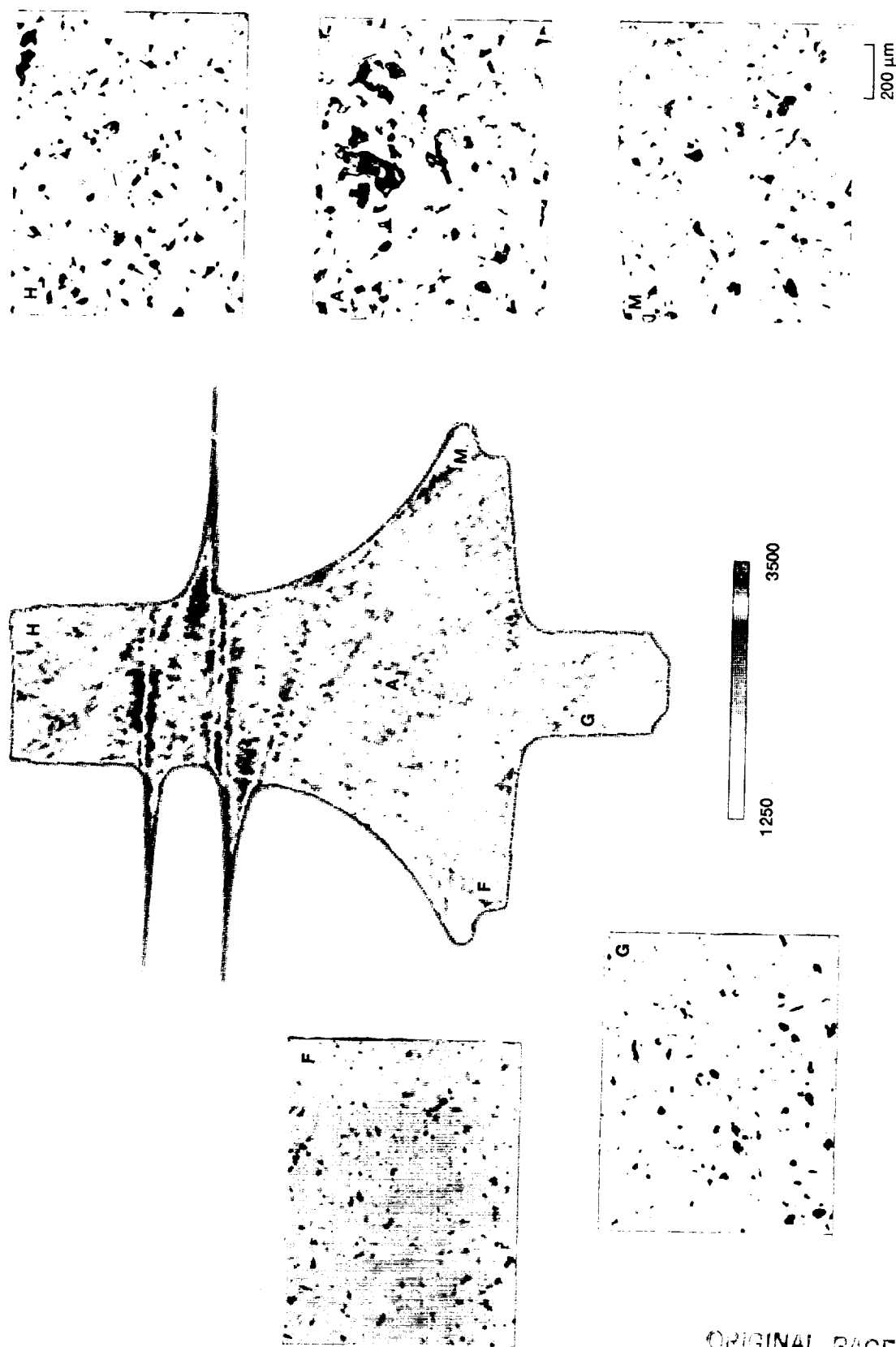
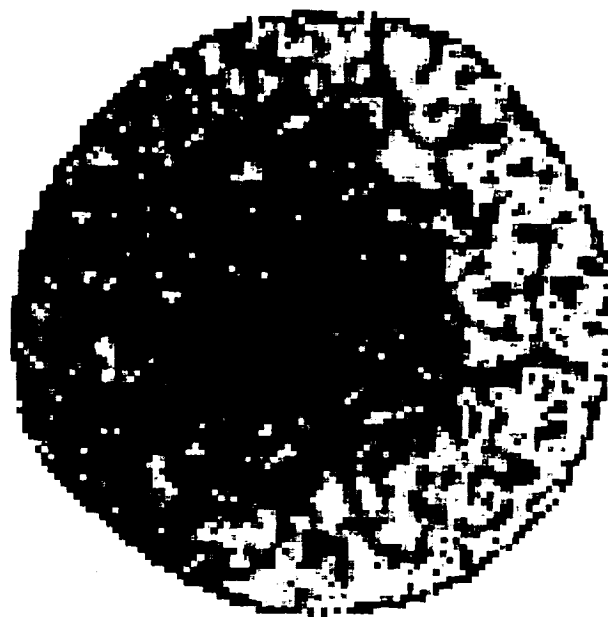


Fig. 4.10.—Optical micrographs highlighting the microstructure of different regions on the polished SC-ROTOR-S3 face.

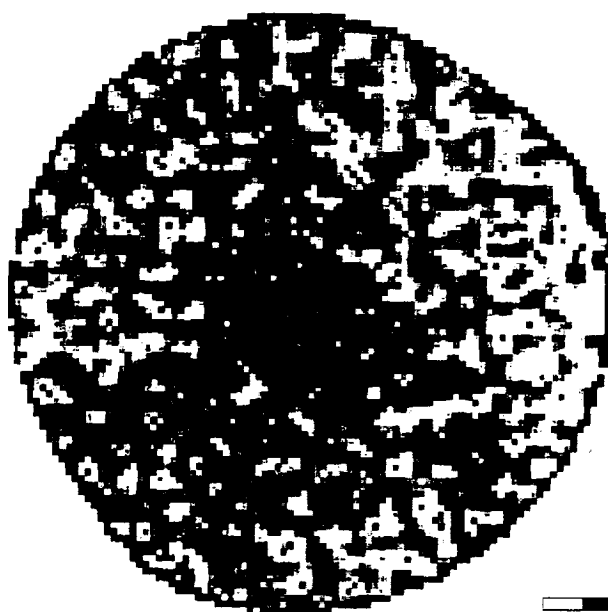
ORIGINAL PAGE
COLOR PHOTOGRAPH

PAGE 110 INTENTIONALLY BLANK

PRECEDING PAGE BLANK NOT FILMED



(a) SC-ROTOR-S1.



(b) SC-ROTOR-S2.

2625 3328

Fig. 4.11.—CT images of the cross-sectional slices.

PRECEDING PAGE BLANK NOT FILMED

ORIGINAL PAGE
COLOR PHOTOGRAPH

PAGE 112

and SC-ROTOR-S2 were cut out from the rotor, then the rotor was cut in approximately two halves exposing two internal faces from SC-ROTOR-S3. One of these faces is polished and characterized metallographically as shown in figure 4.10. One side of the slices SC-ROTOR-S1 and SC-ROTOR-S2 is polished. Thereafter, these slices are radiographed as shown in figure 4.12. Optical micrographs are taken to highlight microstructural porosity variations as shown in figures 4.13 and 4.14. In addition, subsurface scanning acoustic images are made of SC-ROTOR-S1 as shown in figure 4.15.

A CT evaluation of slice SN-BLADE-S1 (Figs. 4.2, 4.16 and 4.17) was performed while the silicon nitride blade was still intact. The SN-BLADE-S1 physical segment corresponding to the CT slice is then cut out of the airfoil. Next CT slice SN-BLADE-S2 is evaluated (Figs. 4.16 and 4.17) and then cut out of the blade/airfoil root of the blade for subsequent metallographic, radiographic (Figs. 4.18 and 4.19), and ultrasonic (Fig. 4.20) evaluation.

Immersion densities were determined by the Archimedean Principle for all silicon nitride disks and all cut-out physical segments (actual slices) of the silicon nitride blade and the silicon carbide rotor (Table I).

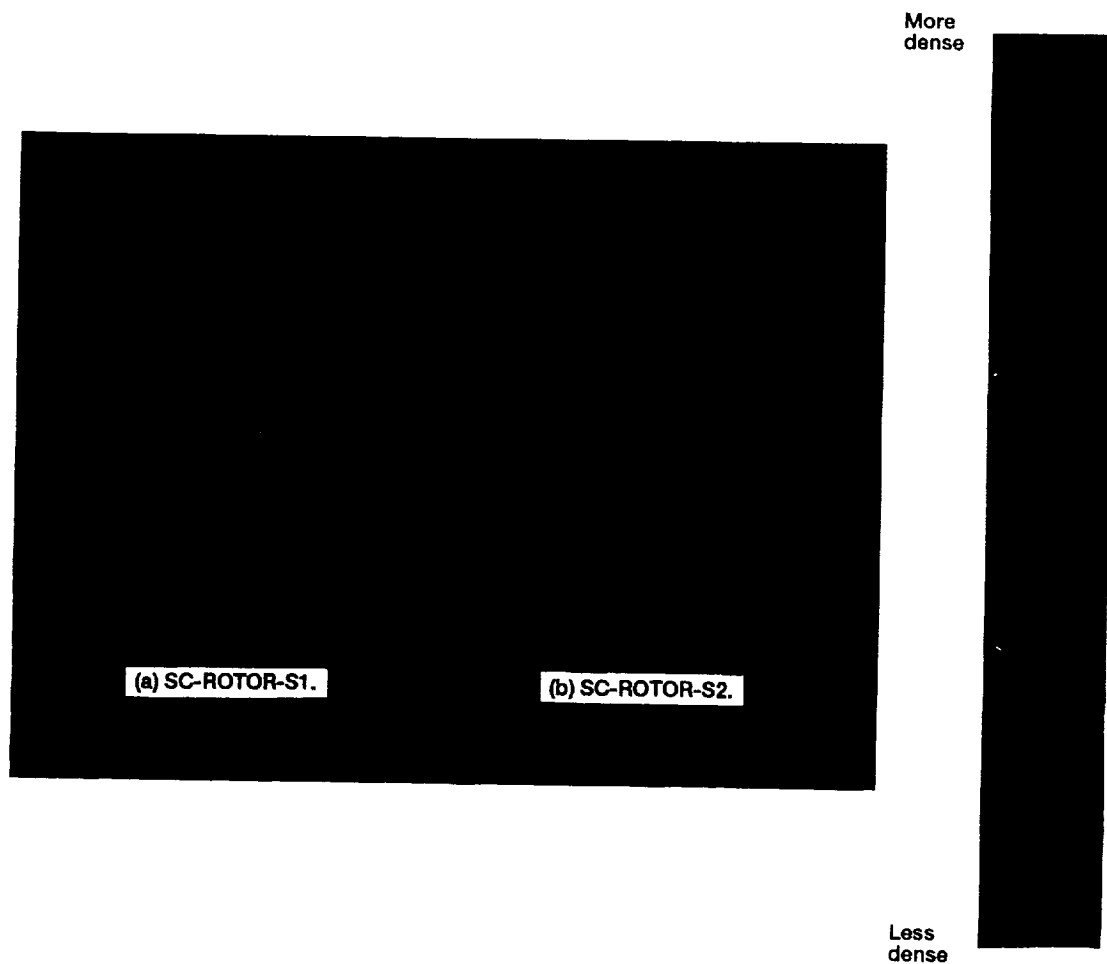


Fig. 4.12.—Radiographic images of the cross-sectional slices.

ORIGINAL PAGE
COLOR PHOTOGRAPH

PAGE 116 INTENTIONALLY BLANK

PRECEDING PAGE BLANK PAGE (11/10/10)

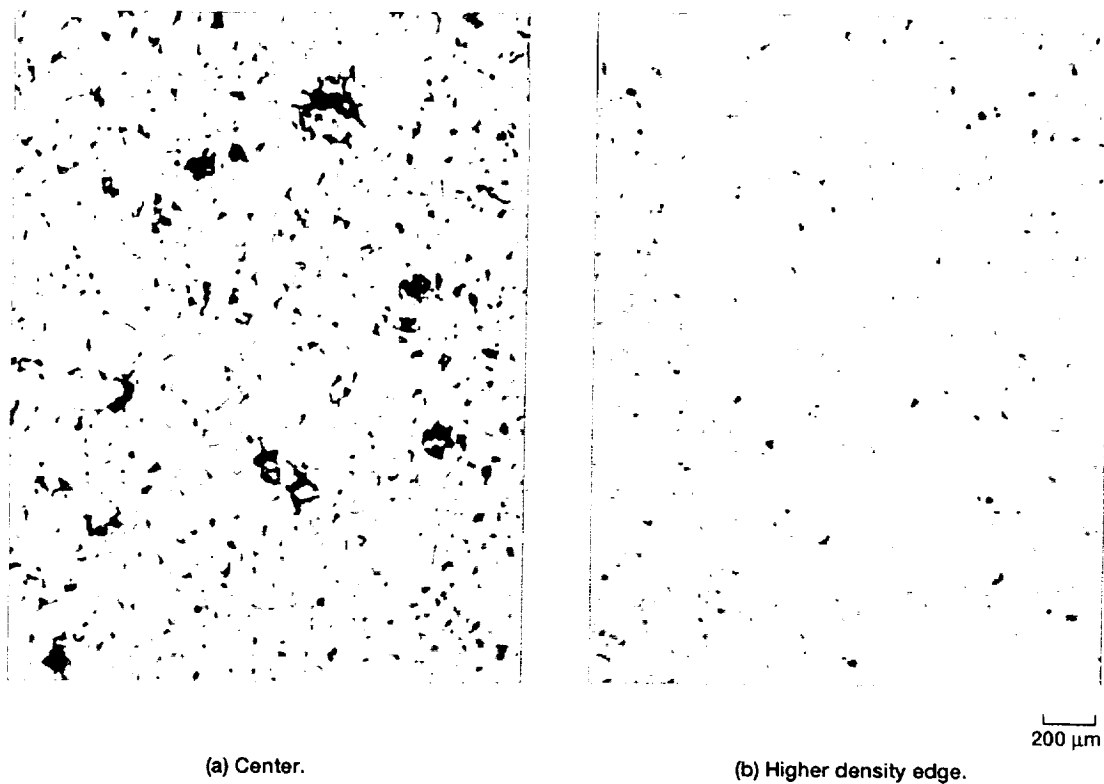


Fig. 4.13.—Optical micrographs highlighting the microstructure of the polished SC-ROTOR-S1 face in (a) the center and in (b) the higher density edge.

ORIGINAL PAGE
COLOR PHOTOGRAPH

7-5

118

INTENTIONALLY BLANK

PRECEDING PAGE BLANK NOT FILLED

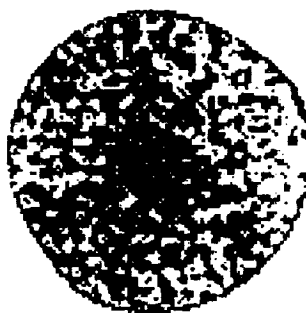
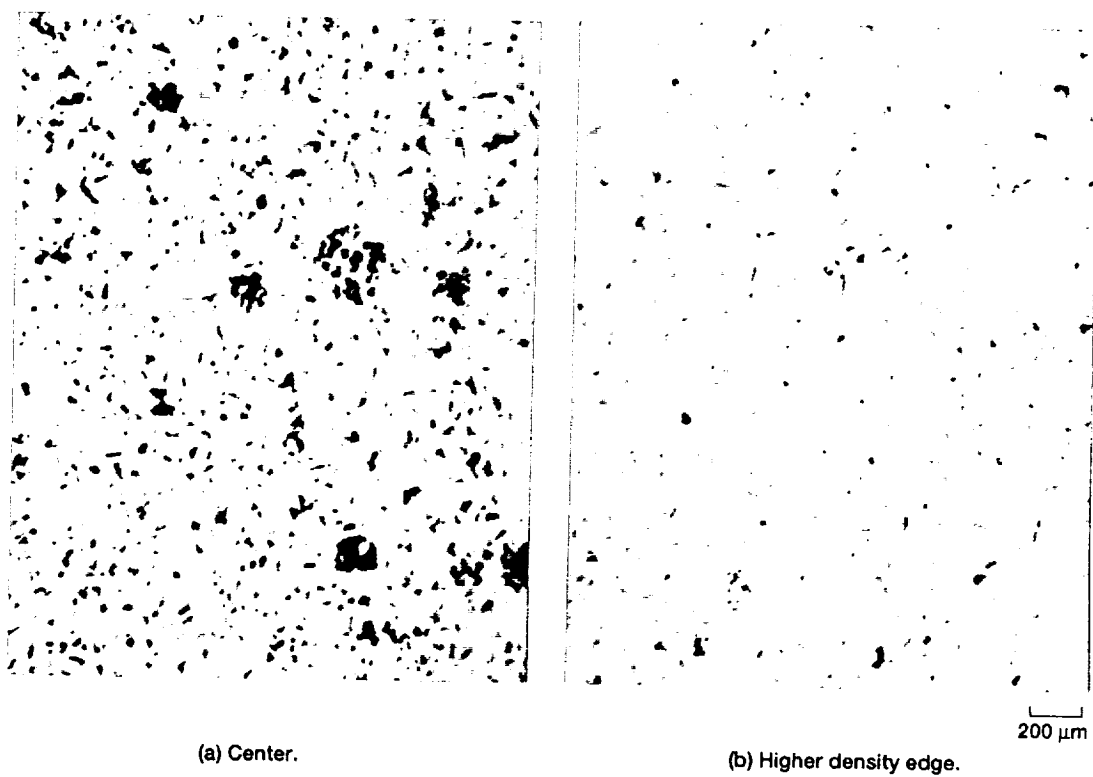
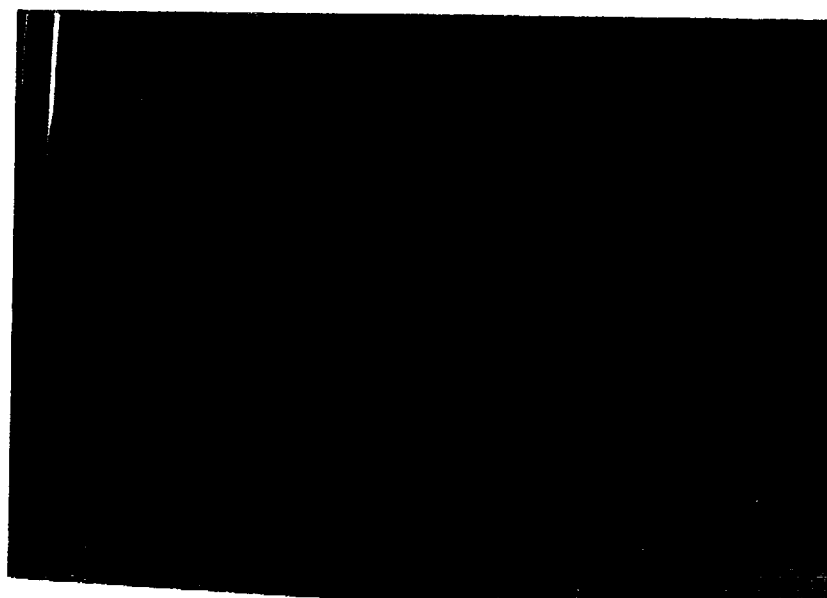


Fig. 4.14.—Optical micrographs highlighting the microstructure of the polished SC-ROTOR-S2 face in (a) the center and in (b) the higher density edge.

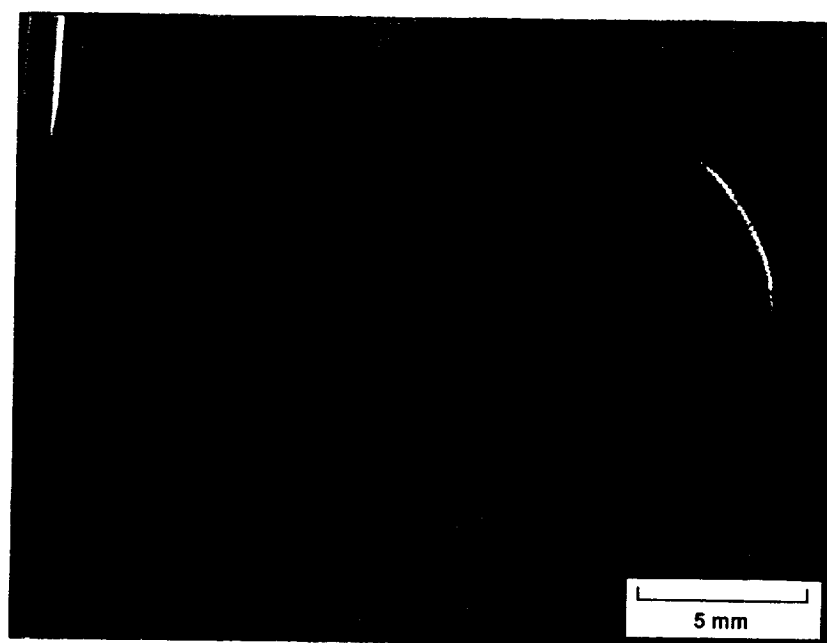
ORIGINAL PAGE
COLOR PHOTOGRAPH

PRECEDING PAGE BLANK NOT FILMED

216 120
INTENTIONALLY BLANK



(a) 1.1 mm below the surface.



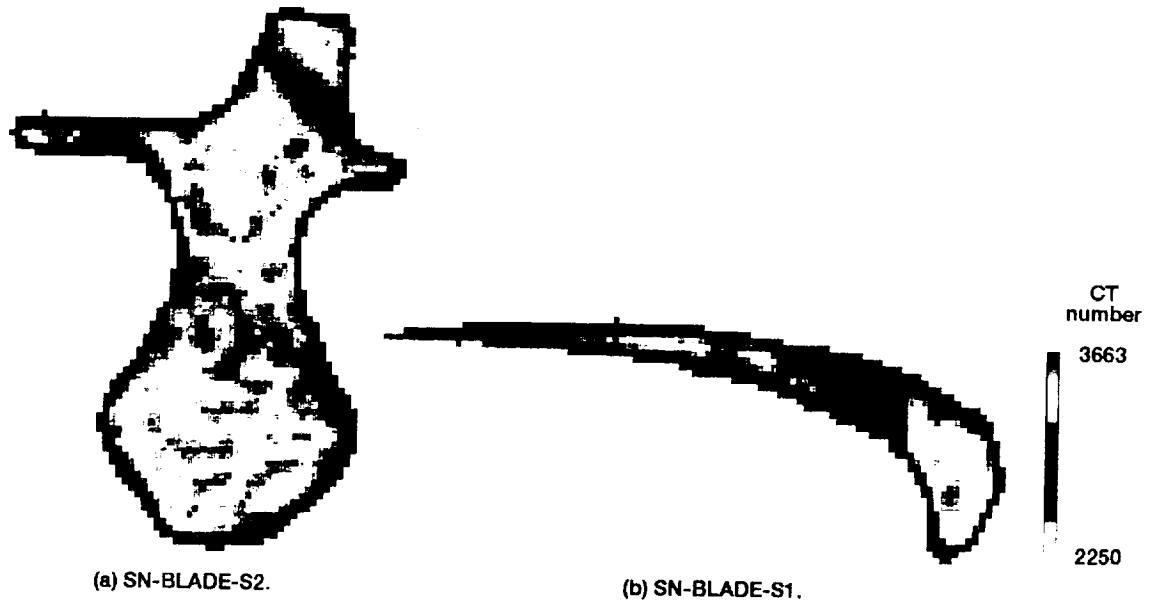
(b) 1.3 mm below the surface.

Fig. 4.15.—Scanning acoustic microscopy images of SC-ROTOR-S1.

ORIGINAL PAGE
COLOR PHOTOGRAPH

PRECEDING PAGE BLANK NOT FILMED

PAGE 128 INTENTIONALLY BLANK



(a) SN-BLADE-S2.

(b) SN-BLADE-S1.

Fig. 4.16.—CT images of the cross-sectional slices.

ORIGINAL PAGE
COLOR PHOTOGRAPH

PROCESSED PAGE 124

PAGE 124

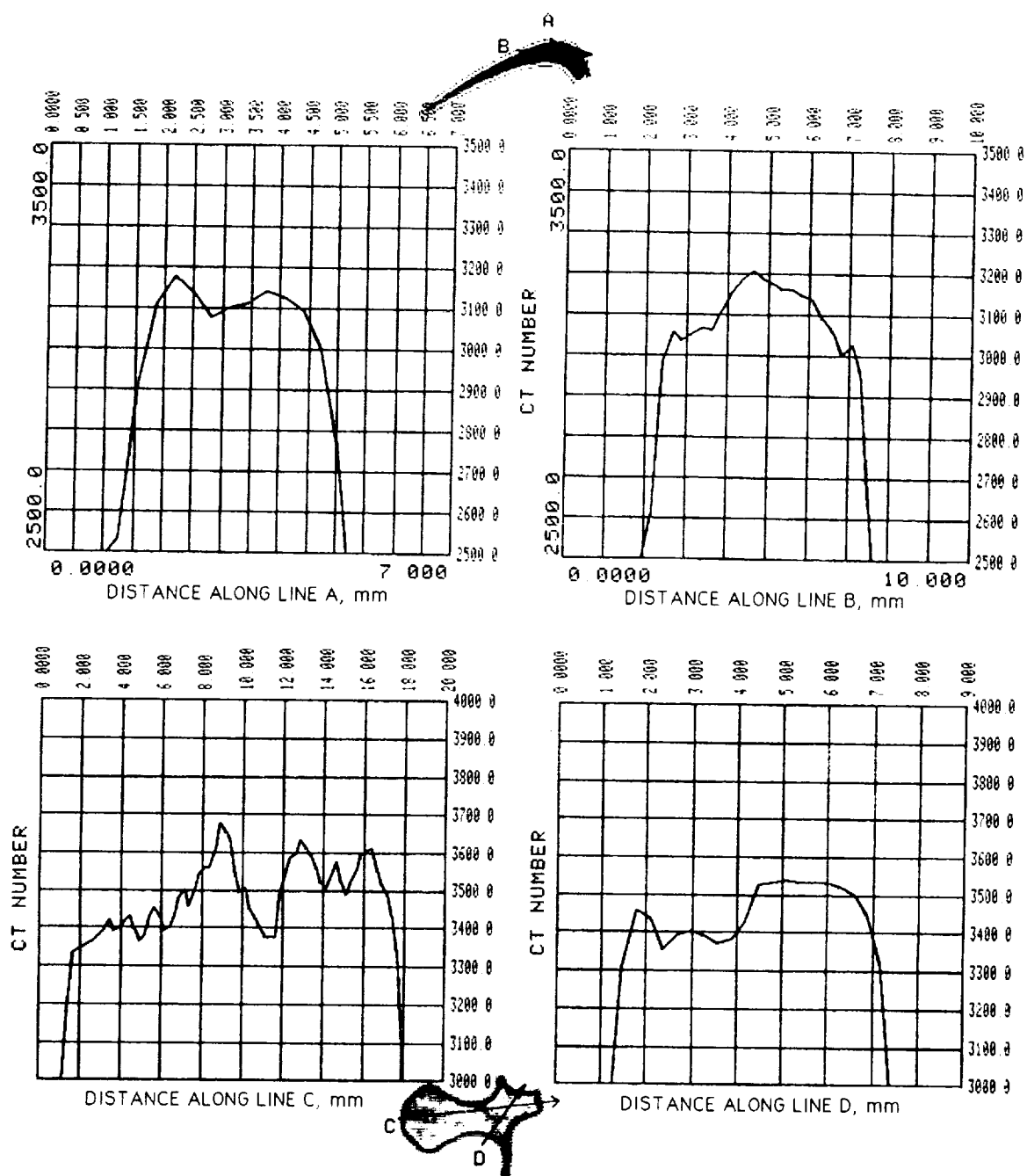


Fig. 4.17.—CT number traces along lines A and B for SN-BLADE-S1 and along lines C and D for SN-BLADE-S2.

ORIGINAL PAGE
COLOR PHOTOGRAPH

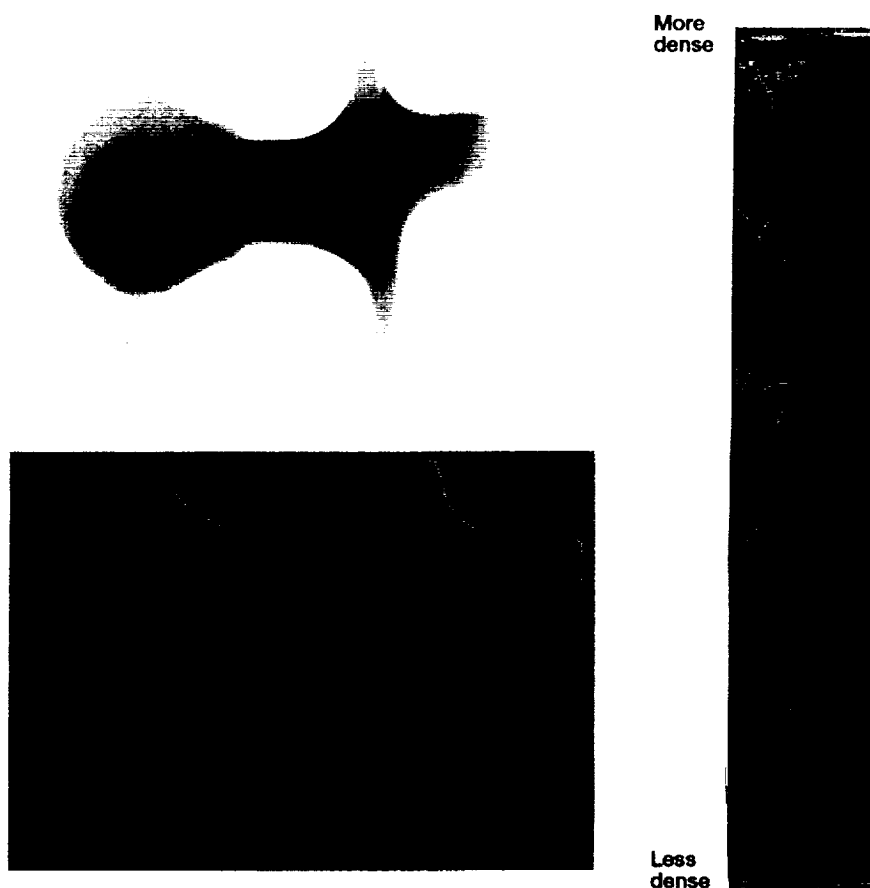


Fig. 4.18.—Radiographic images of the cross-sectional slice SN-BLADE-S2.

ORIGINAL PAGE
COLOR PHOTOGRAPH

PRECEDING PAGE BLANK NOT FILMED

128

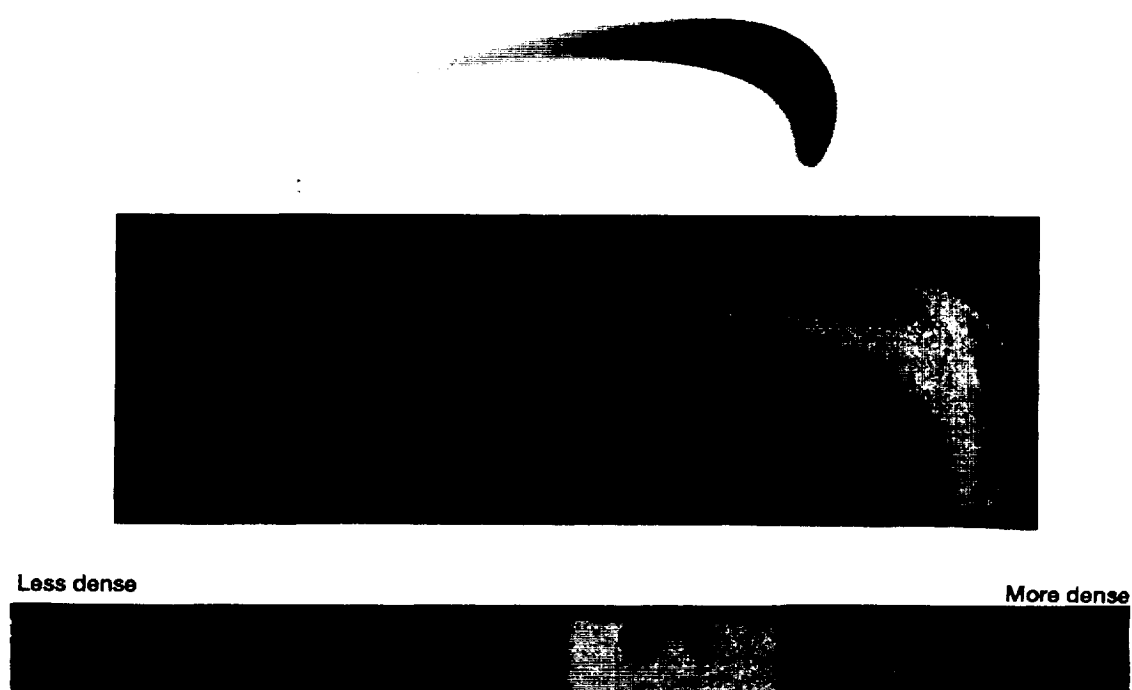
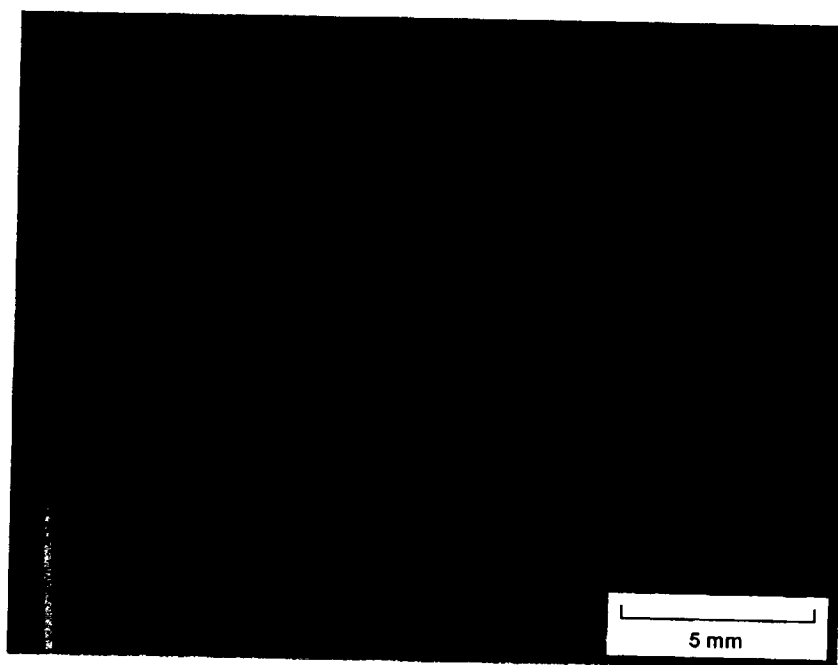


Fig. 4.19.—Radiographic images of the cross-sectional slice SN-BLADE-S1.

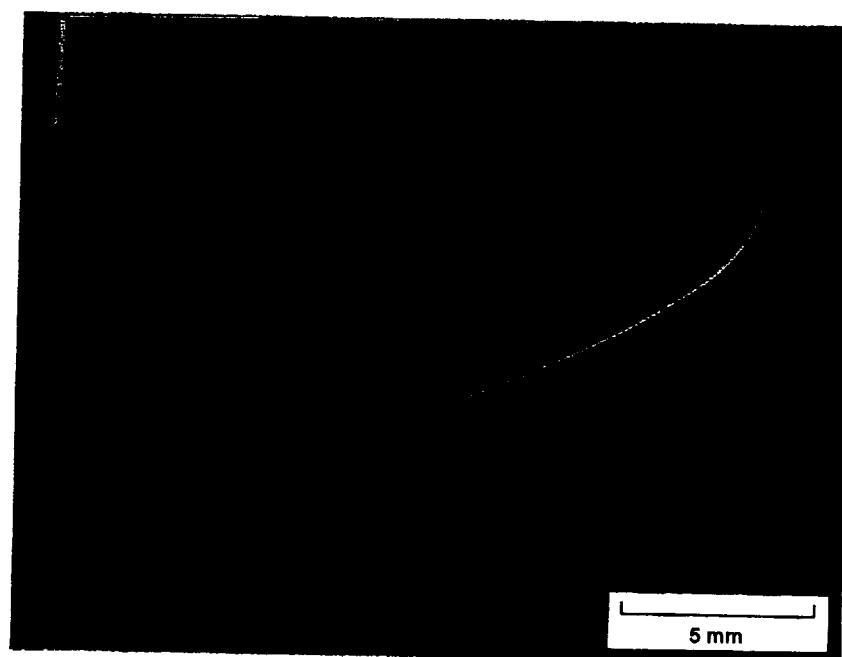
ORIGINAL PAGE
COLOR PHOTOGRAPH

PRECEDING PAGE BLANK NOT FILMED

FIG 130 10/12/1964



(a) SN-BLADE-S2.



(b) SN-BLADE-S1.

Fig. 4.20.—Subsurface scanning acoustic microscopy images.

ORIGINAL PAGE
COLOR PHOTOGRAPH

PRECEDING PAGE BLANK NOT FILMED

138

TABLE I.—DENSITIES AND CT NUMBERS FOR THE SILICON
NITRIDE DISKS, AND THE SLICES FROM THE SILICON
NITRIDE BLADE AND SILICON CARBIDE ROTOR

| Sample | Average CT number | Green density, g/cc | Sintered density, g/cc | Immersion density, g/cc |
|-------------|----------------------|---------------------------|------------------------------|-------------------------------|
| SN-DISK-1 | 3343 | 1.87 | 3.20 | 3.24 |
| SN-DISK-2 | 3347 | 1.91 | 3.16 | 3.25 |
| SN-DISK-A | 3309 | 1.91 | 3.19 | 3.24 |
| SN-DISK-B | 3354 | 1.86 | 3.15 | 3.26 |
| B1 | ---- | ---- | ---- | 3.26 |
| B2 | ---- | ---- | ---- | 3.26 |
| SN-BLADE-S1 | 3100 | ---- | ---- | 3.17 |
| SN-BLADE-S2 | 3250 | ---- | ---- | 3.19 |
| SN-ROTOR-S1 | 2990 | ---- | ---- | 3.10 |
| SN-ROTOR-S2 | 3070 | ---- | ---- | 3.12 |

PRECEDING PAGE BLANK NOT FILMED

Results and Discussion

Silicon nitride disks

The hashed areas in figure 4.1 are regions where the surface of the silicon nitride disks was light gray. The unhashed areas were dark gray. These contrasting areas were attributed to contact with boron nitride spacers between the disks during sintering. The spacers apparently prevented uniform heating and consequently reduced densification of the disk regions in contact with the boron nitride. This a priori knowledge guided the selection of the CT slices (// to Z axis) as indicated in figure 4.1. The objective was to find out whether these low density regions exist throughout the disks.

CT images of in-plane (X,Y) slices (Fig. 4.4) show that the CT number variations are more pronounced in localized regions of SN-DISK-1 than in disks A, 2, and B. Similarly, figure 4.5 shows that the CT number and by implication density variations are quite pronounced near the midplanes of SN-DISK-1 than in SN-DISK-2, SN-DISK-A, and SN-DISK-B. Also, thru-the-thickness microfocus radiography illustrated in figure 4.6 shows that the density of SN-DISK-2 is more uniform than SN-DISK-1.

Optical micrographs from figures 4.7 reveal that more porous, i.e., less dense regions, correspond to the $\text{BN/Si}_3\text{N}_4$

contact areas. In addition the radiographic image of SN-DISK-1 in figure 4.6 reveals similar evidence of low density regions. Figure 4.8 confirms that lower CT numbers correspond in general to regions with high porosity and low density.

X-ray diffractometer scans of polished SN-DISK-A at the boron nitride/silicon nitride contact regions and at other regions showed beta-silicon-nitride to be the only detectable crystalline phase. There was no evidence of boron diffusion into the silicon nitride disks. This demonstrates that the only variation in these disks are density/porosity variations.

It can be concluded that both radiography and tomography detect significant through-the-thickness density/porosity variations in SN-DISK-1 and SN-DISK-2. Superficial near surface density/porosity variations tend not to show up in tomographs and radiographs due to a lack of contrast relative to overall thickness.

Silicon carbide rotor

The CT image of the slice SN-ROTOR-S3 reveals lower values of the CT numbers in the rotor hub region (yellow-red) and higher values of CT numbers (yellow-green) toward the outside edge. This is substantiated by higher porosity/reduced density at point A in figure 4.10 versus lower

porosity/higher density at point F in the optical micrographs. However the green-red striations emerging from the protruding blades are CT artifacts and are not true CT number variations. Figure 4.10 shows one example at point M where the microstructure would be of reduced porosity if the green striation reflects true high density regions. The microstructure at point M has porosity similar to that of H.

The CT image of SC-ROTOR-S1 in figure 4.11 (A) depicts a half moon of higher values of CT numbers (yellow) than in the center region (black). Figure 4.11 (B) shows that slice SC-ROTOR-S2 exhibits reduced density in the center region and higher density near the edge. The radiographic images in figure 4.12, the optical micrographs in figures 4.13 and 4.14, and the subsurface ultrasonic scan in figure 4.15 (B) exhibit similar density variations detected by CT number variations in figure 4.11. Furthermore figure 4.15 (A) features the presence of cluster of voids in a plane right above that of figure 4.15 (B).

Silicon nitride blade

CT images of SN-BLADE-S1 and SN-BLADE-S2 (Fig. 4.16) and related CT number traces (Fig. 4.17) demonstrate limitations of XCT in characterizing relatively small and complex geometrical components. Density variations detected

in these images can not be verified with optical microscopy. Optical microscopy shows that the microstructure is uniform throughout the polished surfaces of the two slices.

Apparent density changes in figures 4.18 and 4.19 are ascribable primarily to variations in thickness instead of actual density or porosity variations. This was due to difficulties in grinding the two slices flat and sufficiently parallel to eliminate the thickness masking effect on imaging true density variations within the slices.

Scanning acoustic microscopy was used to verify general microstructural uniformity as shown in figure 4.20. These ultrasonic subsurface images show that 1) density is uniform throughout the slices, and 2) possibly a higher density skin exists in both slices. The second finding was confirmed by projection radiography and low magnification optics (Fig. 4.21).

Density Versus CT Number for SiC and Si₃N₄ ceramics

The immersion densities of the disks and the cut-out segments are plotted in figure 4.22 versus the corresponding average CT numbers. The coefficient of correlation was 0.98 between bulk density and CT number for the monolithic ceramics examined.

It was demonstrated that XCT can be used to evaluate density variations. By minimizing or accounting for CT

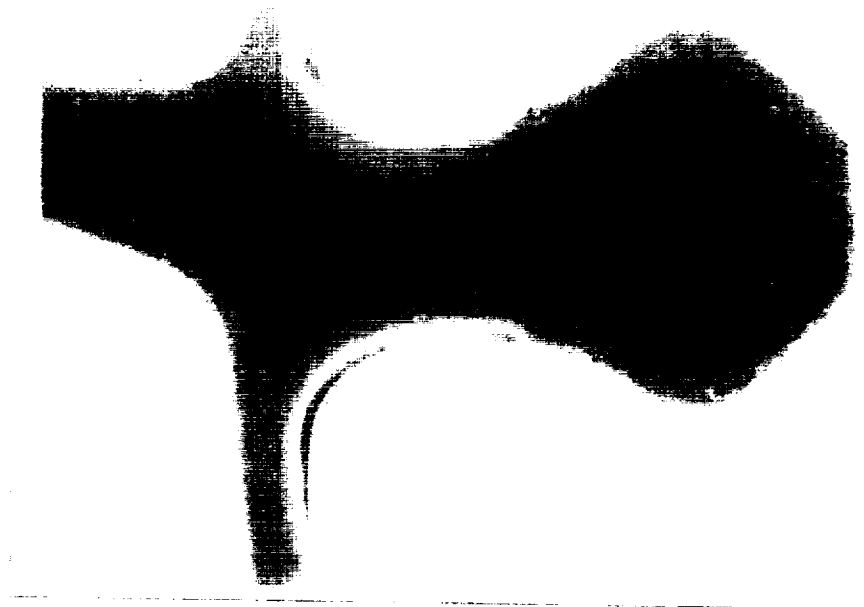


Fig. 4.21.—Optical photograph of the polished surface of SN-BLADE-S2.

ORIGINAL PAGE
COLOR PHOTOGRAPH

PRECEDING PAGE BLANK NOT FILMED

PAGE 140 INTENTIONALLY BLANK

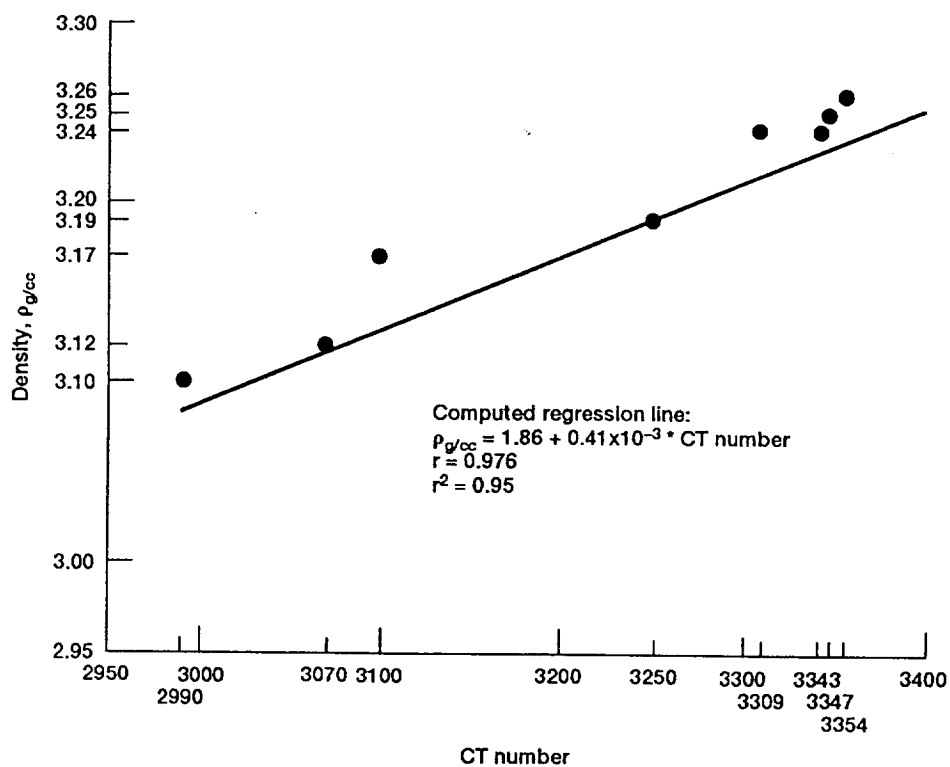


Fig. 4.22.—Density versus CT number for monolithic silicon nitride and silicon carbide ceramics.

artifacts tomographic density information can be used to characterize materials properties and to identify anomalies that can affect the structural integrity of components.

Conclusion

Capabilities and limitations of x-ray computed tomography for characterizing monolithic ceramics have been established. X-ray computed tomography (XCT) is a viable technique for characterizing a relatively medium size component with a relatively simple geometric shape. Tomographic data does provide the information needed to deduce material densities on a volumetric basis. Tomographic findings are corroborated by radiographic, ultrasonic, and light microscopy data.

CHAPTER V.

CHARACTERIZATION OF MMC SUBSCALE ENGINE COMPONENTS USING X-RAY COMPUTED TOMOGRAPHY

Introduction

The manufacturing of high-temperature generic engine components requires concurrent development of new and innovative nondestructive evaluation (NDE) technologies, and parallel upgrading of existing NDE modalities. However, NDE technologies for characterizing newly developing high-temperature composite engine components face many challenging constraints. An NDE technique must be able to characterize components that have 1) thin and thick parts, 2) complex material systems e.g., multiphase composites, 3) complex geometrical shapes, and 4) complex structural integration. Further, NDE must detect and resolve 1) minute processing flaws, 2) different phases or materials that have almost identical properties, 3) fiber architectures, 4) fiber pullouts, 5) fiber breakages, 6) fiber-matrix debonds, 7) delaminations , 8) splittings, and 9) global and local density variations. In addition, nondestructive

materials characterizations should correlate with mechanical/destructive evaluations. Finally, NDE must be standardized for reliable assessments and unambiguous interpretations.

Various NDE techniques have different advantages and limitations. Some are limited to detecting specific types of flaws in certain kinds of materials/components, others are limited to characterizing simple shapes, and most are limited to two-dimensional (2-D) evaluation of 3-D objects. Individual techniques are capable of characterizing only a few features that may detrimentally affect the quality and serviceability of a specific component. Tomographic imaging, using a variety of energy sources, e.g., photons, protons, electrons, and phonons, allows 3-D NDE. However, x-ray tomographic (XCT) imaging is the most widely used technique in industrial NDE (Armistead, 1988). XCT offers distinct advantages over conventional NDE in the realm of 3-Dimensional detection and sizing of internal defects and anomalies. XCT can quantitatively determine, volumetric variations of the CT number in successive transverse cross-sectional images (Berland, 1987; Kak and Slaney, 1988). Comparing these cross-sectional images provides 3-D representation of the internal structure. The CT number represents the x-ray linear attenuation coefficient of a volume element (voxel). The x-ray linear attenuation coefficient is affected by the elemental composition and

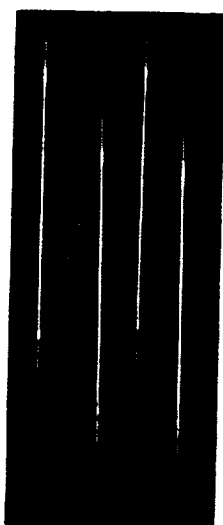
density of the material in a voxel. Comparing these cross-sectional images provides 3-D representation of how internal structures based on their atomic numbers, sizes, and mass densities attenuate x-ray energies.

In this work, capabilities and limitations of XCT for characterizing metal matrix composite (MMC) specimens and subscale engine components are defined. A data base of spatial density information which can be incorporated in geometric modeling of composite constituents and consequent finite element modeling of composite stiffnesses is provided.

Materials and Experimental Systems

A subscale integrally bladed rotor (Fig. 5.1) and light weight engine structures rod (Fig. 5.1) and ring, all made from a pedigreed silicon carbide fiber reinforced beta titanium (Alloy C) composite, are evaluated in this study.⁹ The rod and the ring are HIP consolidated using ribbon-wrapped fiber technology, and the rotor is VHP consolidated using powder coated fiber technology. The rod, the rotor, and the ring are being considered for MMC gas turbine engine applications (Fig. 5.2).

⁹ Pratt and Whitney supplied hardware



Support rods



Rotor subelement

Figure 5.1.—SiC fiber reinforced beta titanium rods and rotor subelement.

ORIGINAL PAGE
COLOR PHOTOGRAPH

PRECEDING PAGE BLANK NOT FILMED

148

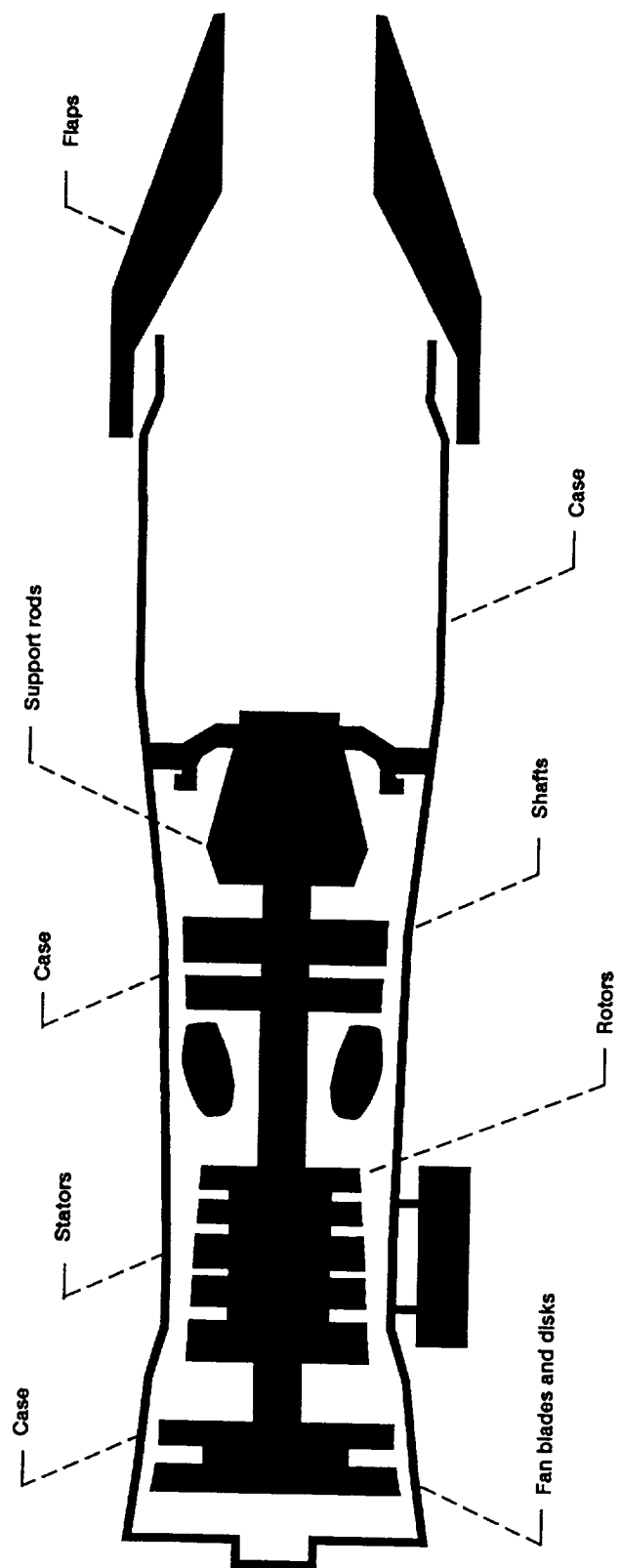


Figure 5.2.—Potential applications for titanium matrix composites in gas turbine engines.

The experimental steps followed are 1) initially evaluate a support rod and subscale components by using XCT; 2) extract and polish transverse cross-sections (2a) from the rod after it was tensile tested, (2b) from the ring after it is burst tested, (2c) and from the rotor; 3) metallographically evaluate all these slices; 4) measure immersion density on each slice; 5) radiographically evaluate each slice; 6) compare radiographic results with metallographic and XCT slice information; and 7) correlate density data with CT number data for each slice.

The previously described XCT system (chapter IV) was used to evaluate these subscale engine components. The CT slice thickness was 2 mm, the image pixel size was 250 μm , the pixel integration time was 55 ms, and the total scan time per slice was 20 to 30 minutes.

A conventional radiography system (400 μm focal spot size) with high energy capability up to 3.2 kW was used to comparatively evaluate the ring, and a microfocus system (10 μm focal spot size) with low energy up to 10 W was also used to comparatively evaluate actual cross-sectional slices.

Results and Discussion

Supporting Rod

XCT evaluation of a supporting rod consisted of scanning it at different locations as shown in figure 5.3. Transverse cross-sectional CT slices (in the horizontal direction) A through F exhibit the CT number variation within these cross-sections as depicted by the change in pseudo-colors or in grayness. XCT images detected unintended excentricity between the core and the case of the composite. Higher CT numbers (blue to dark blue or darker gray) correspond to the case area, whereas lower CT numbers (red to yellow or lighter gray to white) correspond to the core area of the composite slices. Variations in CT numbers along specified directions e.g., bb, dd, and ff are shown in figure 5.3. CT number changed by 9% (from 98% to 92%) from the case to the core of the composite in slice B, and by 6% in slices D (from 89% to 83%) and F (from 92% to 86%). This is expected, because the case is a higher x-ray absorptive titanium base material than the composite core which includes mainly SiC fibers. Furthermore, by comparing slices B, F, and D it is obvious that the CT numbers for the core decreased from B to F to D respectively, indicating nonhomogeneous consolidation in the vertical direction. The cladding in slice B is of higher CT number (98%) than in

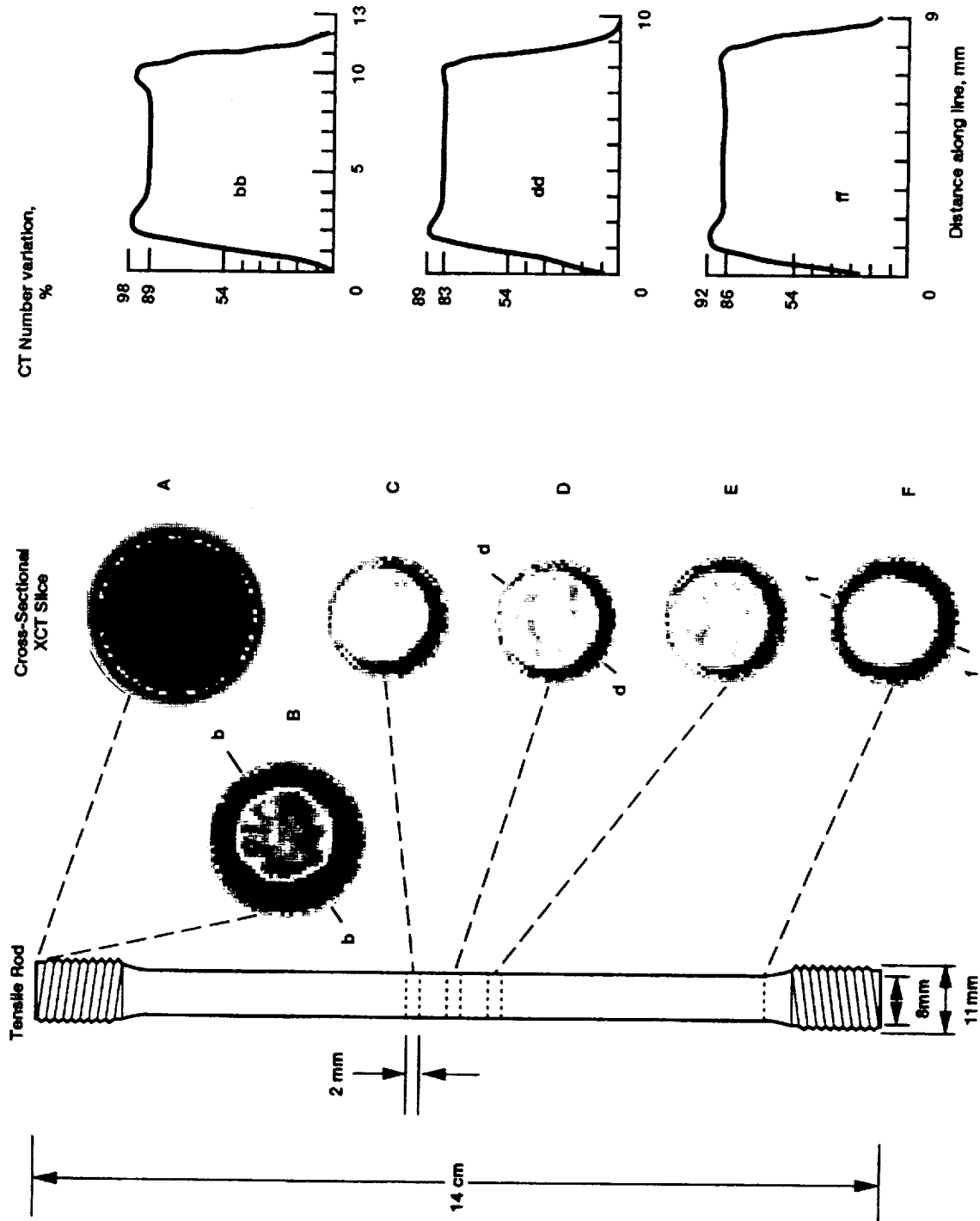


Figure 5.3.—X-Ray computed tomography of MMC tensile rod.

ORIGINAL PAGE
COLOR PHOTOGRAPH

slices D (89%), and F (92%). This is due to the geometry of the rod, the higher CT number sections were machined off in slices away from the threaded region. Slice A shows that no fibers or small number of tip of fibers are present in the last 2 mm slice at the end of the rod.

Data from every voxel enable the computation of the average CT number of any region of interest to include the whole slice area as shown in the third row of figure 5.4. Row four in figure 5.4 shows the immersion density of slices B, D, and F. These densities show a similar trend toward the average CT number for the three slices. However, the average CT number for slice B was not close to its density value. This can be attributed to the x-ray scatter off the edges of the slice making its average CT number smaller than expected because the material, which is not accounted for, is of high CT number, i.e., beta titanium case material.

Figure 5.4 also shows the microfocus radiographs of actual slices taken from the XCT regions B, D, and F. These through-the-thickness x-ray attenuation radiographs accentuate the fiber distribution and average density variations within each cross-section. These are affected by 1) the degree of flatness and parallelism of the slices which affected the through-the-thickness average density variations measurements, and 2) the scatter off the edge of the cladding. This shows that XCT has an advantage over

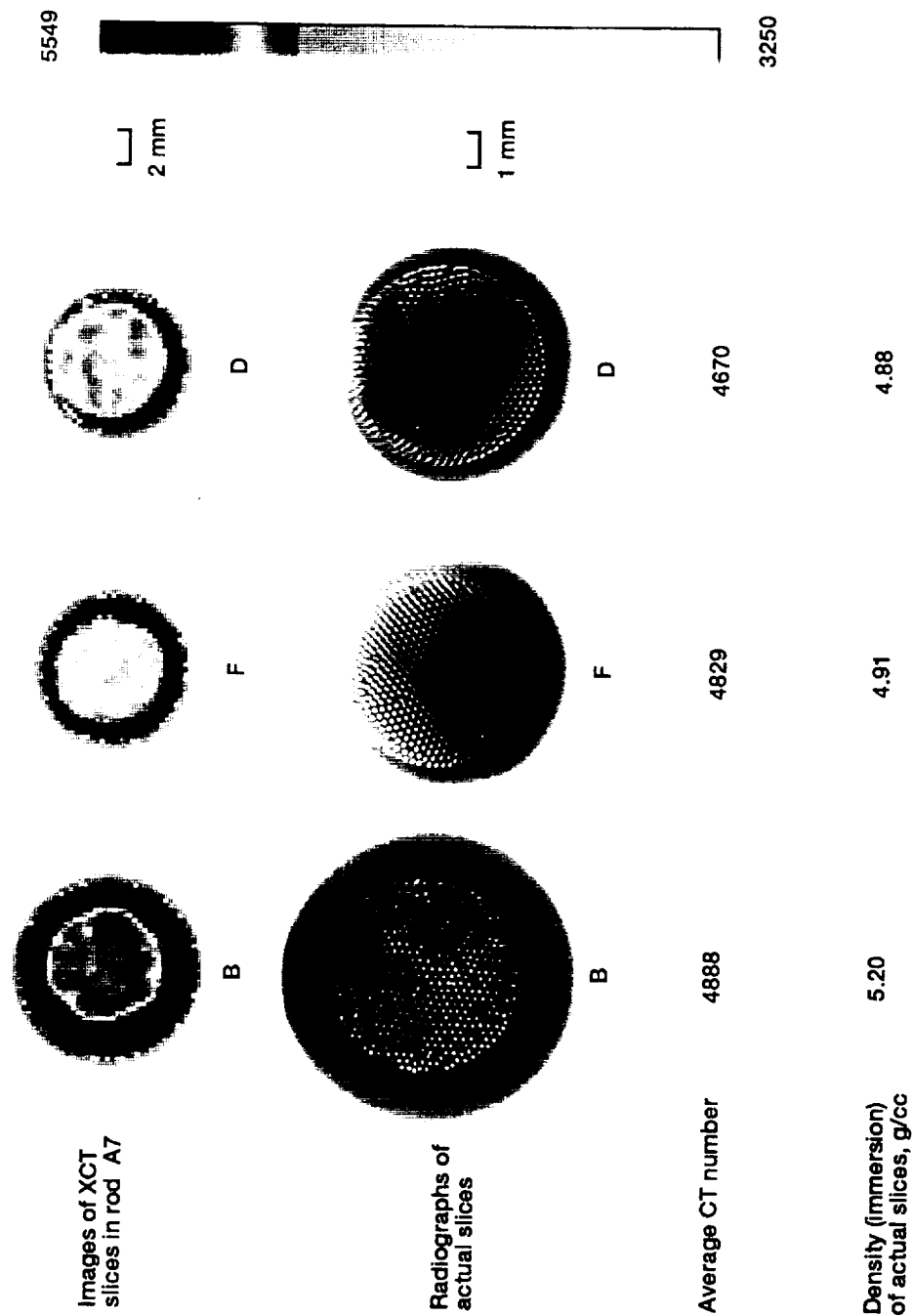


Figure 5.4.—Detailed information on actual slices from the rod.

ORIGINAL PAGE
COLOR PHOTOGRAPH

PRECEDING PAGE BLANK NOT FILMED

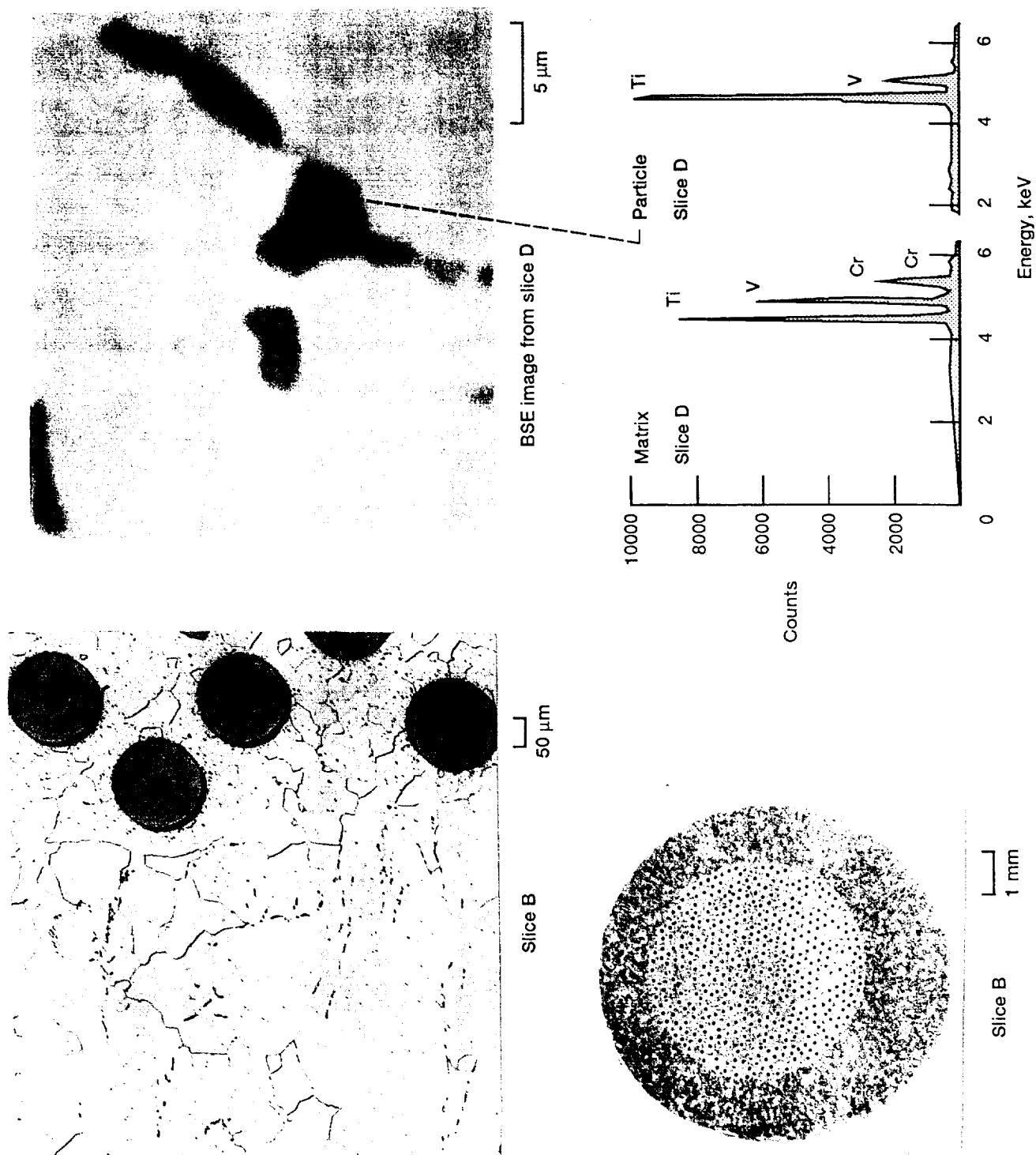
158
PRECEDING PAGE BLANK NOT FILMED

microfocus radiography, i.e., even with a high resolution radiographic system tedious sample preparation is still needed before good representative information can be obtained.

Figure 5.5 shows optical micrographs of slice B as etched. Micrographs of polished and etched slices show that porosity is minute. The presence of titanium rich particles at the grain boundaries is evident, as shown in the back scattered electron image of part of slice D and as demonstrated in comparing the energy spectrums between particle and matrix (Fig. 5.5).

Ring

Figure 5.6 shows a through-the-thickness conventional radiograph of the ring and four XCT slices. Conventional radiography shows a thinner case toward the inside diameter (ID) than the case toward the outside diameter (OD). Conventional radiography also shows the superimposed density variations within the composite core. Similarly, the four XCT slices show a smaller case on the ID side than on the OD side, but also detail the density variations within each slice. XCT slices detect the presence of a protruding cusp in the core located near the top side and toward the ID of the ring. The core of the composite is intended to be rectangular, uniform, and equally distant from all edges.



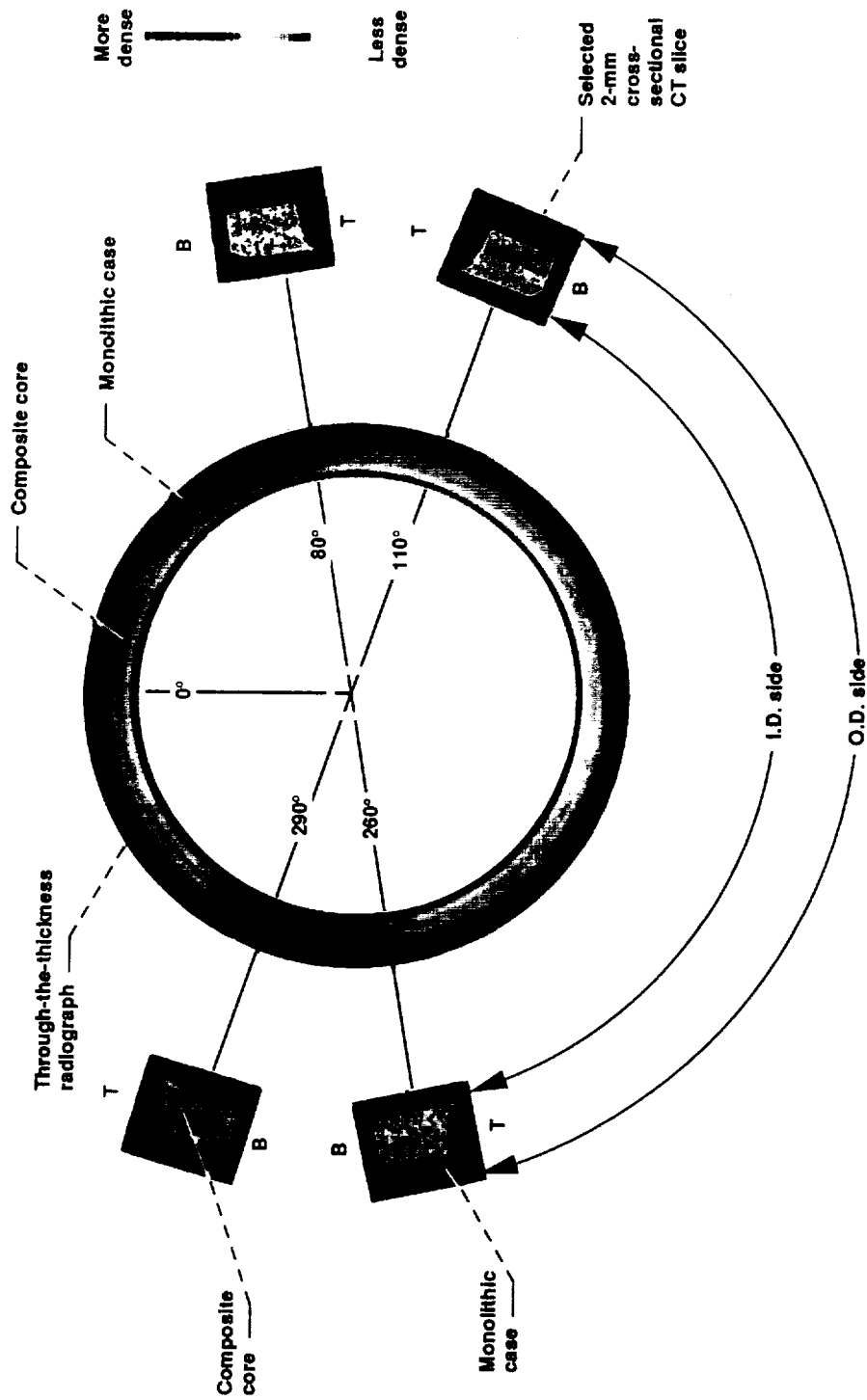


Figure 5.6.—X-radiography and X-computed tomography of MMC ring LES-3.

ORIGINAL PAGE
COLOR PHOTOGRAPH

Figure 5.7 shows a magnified image of CT number variations in the slice taken at 110° and the CT number variations in percent along lines AA and BB. There is a 10% change in the CT number between the case and the core of the ring, and a 3 to 4% change within the composite core.

It should be noted that CT artifacts were not detected in the XCT slices of the rod and the ring, because they had simple circular and rectangular shapes.

SCS6/ALLOY C Rotor

A transverse axial cross-section XCT slice of the subscale integrally bladed rotor is shown in the center of figure 5.8 (Fig. 5.1 is the optical photograph). Also shown are 4 XCT slices taken perpendicular to the circumferential direction roughly midway between two adjacent blades. The streaks in the transverse axial slice demonstrate photon starvation problems, i.e., few x-rays are reaching the detector after being attenuated by the material along the x-ray path lengths. After taking a scan through two diametrically opposite blades, where the x-ray path in the material was on the order of 3.5 inches, it was concluded that this path length is a limiting factor for XCT scanning of this material. The four XCT transverse-to-circumference slices depict a deviation from rectangular shape of the core to an almost a "finger-print" representation of each slice.

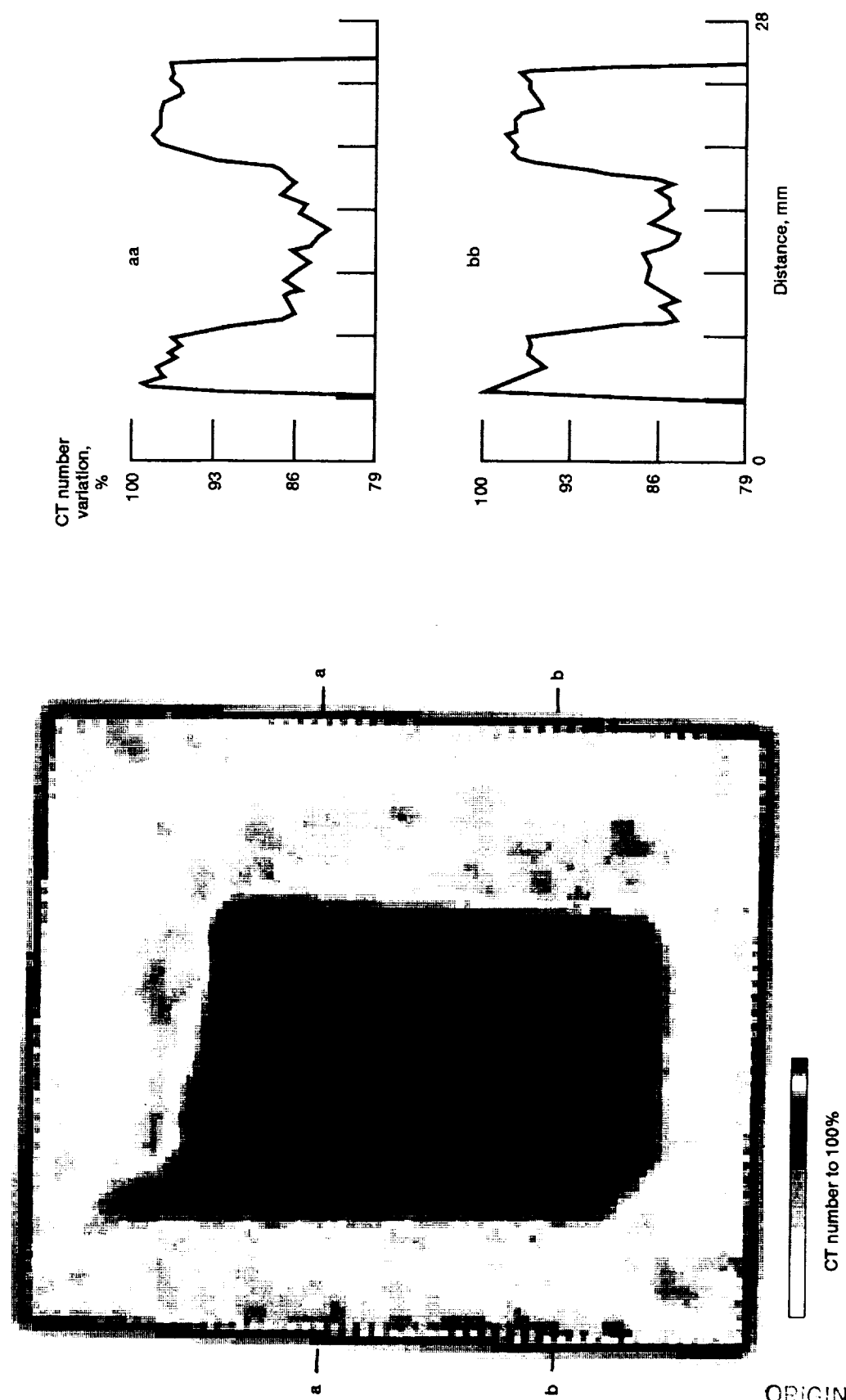


Figure 5.7—CT number variations in the CT slice at 110° from the MMC ring.

PRECEDING PAGE BLANK NOT FILMED

PAGE 146

ORIGINAL PAGE
COLOR PHOTOGRAPH

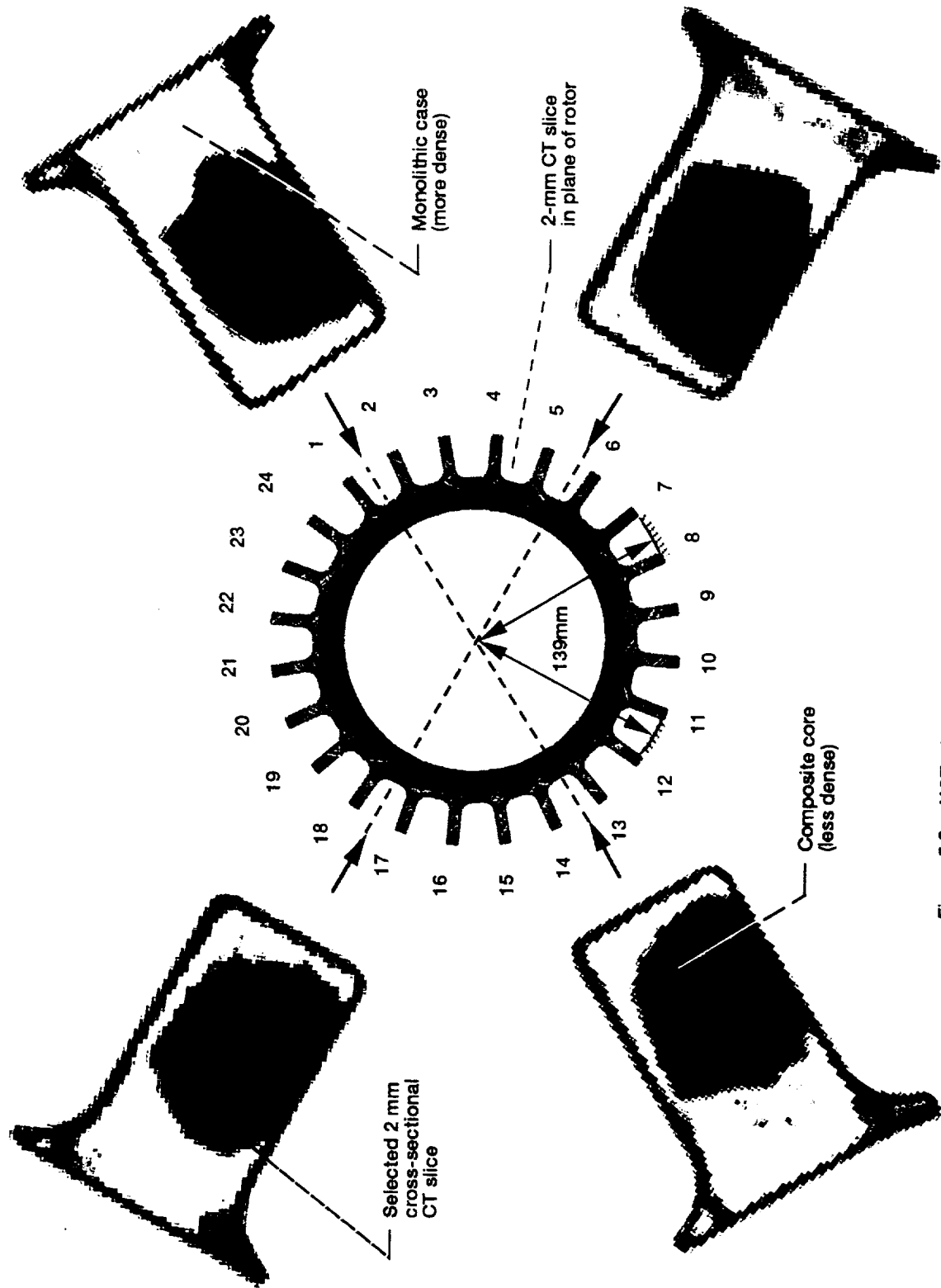


Figure 5.8.—XCT of subscale integrally bladed MMC rotor.

These four slices demonstrate the presence of CT number variations within the core as well as within the cladding regions.

The comparison of XCT data to radiographic data of slice B (Fig. 5.9) shows that the CT number variations within the core are mainly due to the degree of fiber concentration. Greater fiber concentrations are depicted by darker colors. Also shown in figure 5.9 as well as in figure 5.8 is an area of low CT numbers closer to the outside edge and in the two protruding edges of all four XCT slices. However, metallographic examination of all four slices did not show porosity, low density, or particle concentration in these low CT number areas. Figure 5.10 indicates that a minute amount of porosity existed in the composite core near its boundary with the cladding. Furthermore, figure 5.11 displays the presence of titanium rich particles which are more concentrated in the core areas than in the cladding areas. Consequently, the subsequent CT number variations are XCT reconstruction artifacts due to the presence of the protruding small sections in the slices of the rotor combined with the translate-rotate scanning geometry of the scanning system. These XCT artifacts were not detected in the XCT slices of the rod and the ring because of their simple shapes.

Slice B was further sectioned as shown in figure 5.12 and the immersion density was measured on sections I, II,

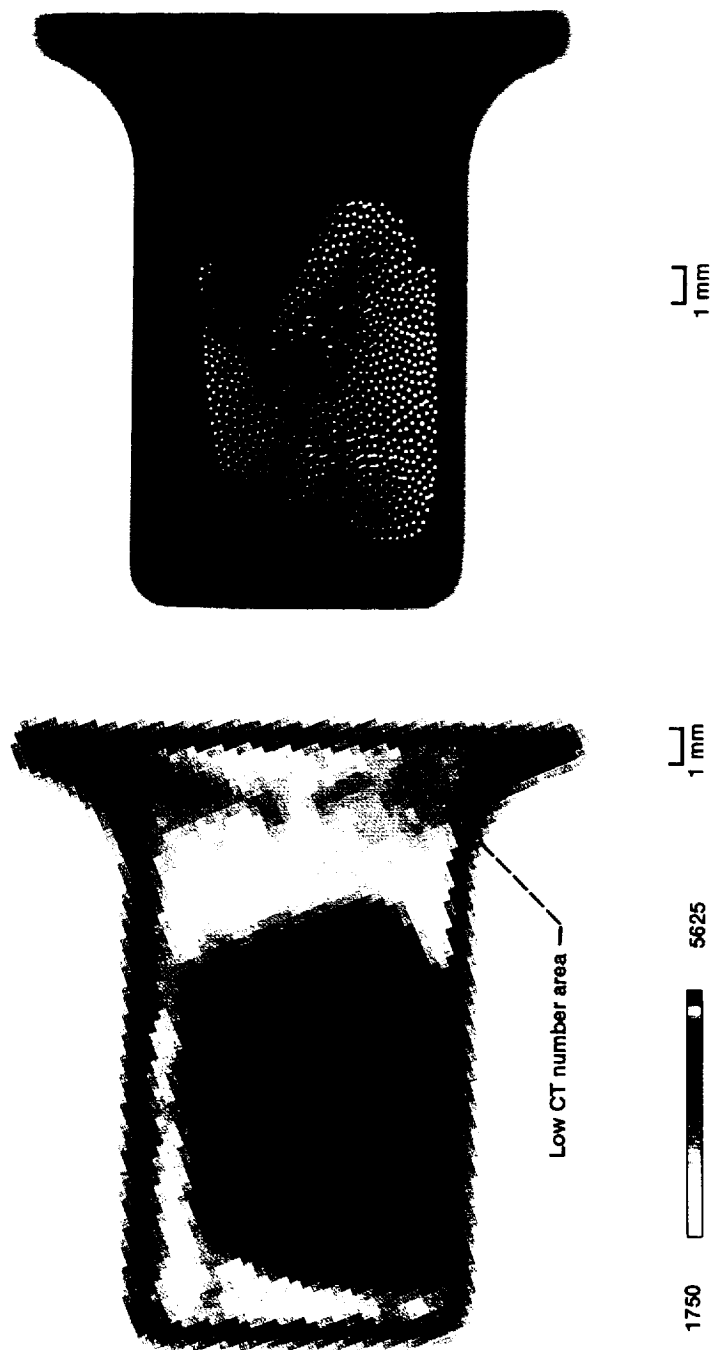


Figure 5.9.—XCT images highlight degree of fiber concentrations.

ORIGINAL PAGE
COLOR PHOTOGRAPH

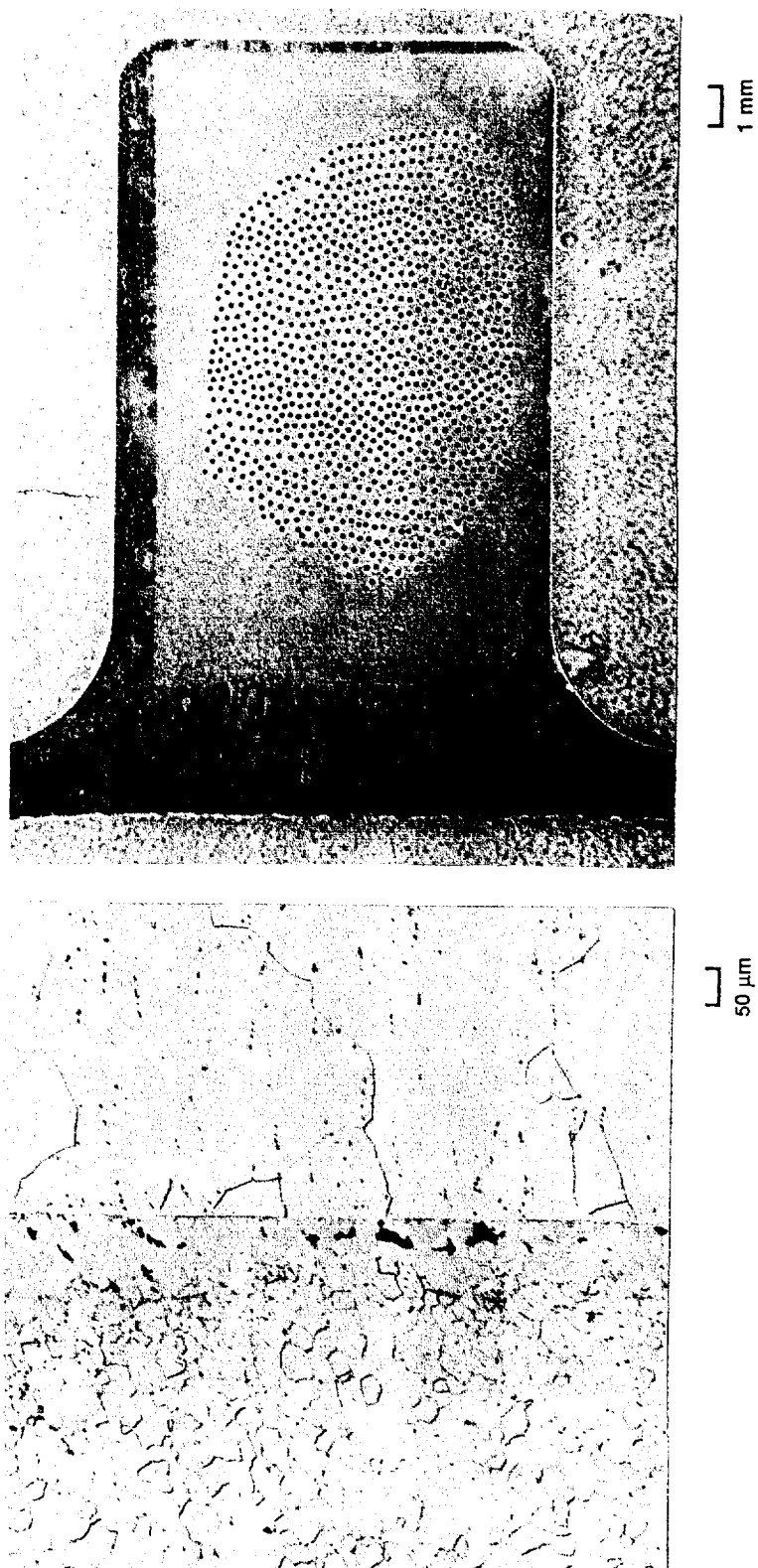


Figure 5.10.—Optical micrographs of slice D from MMC rotor.

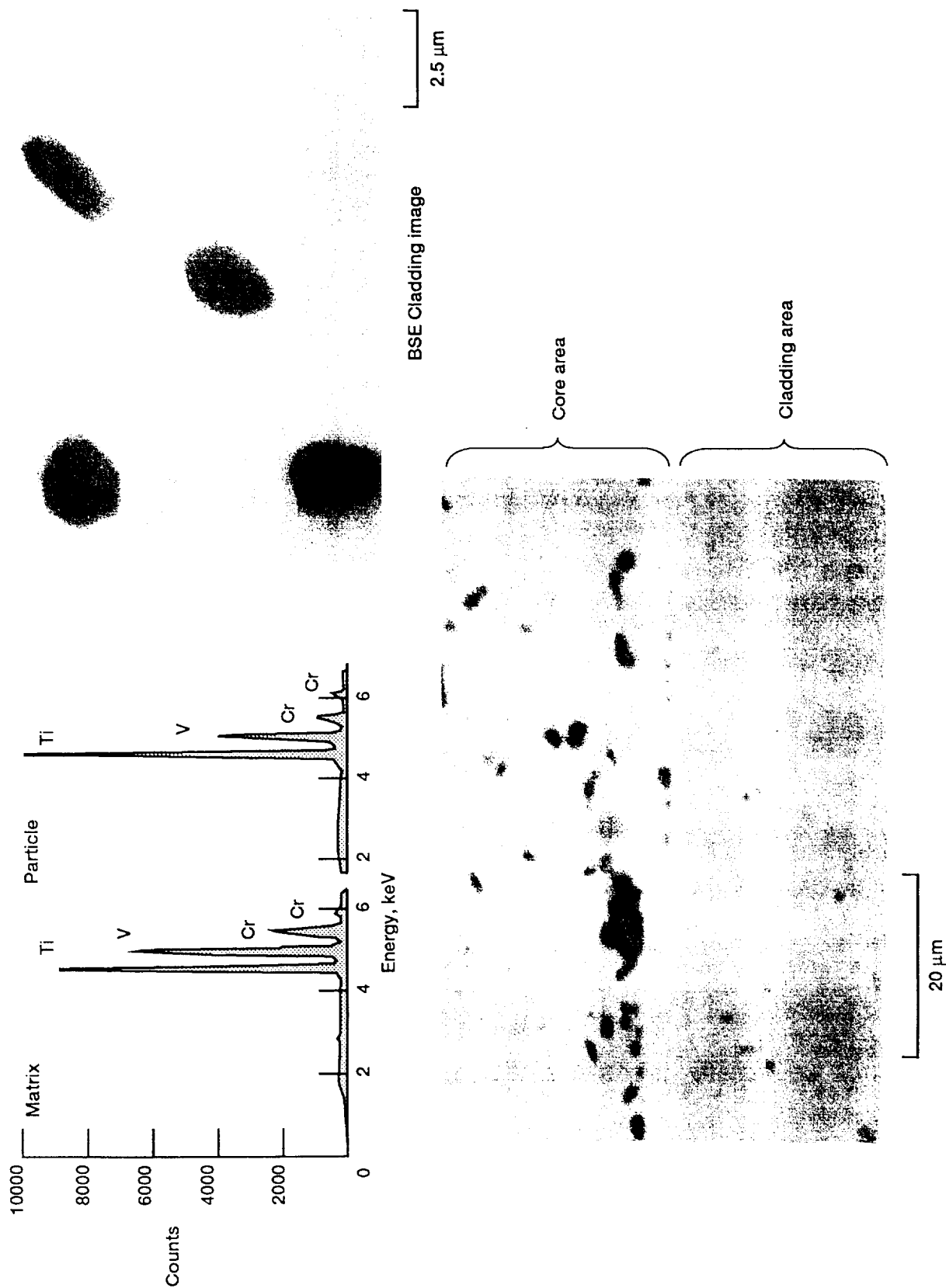


Figure 5.11.—BSE images and EDAX from slice C and corresponding EDAX from MMC rotor.

| | CT number | Density, g/cc (Immersion) |
|-------------|-------------------|------------------------------|
| Slice B | ^a 5009 | 5.10 |
| Section I | ^b 4718 | 4.83 |
| Section II | ^b 5263 | 5.29 |
| Section III | ^c 5222 | 5.40 |

- ^aGood average density measurement
^bGood density measurement away from artifact area.
^cCT artifacts due to:
- Object geometry
 - Reconstruction algorithms

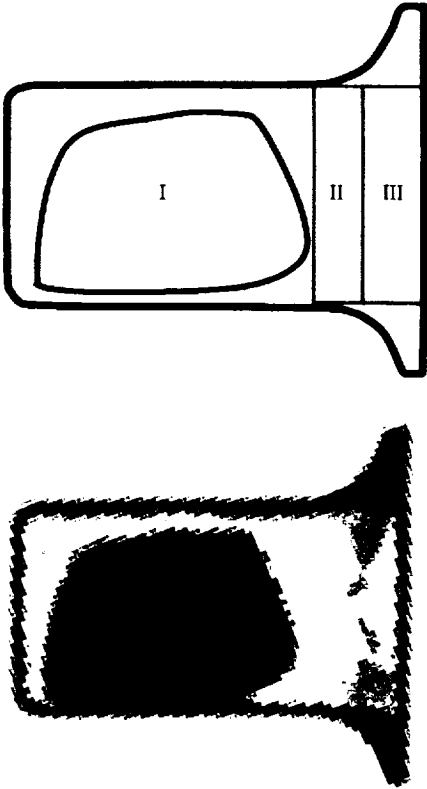


Figure 5.12.—CT numbers and immersion density measurements of different sections in slice B from MMC rotor.

and III. Density measurements correlated with optical characterization, i.e., region I is less dense than region II which in turn is less dense than region III. The average CT number for the whole slice and for sections I and II agreed very well with the corresponding measured densities, however the CT number for section III predicted poorly the density of that section. This proves that XCT can be used to estimate density for the whole slice and for sections free of CT artifacts.

Density versus CT number for SCS6/Alloy-C composite

The immersion densities of a few slices from the rod and of a few slices and sections from the rotor are plotted in figure 5.13 versus the corresponding computed average CT numbers. Even though the data included some XCT artifacts and in certain cases was partially limited due to x-ray scatter off the edges, this plot shows a correlation between bulk density and CT number for a composite system.

General Discussion

XCT information was provided to the manufacturer and this helped identify fabrication and processing problems for different material processes, and among different components which were fabricated with similar processes. The CT number

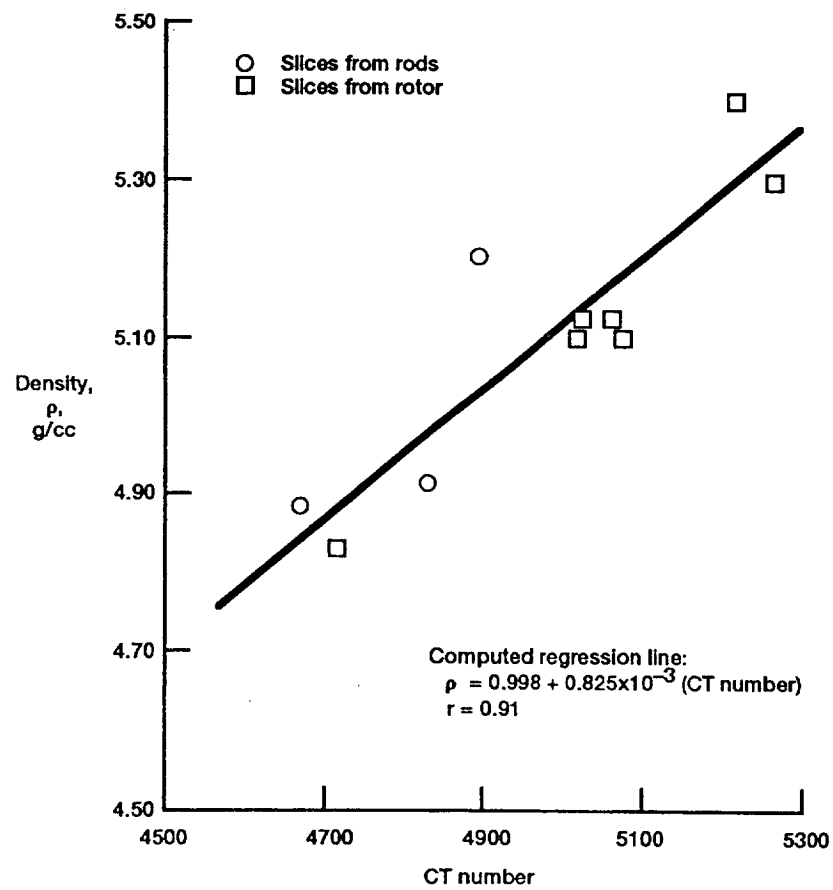


Figure 5.13.—Density as a function of CT number for SC-6/alloy C.

variations which were detected within the core region of the rod (less than 1 percent) were much less than those within the core region of the ring (3 to 4 percent). This indicates better consolidation in the cylindrical rod than in the annular ring. In order to avoid machining through fibers, as in the case of the rod, the manufacturer now uses XCT images to guide machining of components to final dimensions.

XCT density information is being recognized as a means for guiding structural design engineers. Distortions in composite constituents, which may cause nonuniform material responses at high temperatures and under different loading conditions, is detected by XCT. Consequently, design and test engineers can concurrently decide whether to continue testing defective component or section them for detailed evaluation in order to further identify sources of manufacturing problems. NDE coupled with destructive verifications will certainly help accelerate the improvement of composite components.

Three-dimensional density information of composite components, can guide geometric modeling of composite constituents, and also it can guide composite stiffnesses modeling where CT artifacts are avoided or minimized. Engineering tomography, which incorporates XCT density information in finite element modeling, can significantly

help in predicting life and serviceability of composite components.

Conclusion

Capabilities and limitations of x-ray computed tomography for characterizing metal matrix composite subscale engine components were defined. Examples of spatial density information, which can be incorporated in finite element modeling of composite spatial stiffnesses and in geometric modeling of composite constituents were provided. It can be inferred that X-ray computed tomography is a viable technique for accelerating the development of composite components. X-ray computed tomographic imaging can identify problems with manufacturing processes, guide machining of components to final dimensions, and lead structural and design engineers to realistic component-life-prediction models.

CHAPTER VI

IN-SITU X-RAY MONITORING

Introduction

Ceramic matrix composite (CMC) systems are being developed for heat engine applications (Mah et al., 1987; Heraud et al., 1988; Bhatt, 1988). The ultimate goal of the current research is an understanding of composite behavior in order to optimize the composite properties for different hot section applications. CMCs are being developed because they provide enhanced material toughness while maintaining the useful properties of monolithic ceramics. The fiber-matrix interface in CMCs plays an important role in determining toughness-related properties (Kerans et al., 1989; Evans and Marshall, 1989), but there is very little quantitative data on interface properties (Kerans et al., 1989). Further, composite failure processes are not well understood and there is a lack of verified and validated failure models.

In order to apply CMCs in critical high temperature structures, the failure processes and damage tolerances must be understood and the failure analyses and mechanics models must be improved. Methodologies such as in-situ x-ray radiography and acoustic emission monitoring clarify failure sequences and damage accumulation processes in composite specimens under loading (Baaklini and Bhatt, 1990; Chulya et al., 1990). The information gathered from in-situ monitoring can help in the development and validation of analytical models. Damage and failure mechanisms, e.g., transverse matrix cracking, fiber-matrix debonding, fiber breaking, fiber pullout, and delamination can be better understood if imaged and identified as they occur. Noninvasive in-situ examination can help elucidate the sequence in which these phenomena occur and, consequently, aid in the identification of controlling factors, i.e., whether they are matrix dominated properties, fiber dominated properties or a combination of both.

The objectives of this study are to demonstrate the capabilities of in-situ x-ray radiography for monitoring damage accumulation and failure processes in unidirectionally reinforced SiC/RBSN system under tensile loading. It will be seen that the methodology can be used to determine the interfacial shear strength between the SiC fiber and the RBSN matrix. The benefits of this research are: (1) interpretation of mechanical

test results, (2) validation of analytical models, (3) verification of experimental procedures, and (4) optimization of the fabrication process.

Experimental

In-situ x-ray and materials testing system

An in-situ x-ray and materials testing system (IXMTS) facility was built in order to conduct in-situ x-ray monitoring of materials under tensile loading. Figure 6.1 shows a schematic of the experimental apparatus. Figures 6.2 and 6.3 show the IXMTS and details of the specimen testing/evaluation region. The IXMTS combined a 3.2 kW x-ray source, and an electro-mechanical materials testing system.

The x-ray source/generator were capable of reaching a maximum voltage of 160 kV and a maximum current of 45 mA. The x-ray tube had a 400 μm and a 3 mm focal spot size. Film radiography was chosen as the detection medium because of its high resolution and registration capabilities. The materials testing system¹⁰ consisted of a 250 kN load frame, a 100 kN electro-actuator, a 50 kN load cell, and a digital control system.

¹⁰ Instron Materials Testing System, Canton, MA

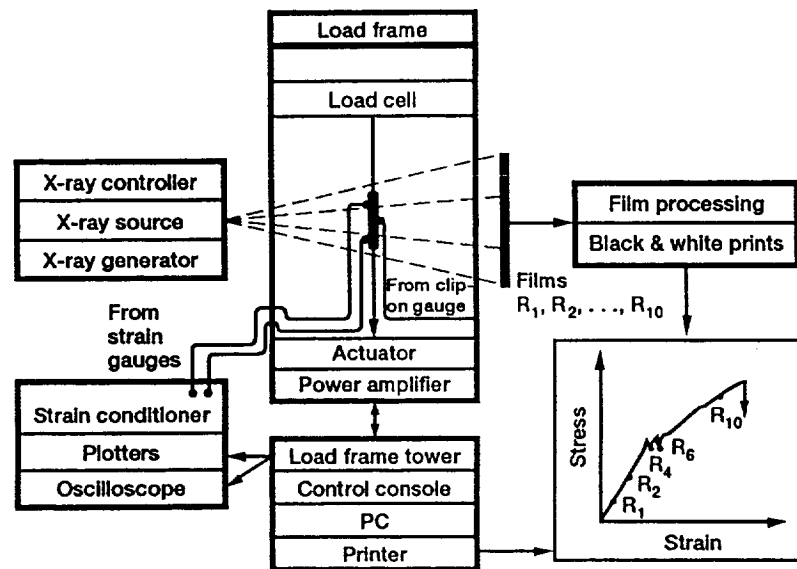


Figure 6.1.—Schematic diagram of the In-situ x-ray and materials testing system.

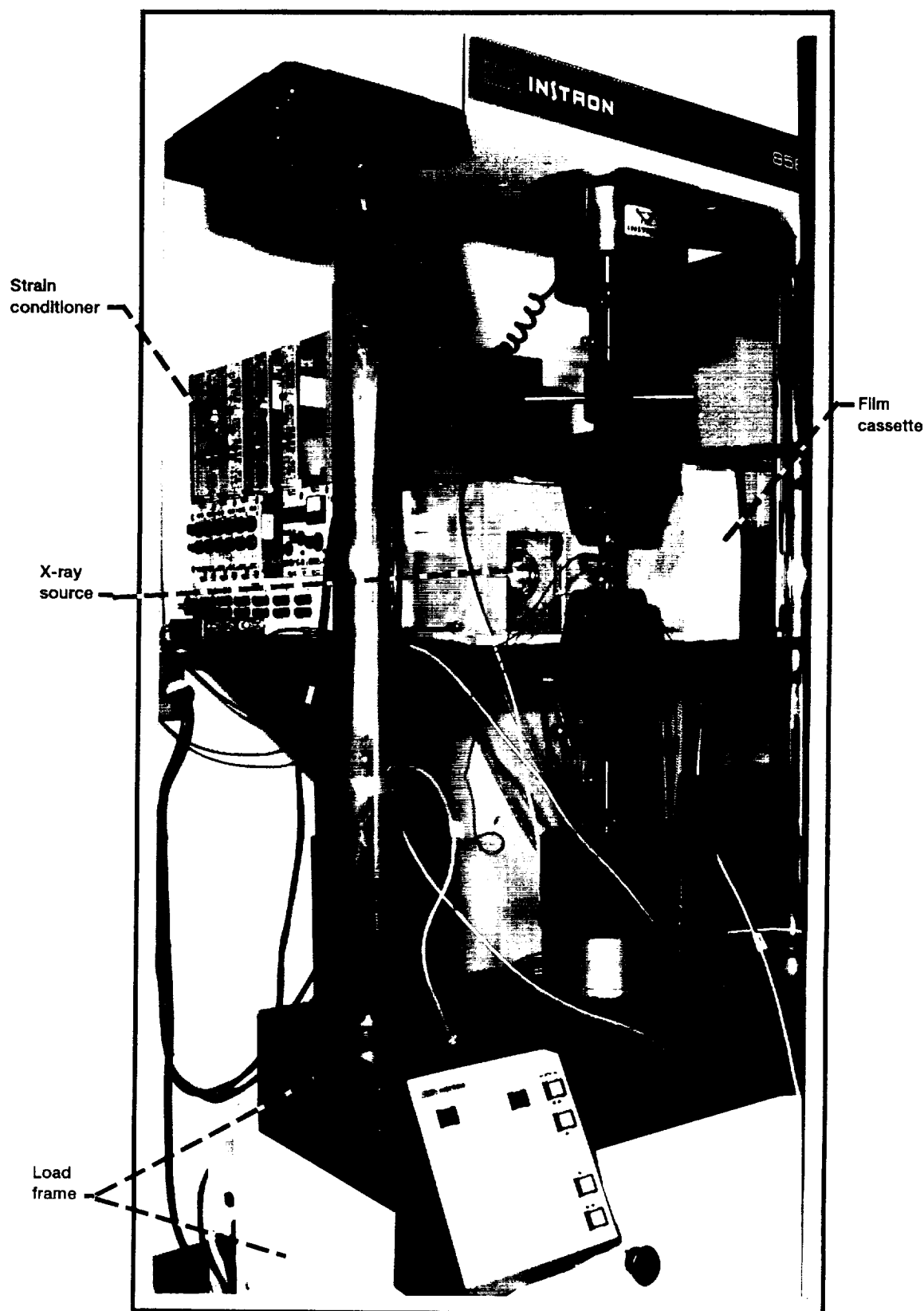


Figure 6.2.—In-Situ x-ray and materials testing system.

~~PRECEDING PAGE BLANK NOT FILMED~~

ORIGINAL PAGE
COLOR PHOTOGRAPH

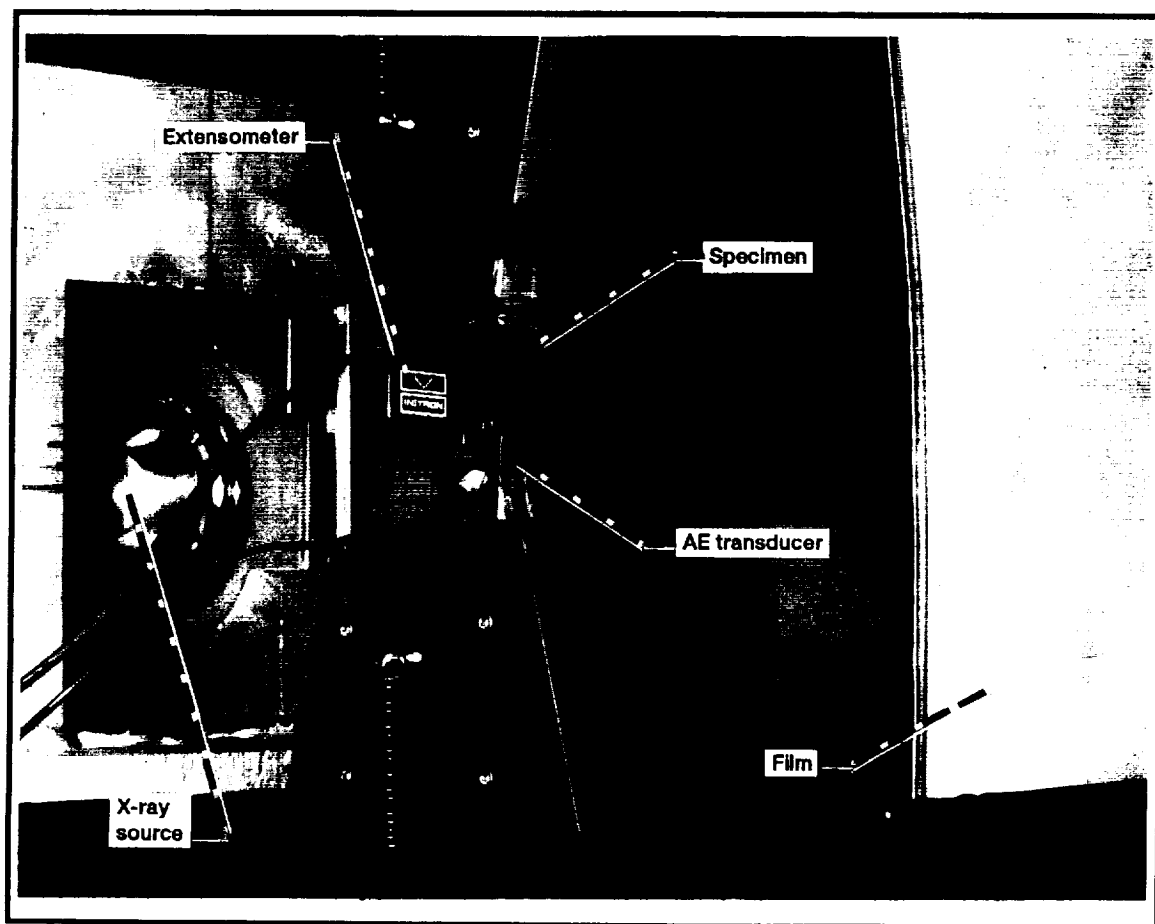


Figure 6.3.—Detail of In-situ x-ray materials testing system.

ORIGINAL PAGE
COLOR PHOTOGRAPH

ORIGINAL PAGE
COLOR PHOTOGRAPH

PRECEDING PAGE BLANK NOT FILMED

188

All the work described here was done at room-temperature. The tensile testing is done in a load control mode for some specimens and in displacement control mode for others. Loading and displacement rates are 45 N/min and 25 $\mu\text{m}/\text{min}$, respectively. These relatively slow rates are used in order to allow ample time for in-situ film radiographic image registration without holding the load or displacement. The load increment is ≤ 111 N during the radiographic exposure (25 to 35 seconds), except at failure. As the tensile specimen is loaded, the axial strains are monitored by two adhesively bonded strain gauges and a clip-on extensometer. Two x-ray films (to separate film development artifacts from defects in materials) are exposed at different stress-strain levels during the test.

The strain gauges are bonded to the faces of the specimen and the extensometer is clipped to the edge while leaving the 2.54 cm gauge length accessible to in-situ radiography. Immediately after each test, the specimen is evaluated with microfocus radiography and optical metallography. The radiographic images are used to interpret the results in conjunction with the stress-strain data.

Radiographic evaluation

Two different x-ray systems are used: (1) a conventional system with a 400 μm focal spot size and (2) a microfocus system with a 10 μm focal spot size. Conventional radiographs are made in the direct contact mode (image is 100% of object size) while microfocus radiographs are made in a projection mode with a resultant magnified radiographic image. In addition to in situ during tensile testing conventional radiography was used to evaluate silicon powder cloths and composite panels before and after machining. High resolution microfocus radiography (Baaklini and Roth, 1986) is used to evaluate the tensile specimens before loading and after failure.

Specimens

The SiC/RBSN composite $[0]_1$, $[0]_3$, $[0]_5$, and $[0]_8$ ply panels are produced by ceramic powder fabrication methods (Bhatt and Phillips, 1988) using 142 μm diameter SiC fibers, designated with a double carbon coated layer known as SCS-6 fibers¹¹. Bhatt (1987) has described the method of preparing fiber-reinforced ceramic materials in detail. Fabrication procedures were summarized in chapter II. The radiographic evaluation of machined panels guided the

¹¹ Textron Specialty Materials Division, Lowell, MA

cutting of tensile specimens. The selection of cuts was predicted on different density features exhibited by the composite panels to obtain: (1) specimens with sizeable volumetric high density impurity located in the gauge length region, (2) specimens with many small high density impurities in the gauge length region, and (3) specimens with low density variations were chosen. The specimen dimensions were 125 by 12.7 by 1 to 2.0 mm. Two axial wire-wound strain gauges were adhesively bonded to the front and back faces of each tensile specimen which had glass fiber-reinforced epoxy tabs for gripping.

Results

Radiographic characterization prior to testing

Figure 6.4 shows a radiographic image of a representative $[0]_3$ SiC/RBSN panel before and after machining the graphite layer. The graphite layer formed during the high temperature vacuum hot pressing composite fabrication. It is obvious from the radiographic print before machining that the graphite layer masks any density variation information from the SiC/RBSN panel, i.e., the density variation detected was mainly due to the variation in the thickness and density of the graphite layer itself.

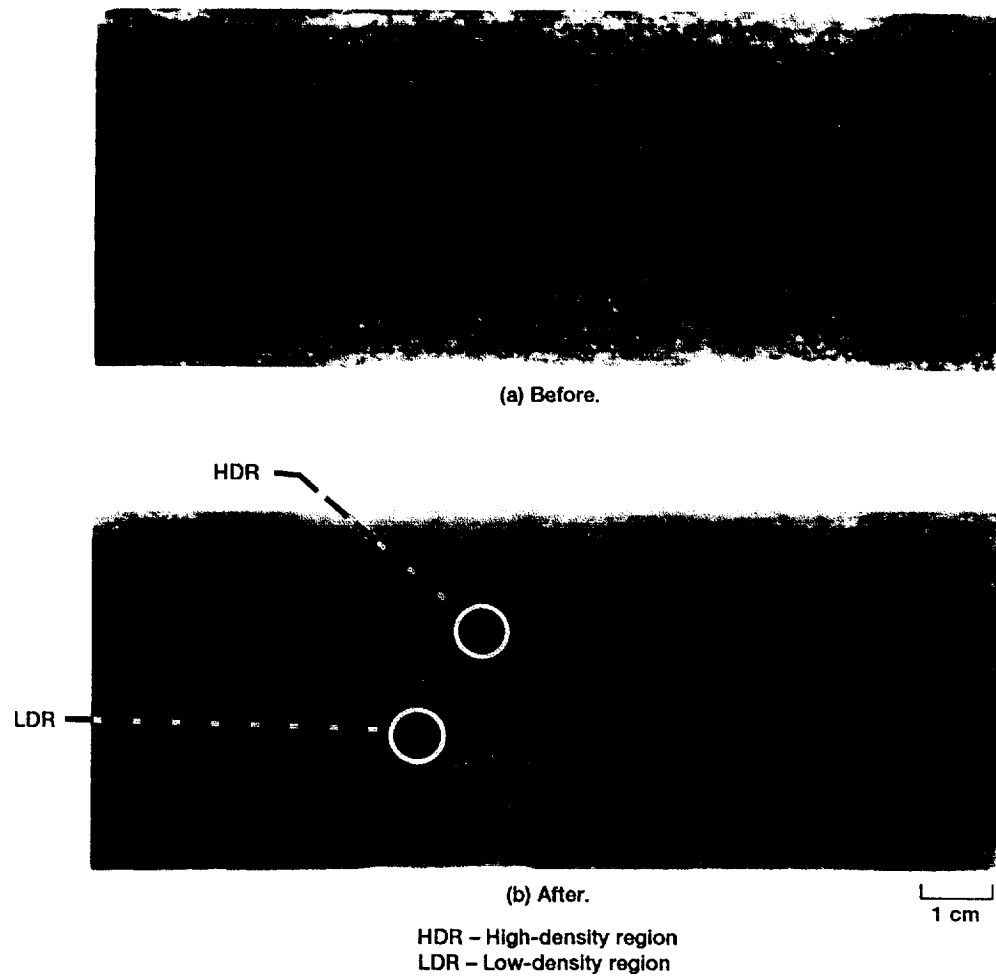


Figure 6.4.—Conventional radiographs of $[0]_3$ panel before and after machining.

Machining the graphite layer, enabled better radiographic characterization of the composite panels. After machining the fiber architecture was detected. The orientation of the fibers is evident in figure 6.4. High density impurities, i.e., the dark isolated features (black dots) which are shown in figure 6.4(b), were identified as iron rich inclusions. Light to white spots in figure 6.4(b), were due to localized low density or surface chipping.

Mechanical properties

The room temperature tensile stress-strain behaviors for $[0]_1$, $[0]_3$, $[0]_5$, and $[0]_8$ SiC/RBSN specimens are shown in figure 6.5. Corresponding tensile properties are listed in Table II. The rule-of-mixtures composite modulus (Agarwall and Broutman, 1979), $E_{(rom)c}$, is,

$$E_{(rom)c} = E_m V_m + E_f V_f \quad (6.1)$$

where E_m and E_f are the matrix and fiber moduli, respectively, and V_m and V_f are the matrix and fiber volume fractions, respectively. $E_{(rom)c}$ values appear in Table II. The E_m and E_f values used herein are 110 GPa and 390 GPa respectively (Bhatt and Phillips, 1988).

The stress-strain results for the $[0]_1$ and the $[0]_3$ specimens show a linear behavior until final fracture. At

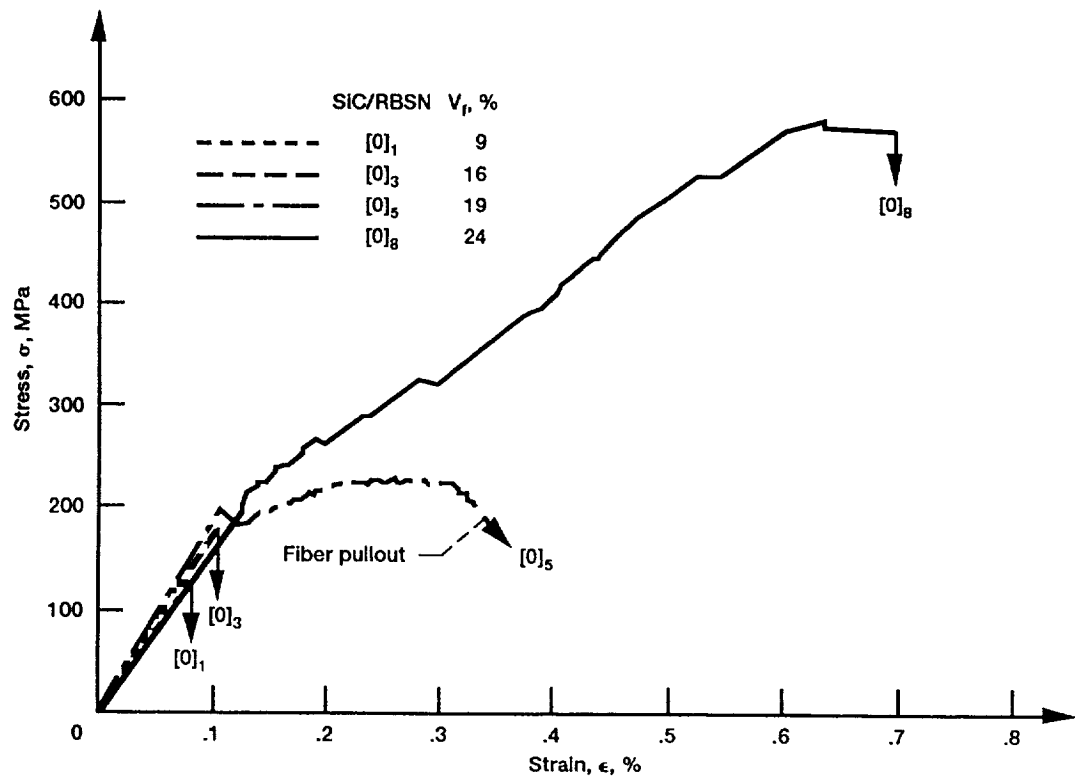


Figure 6.5.—Room temperature stress-strain behavior for unidirectionally reinforced SIC/RBSN composite specimens.

TABLE II.—ROOM TEMPEARATURE TENSILE PROPERTY DATA FOR Sic/RBSN

COMPOSITE SPECIMENS

| Sic/RBSN | V_f percent | Number of specimens | E_c^a GPa experimental | E_c^a GPa rules of mixture | TC MPa ultimate | Proportional limit | |
|----------------------|------------------|---------------------------|--------------------------------|---------------------------------------|-----------------------|-----------------------|-------------------------|
| | | | | | | σ , MPa | ϵ , percent |
| $[0]_1$ | 9 | 5 | 160 | 135 | 129 | 129 | 0.08 |
| $[0]_3$ | 16 | 1 | 178 | 155 | 178 | 178 | 0.10 |
| $[0]_8$ | 19 | 3 | 180 | 163 | 226 | 197 | 0.11 |
| $[0]_8$ | 24 | 1 | 175 | 177 | 576 | 195 | 0.12 |
| ^b $[0]_8$ | 23 | 1 | 108 | 175 | 120 | 43 | 0.04 |

^a $E_c = E_m V_m + E_f V_f$ where $E_m = 110$ GPa and $E_f = 390$ GPa.

^bOverprocessed (1350 °C in N_2 + 4 percent H_2 for 80 hr).

ultimate stress the specimens tested in the load control mode failed catastrophically. Specimens tested in the displacement control mode exhibited a load drop region before final failure. In the latter case, radiography shows that fiber pullout was the dominant failure mechanism.

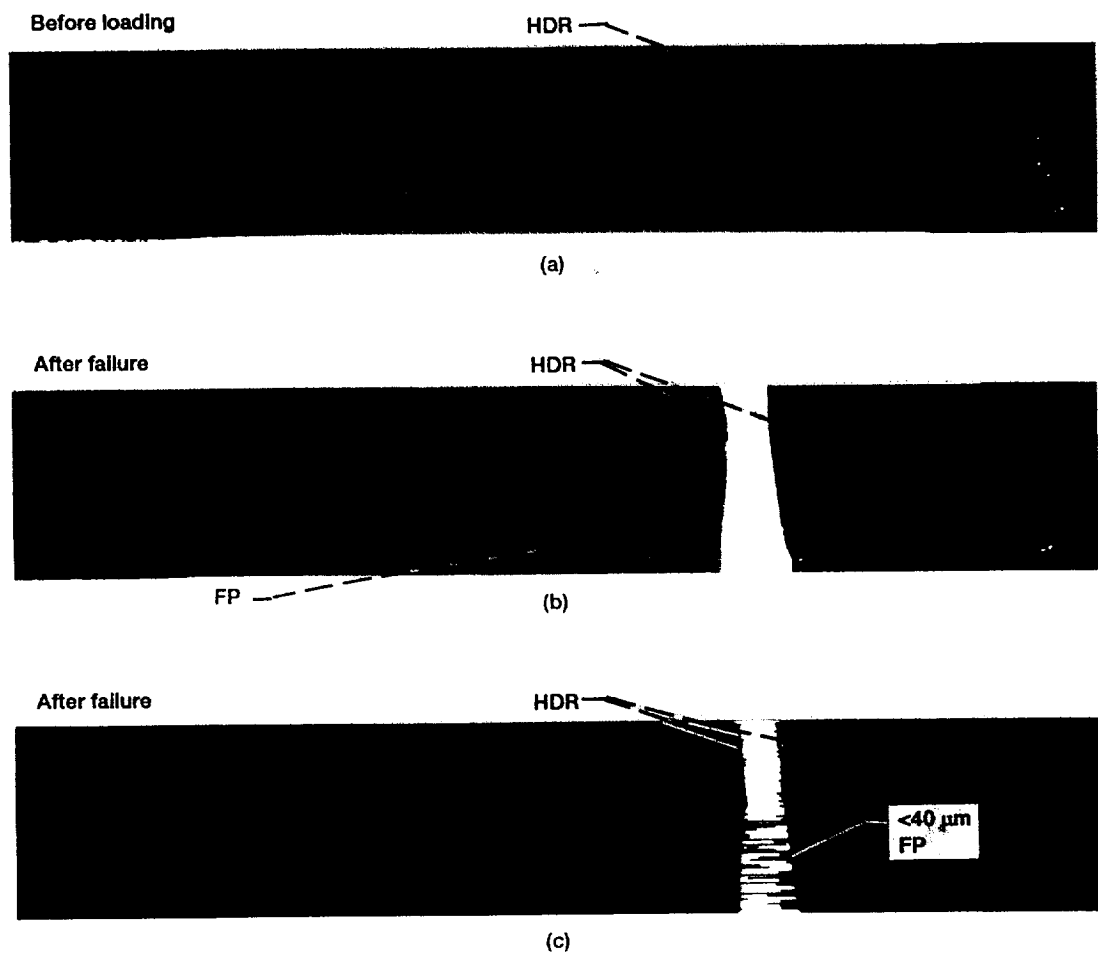
The stress-strain results for the $[0]_5$ specimens show three distinct regions. In the initial region, the stress varies linearly with the strain up to an average stress level of 197 MPa when the load momentarily drops. In the second region the stress-strain curve becomes nonlinear and displays serrations due to the load dropping and recovering without exceeding an average engineering stress of 226 MPa. The third region shows fiber pullouts during which the load dropped slightly but not as catastrophically as upon final failure.

The stress-strain results for the $[0]_8$ specimen show three distinct regions. In the initial region, the stress varies linearly with the strain up to a stress level of approximately 195 MPa when matrix cracking become evident. In the second region the behavior is nonlinear, the load is either holding or dropping then recovering and increasing as the strain is increased. In the third region, the stress varies linearly with the strain in segments where the modulus is either the same or decreasing until maximum tensile stress is reached, shortly after the specimen shows minor load carrying capacity before final fracture.

In-situ radiographic imaging

Figure 6.6 shows microfocus radiographs of the $[0]_1$ specimen. These radiographs were made before loading and after failure. The before-loading image shows a 0.5 by 1.0 mm high density subsurface impurity. This high density region consisted of cluster of 50 μm diameter inclusions. The after-failure image shows that the fracture initiated at the site of the impurity and propagated across the width of the sample. This was inferred from the location and number of the fiber pullouts. Closer examination of the radiograph film showed the presence of multiple breaks per fiber. Figure 6.6(c) shows that microfocus radiography detected 40 μm fiber pullout length.

Figure 6.7(a) and (b) show microfocus radiographs of two different $[0]_1$ specimens after failure. These radiographs show random fiber pullouts and multiple matrix cracks. These cracks did not propagate through the thickness of the specimens because of fiber-matrix debonding at the fiber-matrix interface. Similarly, figure 6.7(c) for a $[0]_3$ specimen shows (1) through-the-width but not through-the-thickness cracks, (2) fibers pullout, and (3) fiber-matrix debonding. The white region near the right of figure 6.7(C) indicates extensive fiber-matrix debonding which also occurred outside the 2.54 cm gauge length (the area between the two strain gauges).



- FP - fiber pullout
- HDR - high-density region

Figure 6.6—Microfocus radiographs of a [0]₁ SiC/RBSN specimen.

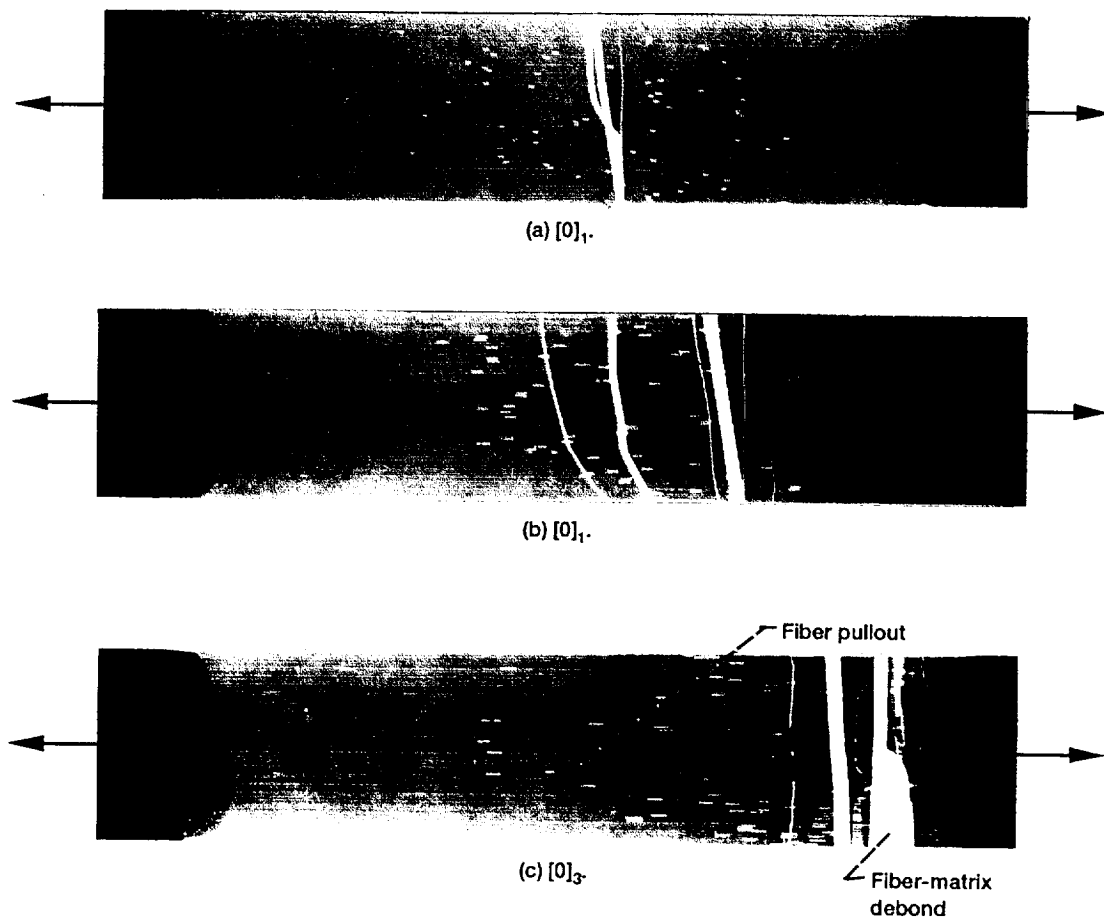


Figure 6.7.—Microfocus radiographs of SiC/RBSN specimens after failure.

Figure 6.8 shows magnified microfocus radiographs of the major cracking zone in the 1-ply specimen after failure. Figure 6.9 shows the right and left edges of the same specimen where fiber matrix debond is evident. In addition the optical micrograph in figure 6.10 clearly shows the pullout identified by radiography. Similarly, figure 6.11 shows magnified radiographs of a 5-ply specimen with random fiber pullout in and near the major cracking region. Figures 6.12 and 6.13 are photographs of the same specimen showing evidence of fiber matrix debonding and random matrix cracking where most cracks are not through-the-thickness and across-the-width type. In addition, by comparing figure 6.11 to figure 6.13 it is evident that locations of the fiber pullouts are optically nontransparent.

Figure 6.14 shows three radiographs R6, R8, and R10 selected from a series of 10 in-situ radiographs taken throughout the tensile loading history of a $[0]_5$ specimen. The stress-strain behavior is also shown. In figure 6.14, radiographs R3, R4, and R5 do not show the presence of matrix cracking. However, R6 shows one major thru-width crack and R8 shows multiple cracks. R10, taken after failure shows (1) fiber pullouts, (2) closure of cracks imaged earlier under load, and (3) major cracks with corresponding fiber-matrix debonds region at failure. Radiographs R7 and R9 show similar information.

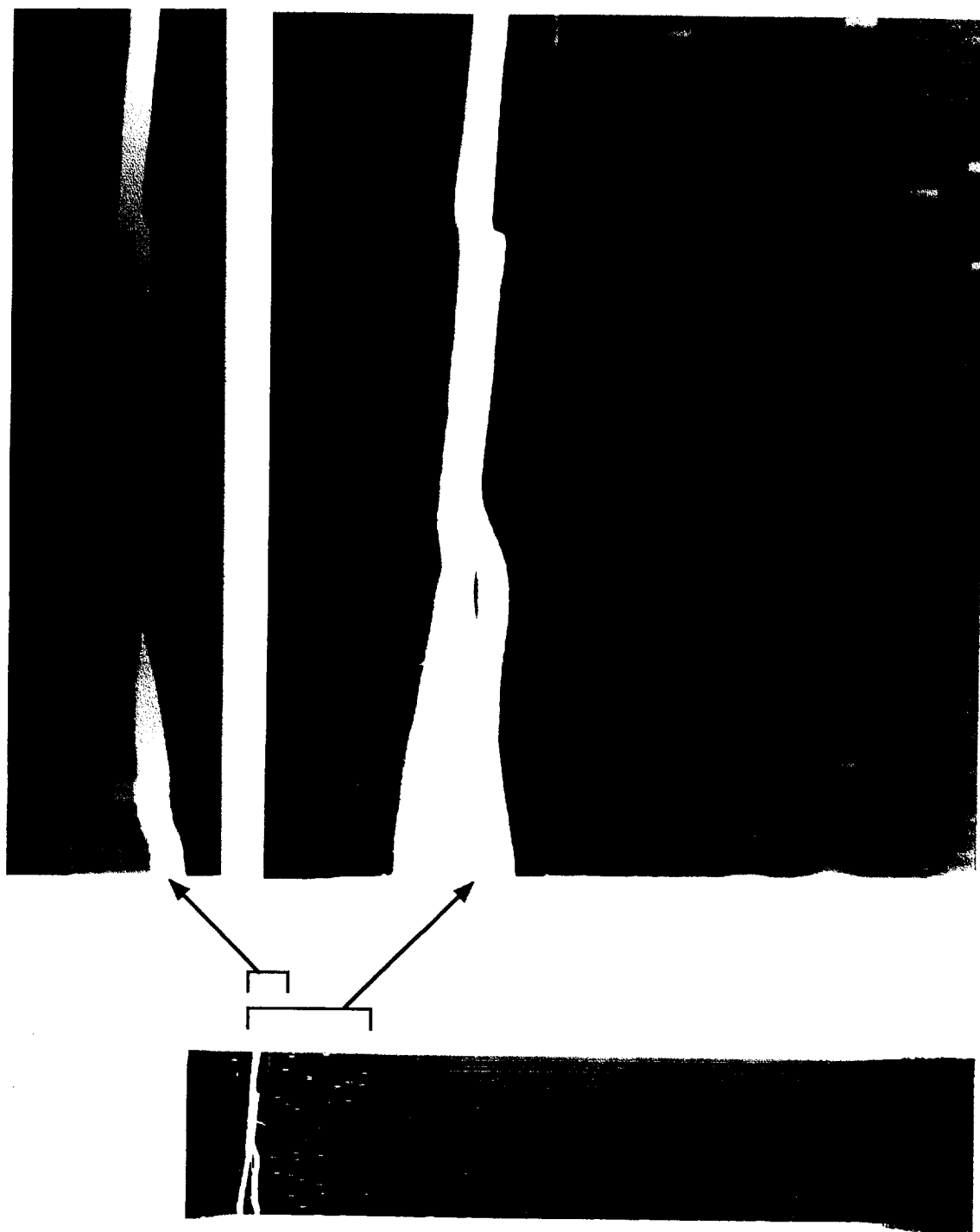


Figure 6.8.—Microfocus radiographs of [0], SiC/RBSN specimen after failure.

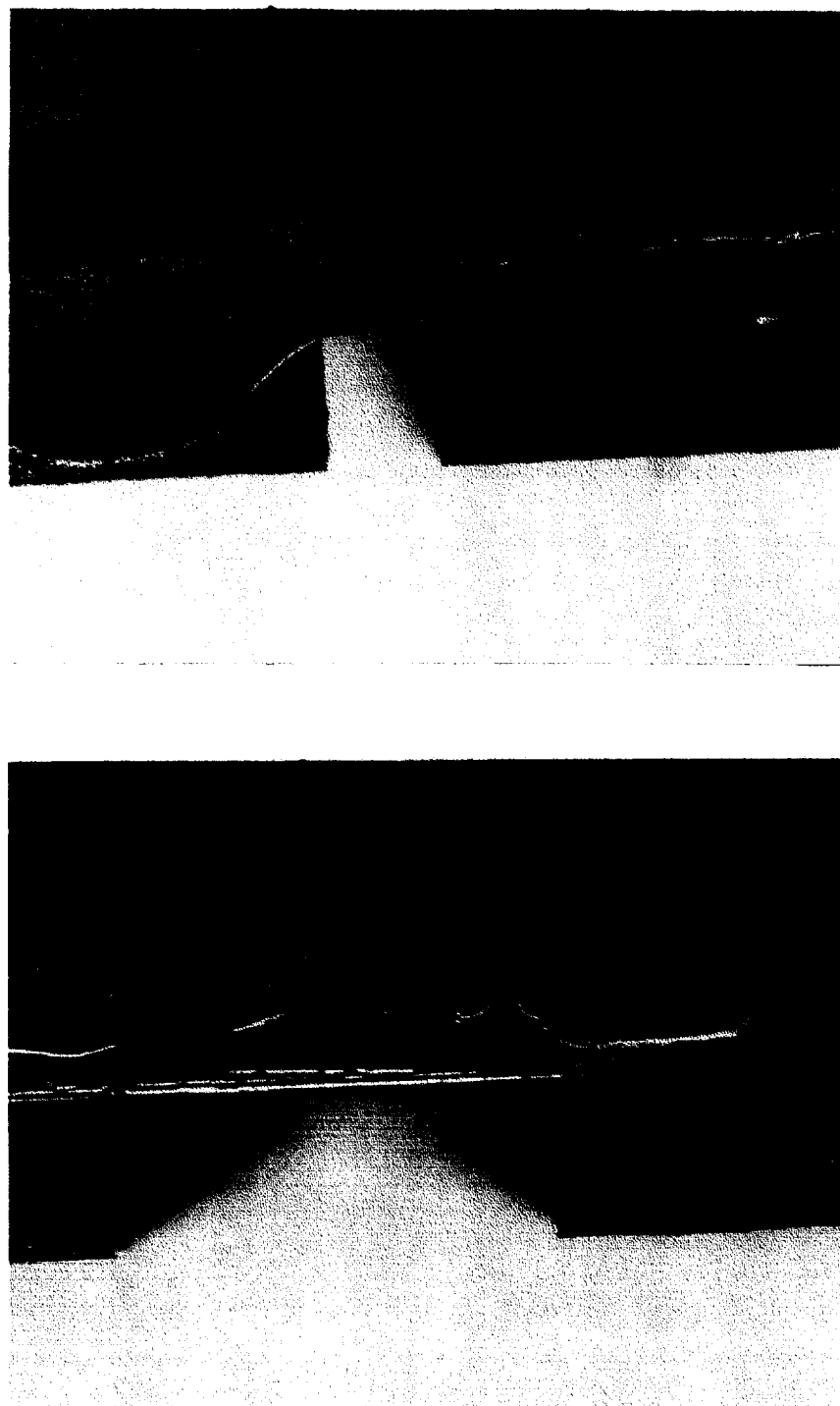
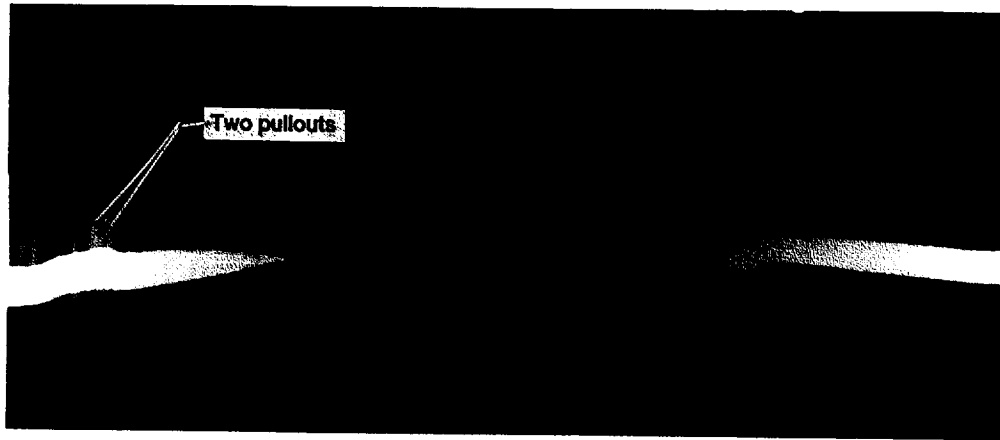
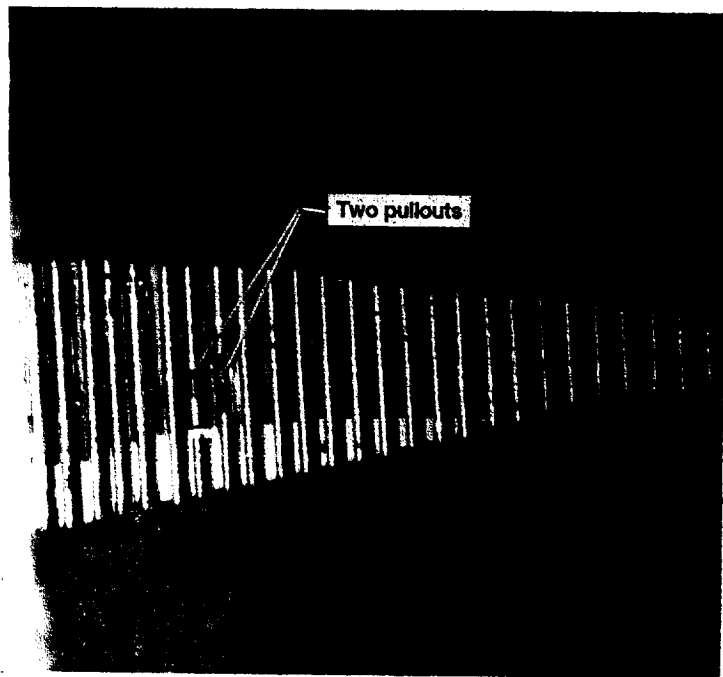


Figure 6.9.—Optical micrographs showing left and right edges of [0]₁ SIC/RBSN specimen (same as in figure 6.8) after failure.



(a) Radiograph.



(a) Optical.

Figure 6.10.—Optical proof (b) of fiber pullout detection by radiography (a) In the specimen shown in figures 6.8 and 6.9.

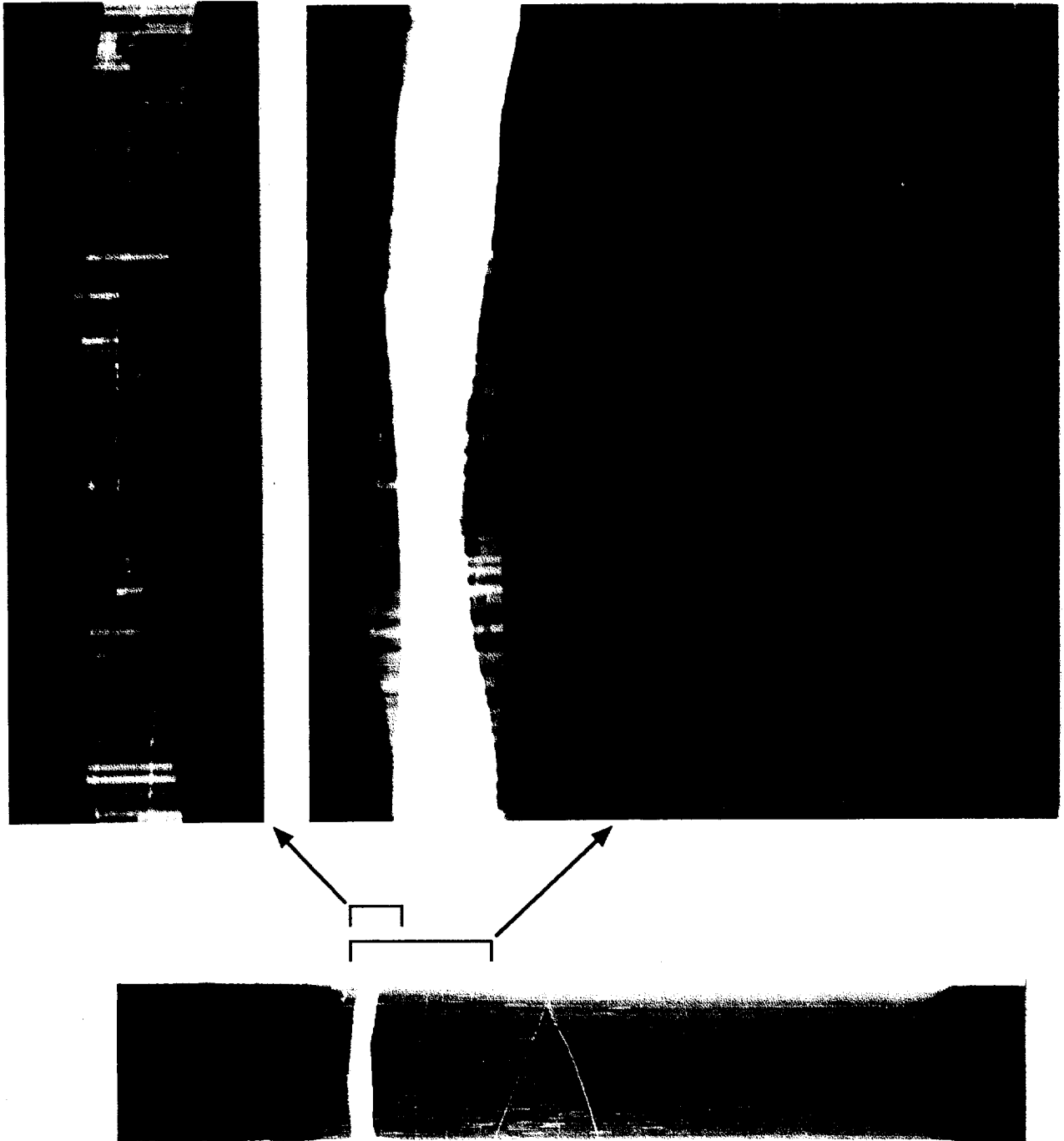


Figure 6.11.—Microfocus radiographs of $[0]_s$ SiC/RBSN specimen after failure.

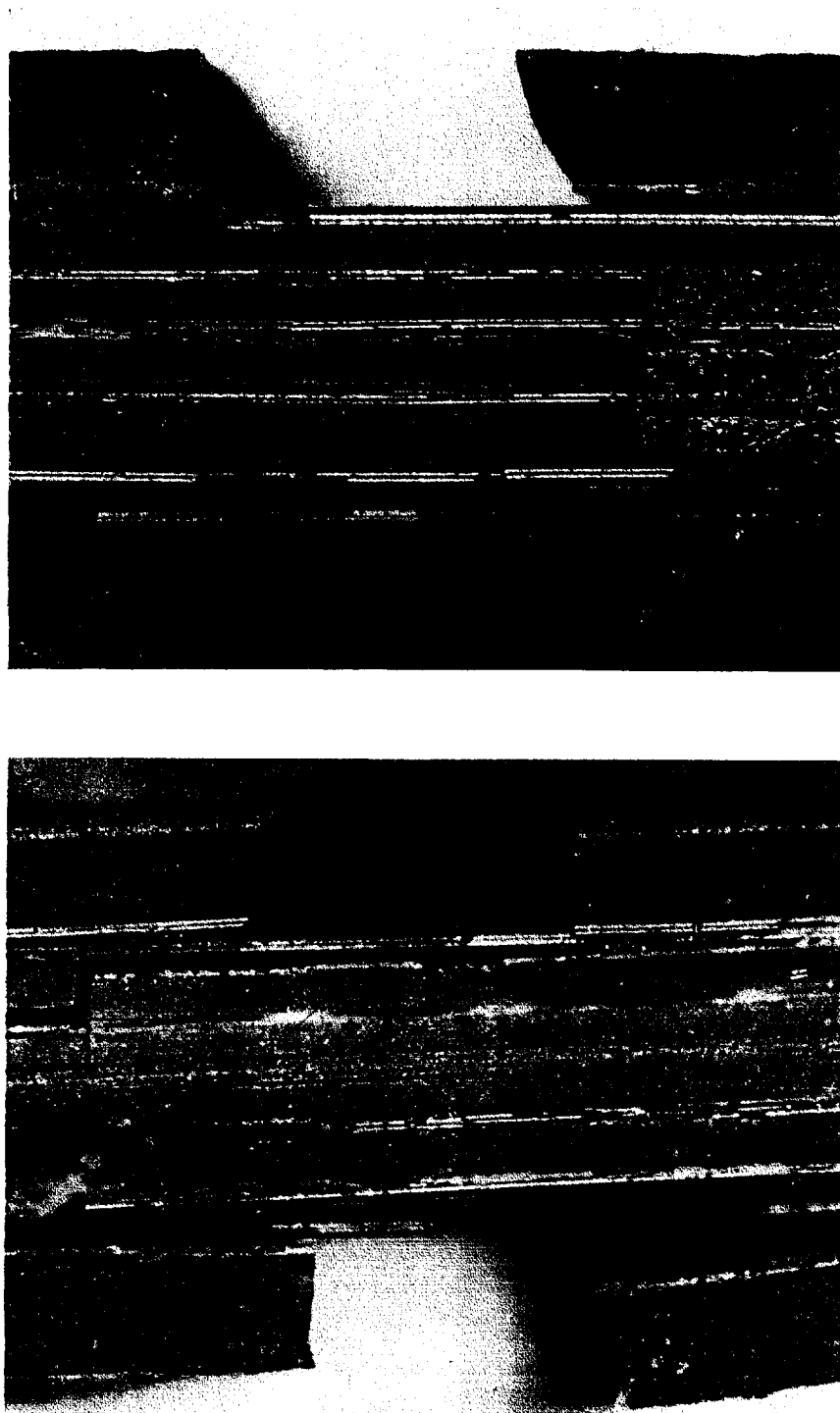


Figure 6.12.—Optical micrographs showing left and right edges of [0]₅ SIC/RBSN specimen (same as in figure 6.1) after failure.

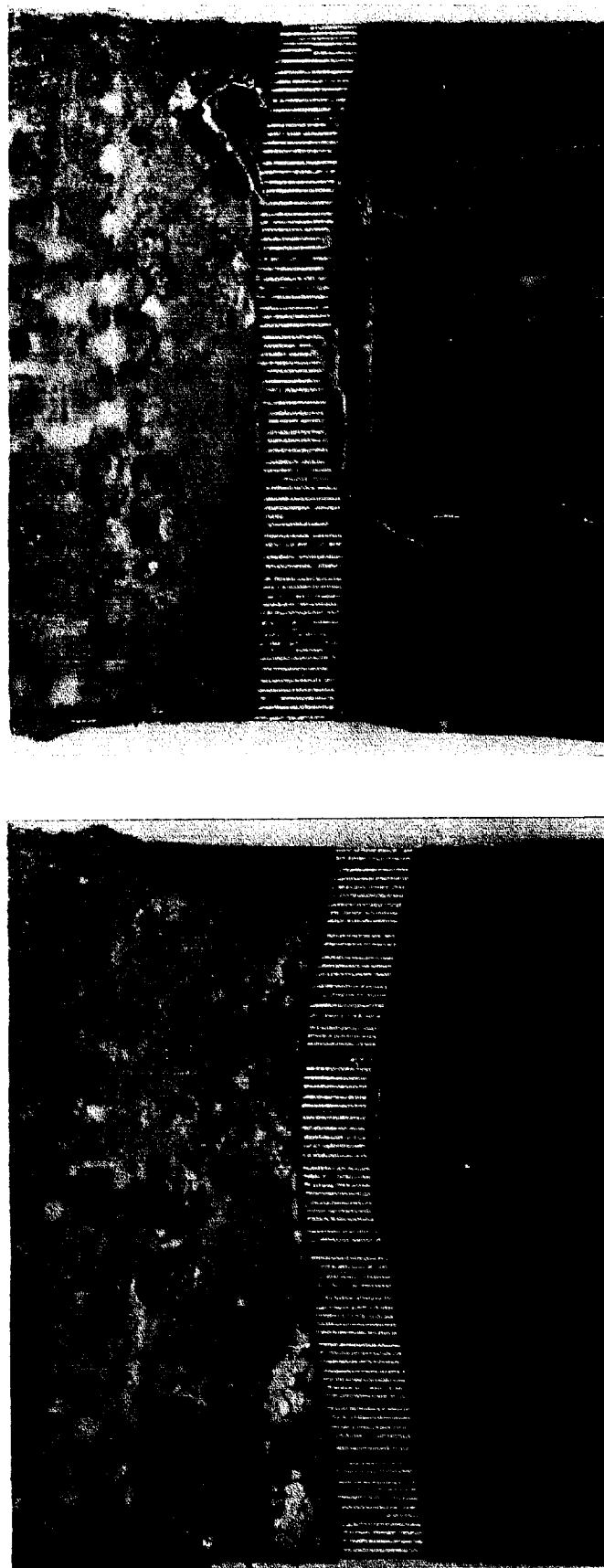


Figure 6.13.—Optical micrographs of front and back faces of $[0]_S$ SIC/RBSN specimen (same specimen as in figures 6.11 and 6.12).

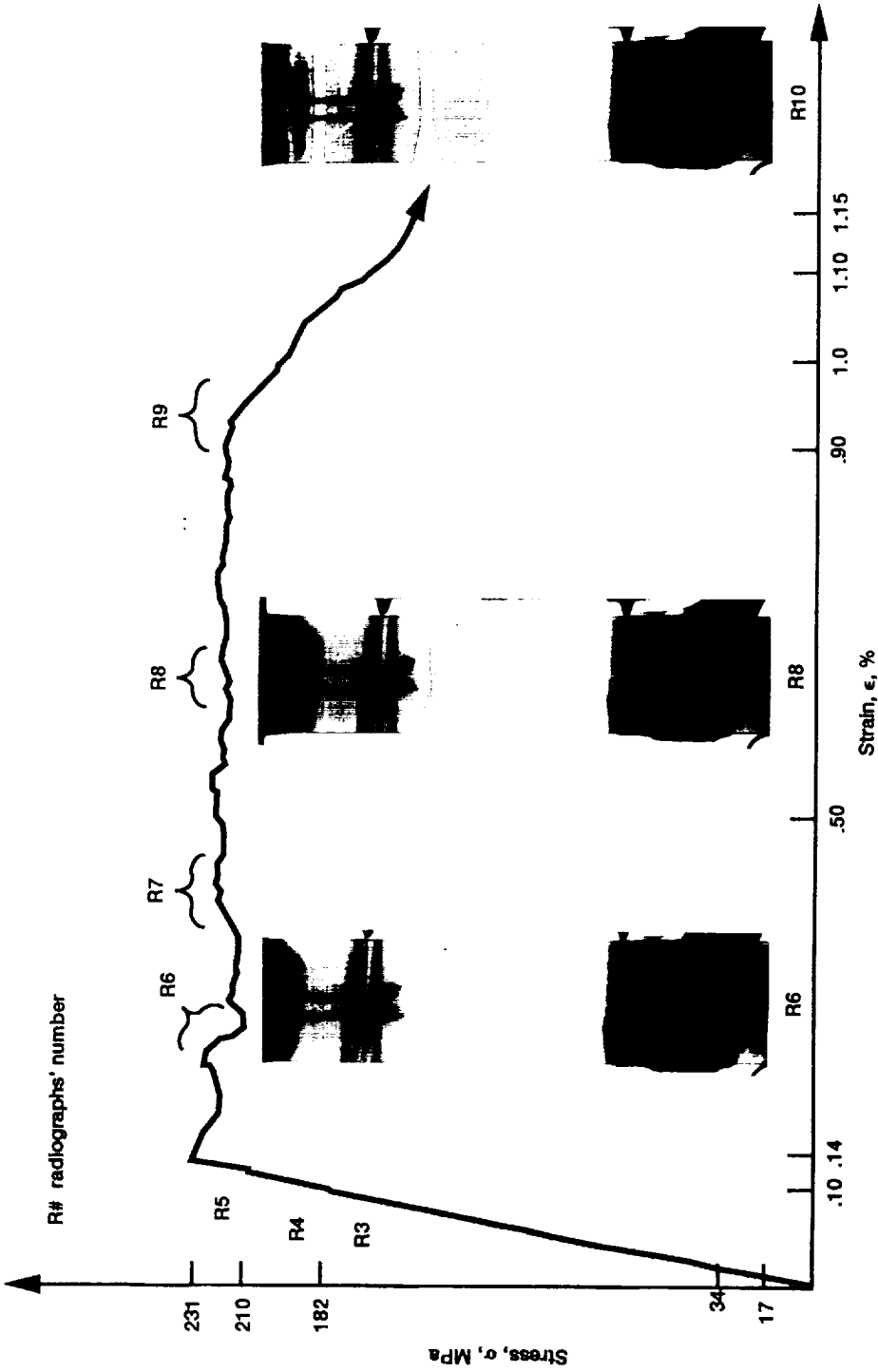


Figure 6.14.—Selected in-situ radiographs obtained during tensile loading of a [0]₅ SIC/RBSN composite (V_f ≈ 19%).

Figure 6.15 shows selected in-situ radiographs made during tensile loading history of a $[0]_8$ specimen. R0 shows the specimen at near-zero load. R8 shows the specimen at 268 MPa stress and 0.2% strain. R8 shows 6 cracks, perpendicular to the fiber orientation, that had propagated from right to left and completely through the width of the specimen. Figure 6.16 and Table III present a summary of the crack development and the corresponding crack spacing imaged in R8. R9 and R10 in figure 6.15 show 10 through-the-thickness and through-the-width matrix cracks at 410 and 538 MPa, respectively.

Figure 6.17 is a schematic of the matrix crack spacing method for calculation of estimating the interfacial shear strength, τ_f , based on the Aveston, Cooper, and Kelly (ACK) theory (Aveston et al., 1971).

$$\tau_f = \frac{\sigma_c^m D_f}{2.98(\bar{X})V_f(1+E_fV_f/E_mV_m)} \quad (6.2)$$

where σ_c^m is the composite stress corresponding to the first matrix crack, (\bar{X}) is the mean crack spacing, D_f is the fiber diameter, and the rest of the terms are as defined in equation (6.1). The stress, σ_c^m , was determined from the

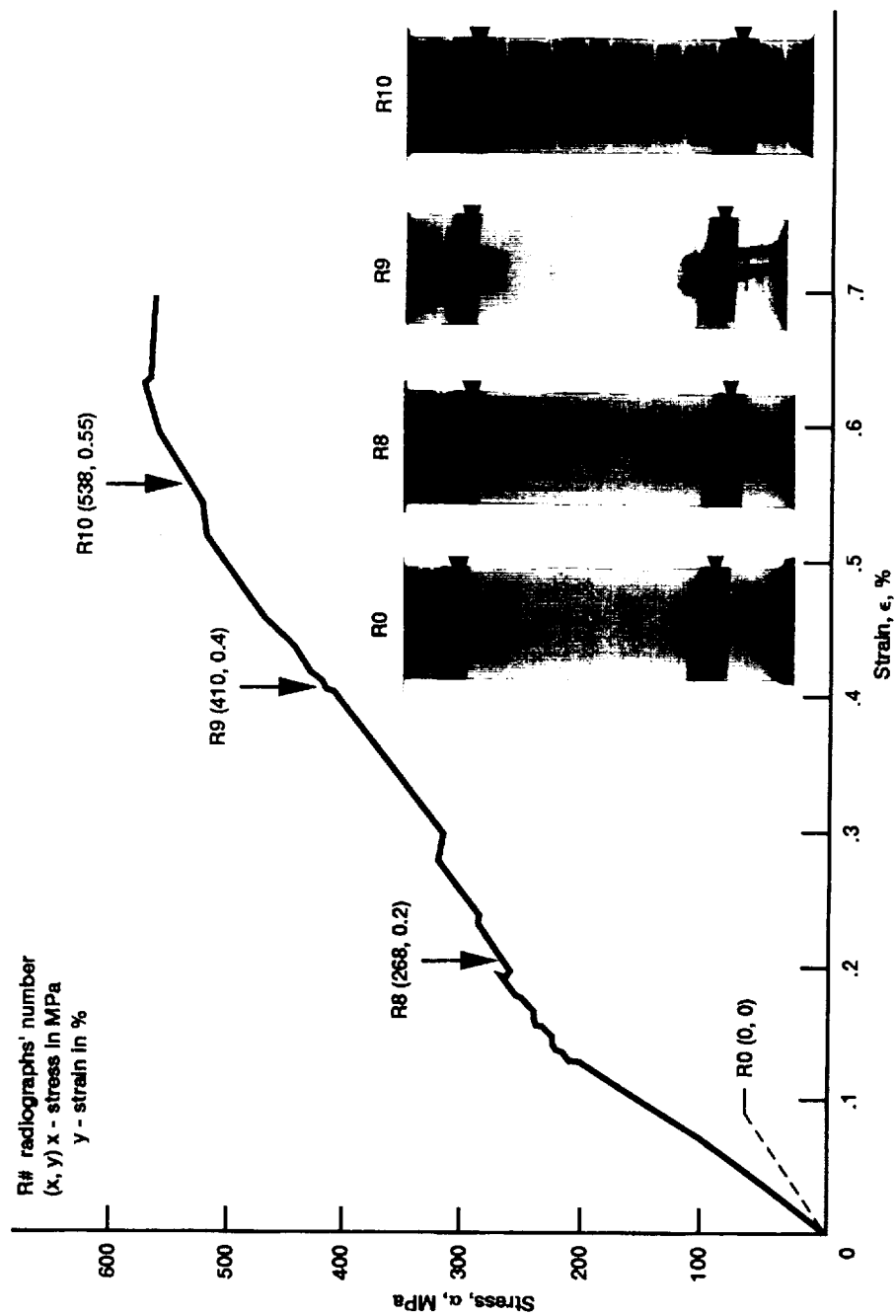


Figure 6.15—Selected in-situ radiographs obtained during tensile loading of a $[0]_{\text{SiC/RBSN}}$ composite ($V_f \approx 24\%$).



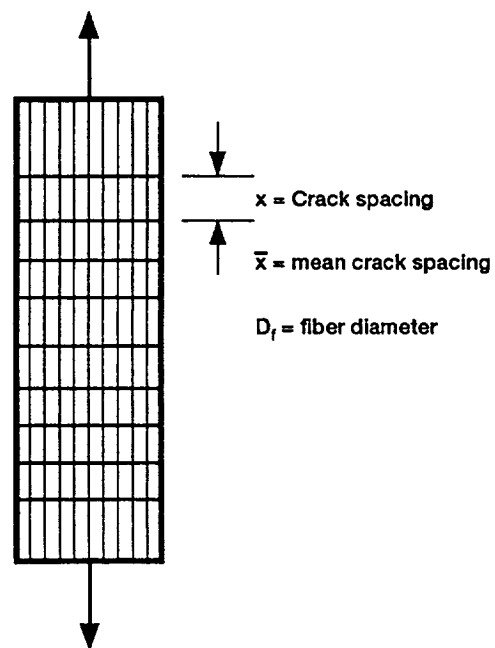
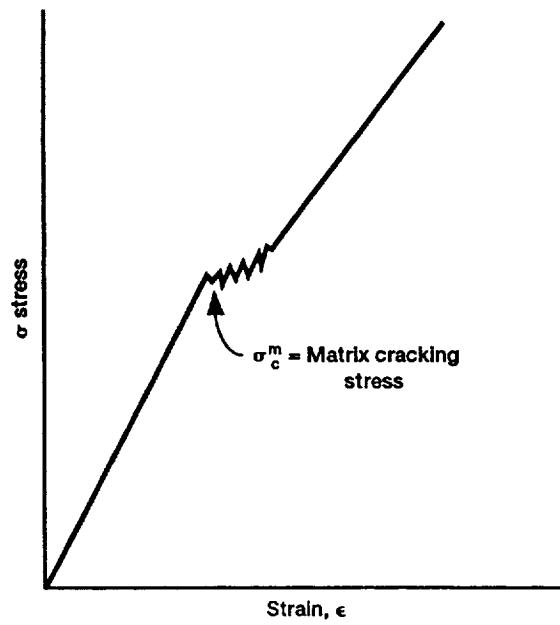
Figure 6.16.—Summary of resulting crack density as presented on radiograph number R8 at 268 MPa and 0.2% strain.

TABLE III.—VARIATION OF CRACK DENSITY VERSUS LOAD FOR SiC-RBSN
COMPOSITE ($V_f \approx 24$ PERCENT)

| Radiograph number | Stress, MPa | Strain, percent | Percent of ultimate (ult = 576 MPa) | Number of cracks detected by x-rays | Mean crack spacing, x, mm |
|-------------------|---------------|-----------------|-------------------------------------|-------------------------------------|---------------------------|
| R4 | 219 | 0.14 | 38 | ^a ₁ | ---- |
| R5 | 226 | 0.15 | 39 | ^a ₂ | ---- |
| R6 | --- | ---- | -- | ^a ₃ | 8.56 |
| R7 | 258 | 0.18 | 45 | ^a ₅ | 8.02 |
| R8 | 268 | 0.20 | 47 | ^a ₆ | 6.42 |
| R9 | 410 | 0.40 | 71 | ^b ₁₀ | 3.56 |
| R10 | 538 | 0.55 | 93 | ^b ₁₀ | 3.56 |
| R12 | After failure | | | ^b ₁₁ | 3.47 |

^aNot across - width cracks.

^bAcross-width and through-thickness cracks.



$$\tau_f^* = \frac{\sigma_c^m D_f}{2.98(\bar{x}) V_f (1 + E_f V_f / E_m V_m)}$$

* Aveston, Cooper, and Kelly

Figure 6.17.—Matrix crack spacing method (τ_f).

stress-strain curve data collected using the clip-on gauge extensometer. σ_c^m was determined by locating the first deviation from the first linear region of the curve. σ_c^m is confirmed by the stress-strain data collected from adhesively bonded strain gauges. The mean crack spacing, (\bar{X}) , was measured from the radiographs taken between 71 and 93 percent of ultimate engineering strength. For the $[0]_8$ composite with a 24% fiber volume fraction, 3.56 mm mean crack spacing, 195 MPa composite stress at first matrix crack, 390 GPa fiber modulus, and 110 GPa matrix modulus, the interfacial shear strength is calculated to be 5 MPa using equation (6.2). This value for interfacial shear strength agrees with previously obtained data via pushout tests (Eldridge, 1990; Eldridge, et al., 1991) and crack spacing method (Bhatt, 1990).

Figures 6.18 thru 6.20 display different failure mechanisms between an optimized (Fig. 6.18) and an overprocessed (Fig. 6.19) composite. In the optimized case, fibers bridge the cracks and prevent a catastrophic failure. In the overprocessed case, random fiber pullout is evident throughout the gauge length. Some fibers were broken due to overprocessing (high tensile residual stress in fibers) as depicted in figure 6.19 even before testing. Apparently, overprocessing degraded the fiber coating (Fig. 6.20) and weakened or disrupted the interface.

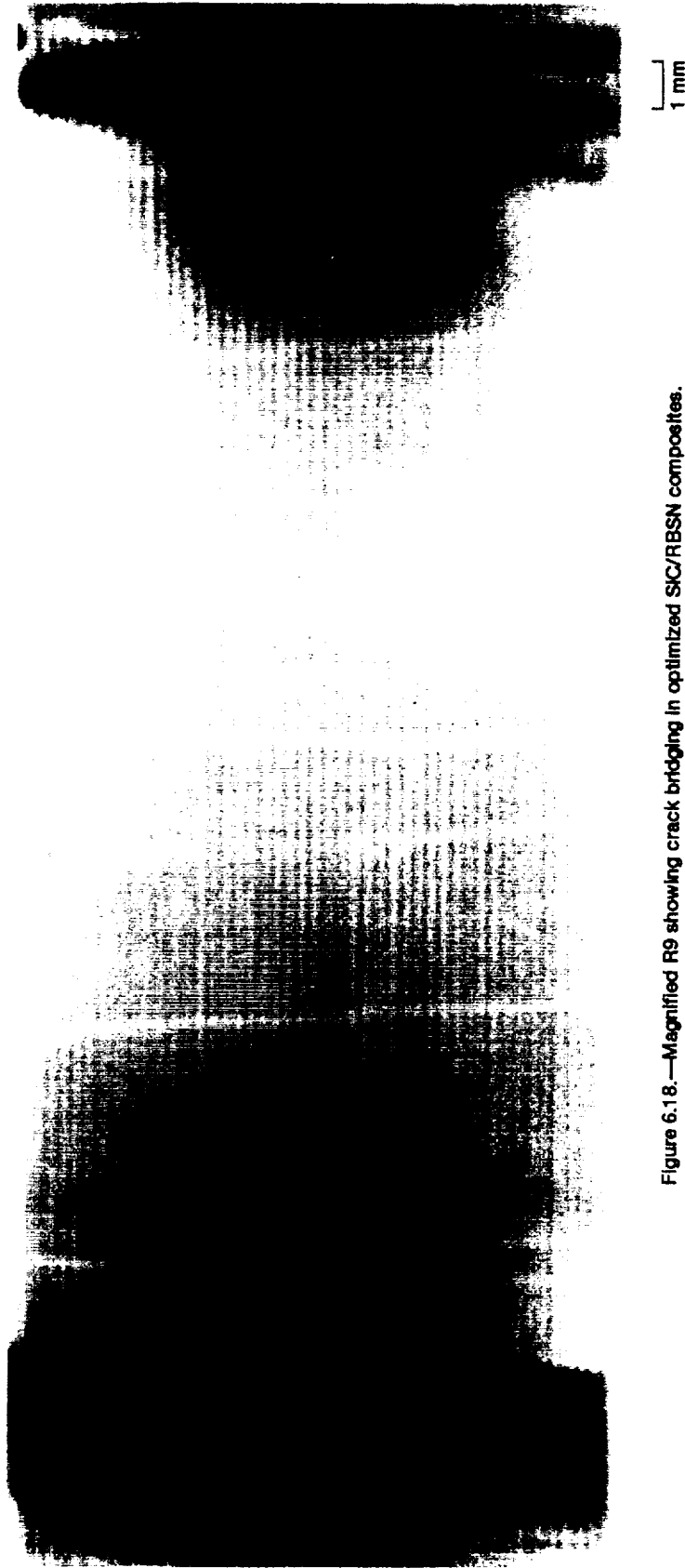


Figure 6.18.—Magnified R9 showing crack bridging in optimized SIC/RBSN composites.

ORIGINAL PAGE IS
OF POOR QUALITY

PRECEDING PAGE BLANK NOT FILMED

Page 200 Continued on next page

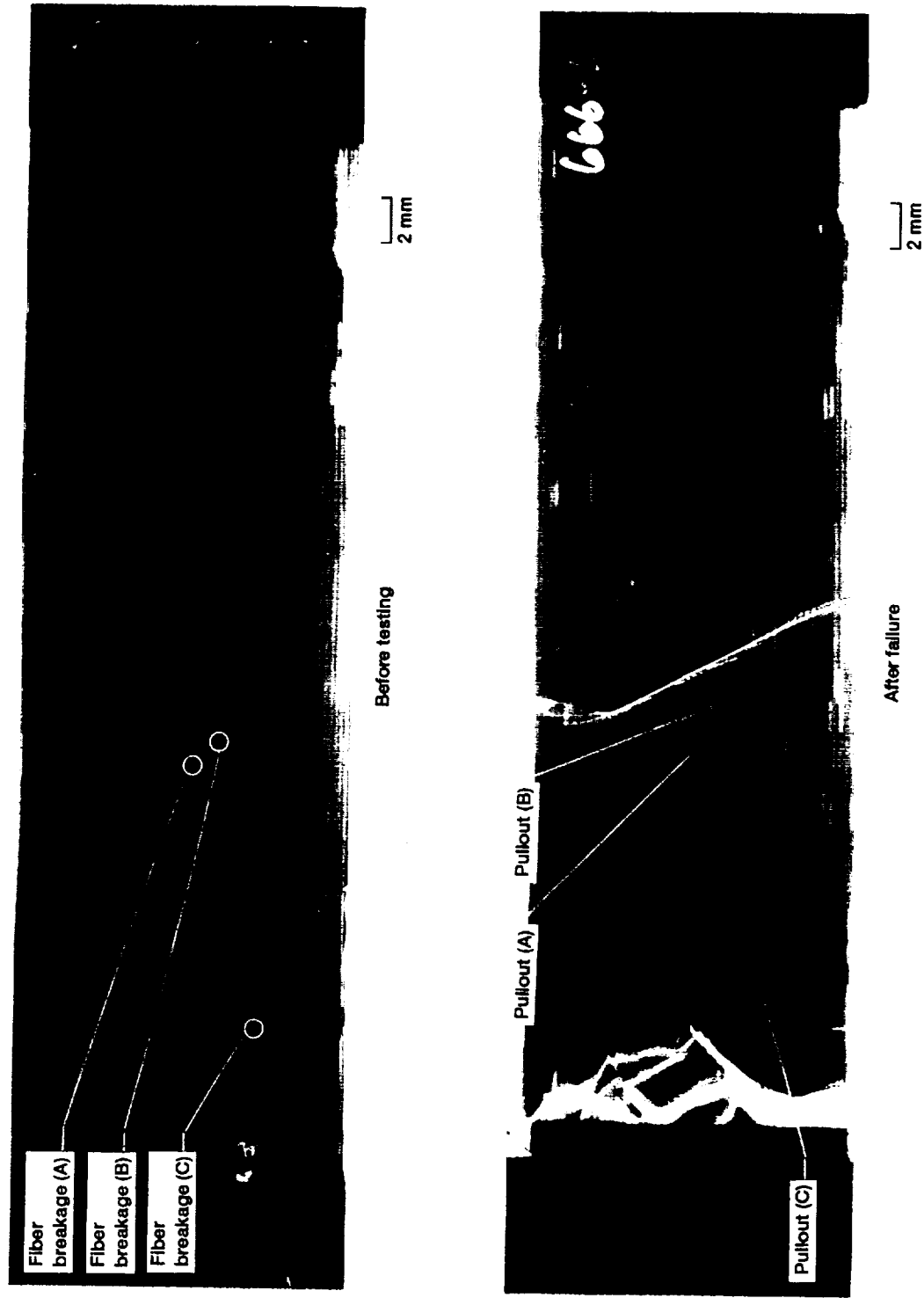


Figure 6.19.—Overprocessed 8-ply SIC/RBSN composite.

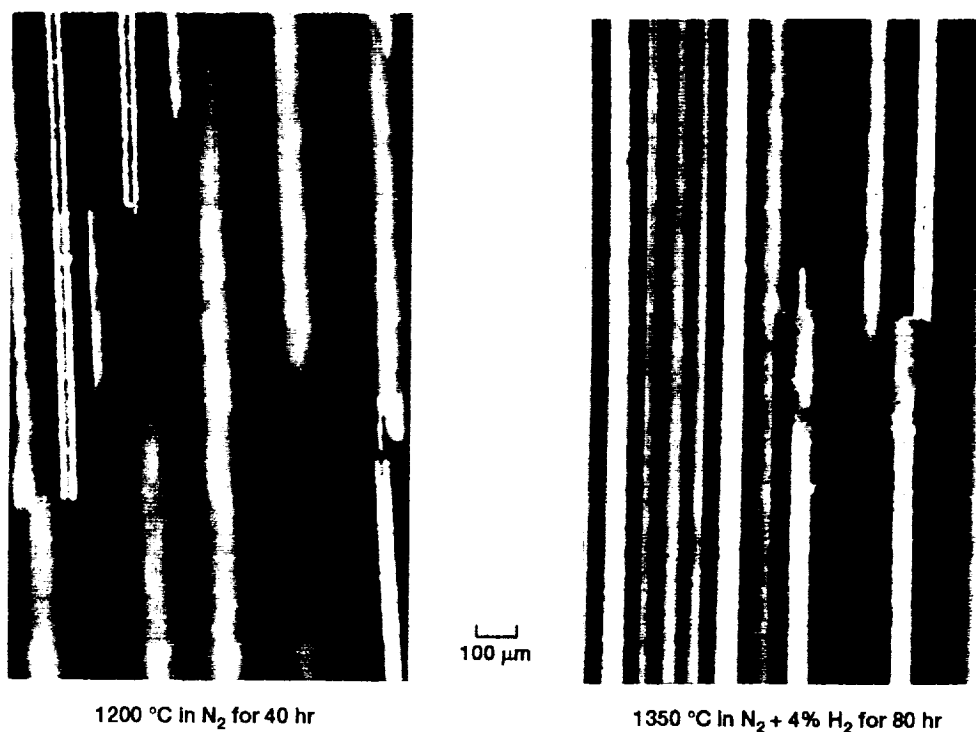


Figure 6.20.—Fractured SCS-6 fibers in 8-ply SiC/RBSN composites.

ORIGINAL PAGE
COLOR PHOTOGRAPH

ORIGINAL PAGE IS
OF POOR QUALITY

PRECEDING PAGE BLANK NOT FILMED

224

Discussion

Significance of radiographic characterization

Radiography of silicon powder cloths and SiC/RBSN panels helped identify: (1) the presence and type of impurities, and (2) the local density variations within each panel and between panels. This information presented options for designing the tensile specimens. Specimens that contain large volumetric flaws could be monitored and compared with specimens that were free of these flaws. Specimens that contained excessive local density variations could be compared with specimens that had minor local density variations. Consequently, based on whether or not impurities and local density variations are affecting the fracture behavior of the composite, materials engineers can modify powder processing or composite fabrication in order to free the composite from detrimental defects.

In this study, it is found that a 0.5 mm by 1.0 mm high density region can affect the fracture behavior of the $[0]_1$ composite (Fig. 6.6) because it behaves like a monolithic ceramic. (Fig. 6.5). Conversely, isolated and randomly distributed high density inclusions less than 150 μm in diameter do not directly affect the fracture behavior of the $[0]_1$ and $[0]_3$ specimens. Similarly high density inclusions up to 225 μm in diameter did not appear to affect fracture

behavior of the $[0]_5$ composites. Local density variations within the tensile specimens do not seem to affect fracture behavior. These preliminary conclusions are based on the limited number of samples available for this study.

Microfocus radiography of failed specimens proved useful in detecting (1) fiber pullout, (2) cracks, and (3) crack branching. This study demonstrated the need for and advantages of microfocus over conventional radiography in studying and explaining the fracture behavior of composites.

Mechanical properties

The primary modulus before first matrix cracking of the composite, E_{pc} , is about the same, (within 12%), for all $[0]_1$, $[0]_3$, $[0]_5$ and $[0]_8$ composite specimens. These primary moduli correspond to within 1% to 12% of the rule-of-mixtures composite modulus, $E_{(rom)c}$, defined in equation (6.1). Overestimates on the order of 12% can be explained by the fact that the one-ply and the three-ply materials were thinner and hence denser than the normal RBSN matrix which modulus is about 110 MPa. Close agreement between E_{pc} 's and $E_{(rom)c}$'s, is indicative of an adequate load transfer between fibers and matrix (Bhatt, 1990).

The first matrix cracking strains and stresses of the $[0]_1$ and $[0]_3$ values are also the strain-to-failure and the

ultimate strengths of these specimens, respectively. In contrast, first matrix stress and strain for $[0]_5$ (19% volume fraction) are very close to those of $[0]_8$ (24% volume fraction), where the strain to failure showed great enhancement over the one-ply and the three-ply, and the 5-ply composite specimens.

The ultimate tensile strength increases with the fiber volume fraction of all composite specimens because it is primarily controlled by the bundle strength of the fibers (Bhatt, 1990).

Significance of in-situ radiography

In the case of $[0]_1$ and $[0]_3$ composites, in-situ radiography images cracks and fiber pullouts after ultimate failure. This is only achieved by testing samples in the displacement control mode. Under the load control mode sudden catastrophic failure occurred at ultimate strength and precluded making the x-ray exposure. In-situ radiography during failure and in-situ and microfocus radiography after failure help identify the presence and location of (1) matrix cracks on the ply level, (2) fiber pullout, and (3) fiber matrix debonding. Fiber pullouts and matrix cracks, opaque for optical evaluation, require imaging by radiography.

In the case of $[0]_5$, failure sequences are radiographically imaged in the non-linear region, and during and after the fiber pullout region (Fig. 6.14). Breakages of fibers cannot be imaged until fibers start pulling apart. Pre-existing microcracks cannot be imaged because of resolution limitations of the x-ray system. The first matrix crack is imaged after the stress-strain curve indicated that matrix cracking occurred. Thereafter, multiple cracks are imaged as the specimen is strained, and fibers start to pull out. It is also noted that matrix cracks would tend to close until the final failure of the composite. At this point fiber pullout, fiber matrix debonding, and fiber breakage are readily imaged. After failure, optical examination demonstrates that matrix cracks had propagated within lamina across the width of the sample but not through the thickness.

In the case of $[0]_8$, in-situ radiography was able to image matrix crack development throughout the tensile loading history as shown in figures 6.15 and 6.16 and as summarized in Table III. In-situ radiography enables the use of the mean crack spacing method to determine the interfacial shear strength as defined in equation (6.2), and also verifies the experimental procedure (Bhatt, 1985) used to determine τ_f . From Table III and figure 6.15, it is apparent that the number of major matrix cracks and corresponding spacings do not change between 71% and 93% of

ultimate strength. This verifies that the procedure to unload the sample at about 75% (Bhatt, 1985) of ultimate load to perform the crack spacing measurements were done in the proper loading region. The x-ray monitoring technique is preferable to optical methods (Bhatt, 1985), because, first stopping the test and unloading is not practical. Second, estimating the presence of cracks which have already closed due to unloading leads to an overestimate of τ_f . Third, the ultimate strength is real not estimated from other similar samples. And fourth, if the sample shatters into fragments after failure or fails earlier than expected the cracks have already been imaged and spacings can be measured from the x-ray film. Further, even in-situ optical monitoring will not deliver the above information in a reasonable time because the high magnification needed to monitor the cracks reduces the imaging field and the working focal length. In addition in-situ optical monitoring will miss hidden cracks in sub-plyes.

Conclusion

In-situ radiography of room temperature tensile testing of SCS-6 silicon carbide fiber reinforced reaction-bonded silicon nitride (SiC/RBSN) composite specimens is a reliable method for monitoring damage accumulation, for determining the interfacial shear strength between the SiC fiber and the

RBSN matrix by the matrix crack spacing method, and for identifying different failure mechanisms. Matrix cracking, fiber-matrix debonding, and fiber pullout are imaged throughout the tensile loading of the specimens. Radiographic evaluation before, after, and during loading provides data on the effect of pre-existing volume flaws, e.g., high density inclusions, and on the effect of local density variations on the fracture behavior of composites. In situ radiography can provide a basis for (1) identification of important failure mechanisms, (2) validation of analytical models, (3) verification of experimental procedures, and (4) optimization of fabrication processes through timely feedback of test useful information.

CHAPTER VII

GENERAL DISCUSSION

The PSDR system provides several unique capabilities:

- (1) precise measurement of x-ray attenuation
- (2) scan imaging with high spatial resolution on the order of $\leq 100 \mu\text{m}$
- (3) x-ray beam profiling and
- (4) investigating stability of different x-ray sources.

The PSDR system is limited by long scan times and photon starvation in the case of thick monolithic specimens and composite constituents of comparable total mass attenuation coefficient.

Opportunities exist for improving the system's contrast sensitivity and penetration power by using (1) higher kV x-ray tubes, (2) microfocus tubes, (3) array detectors (preferably area detectors), and (4) multichannel analyzers and energy filters. The PSDR of this study nevertheless proved instrumental in precise x-ray attenuation measurements and characterization of thin monolithic materials.

Physical density was correlated with CT number giving a calibration curve for monolithic ceramic materials. This reduced interpretational ambiguities associated with the indirectness of NDE measurements. Multiparametric probing and signal analysis is essential for removing ambiguities in collecting complementary and corroborative data. This is stressed in chapter IV where film radiography and acoustic microscopy were used to substantiate XCT findings.

XCT density information described in chapter V proved helpful in identifying fabrication-related problems and comparing different processing methods. For example consolidation of cylindrical rods versus annular rings. XCT helped avoid cutting through fibers during final machining in the case of the rod samples. XCT is now routinely used to guide machining of components to final dimensions.

XCT density information was shown to be an important guide in structural design and modeling of composite components. Distortions in structural constituents, which may cause nonuniform material responses at high temperatures and under different loading conditions, is detected by XCT. NDE coupled with destructive verifications will certainly improve and accelerate the development of advanced composite components.

Three-dimensional volumetric density variations in composite components is readily imaged by XCT and can guide geometric modeling of composite constituents. Moreover XCT

can help determine composite spatial variations of stiffnesses if CT artifacts are minimized. Engineering tomography, which incorporates XCT density information in finite element modeling, can significantly help in predicting life and serviceability of composite components.

Predicting life of components cannot be based on coupon test results. Because the mechanical behavior of components is mainly affected by different fabrication processes that are unique to component fabrications. In addition issues such as nature of loading, mean residual stresses, multiaxial state of stress, and size effects are component dependant distinctive characteristics. Thus, XCT in specific and often NDE modalities in general help in reducing engineering approximation approaches, improve statistical interpretation (imaging modalities are the source of a very large data base) of life and deterministic life prediction analyses, and ameliorate and accelerate damage tolerance assessment.

Noninvasive in-situ monitoring, using the IXMTS system described in chapter VI, demonstrated many benefits in understanding the mechanical behavior of emerging advanced composite material systems.

Specifically for the particular material systems examined in this work, it is found that a 0.5 mm by 1.0 mm high density region can affect the fracture behavior of the $[0]_1$ ceramic matrix composite. Comparatively isolated and

randomly distributed high density inclusions less than 150 μm in diameter do not adversely affect the fracture behavior of the $[0]_1$ and $[0]_3$ ceramic matrix composite specimens tested. Similarly, high density inclusions up to 225 μm in diameter are found not to affect the fracture behavior of the $[0]_5$ ceramic matrix composite specimens. Finally, it is found that local density variations within the composite tensile specimens have little affect on their fracture behavior.

The first matrix cracking strains and stresses of $[0]_1$, and $[0]_3$ specimens are also the strain-to-failure values and the ultimate strengths of these specimens, respectively. In contrast, first matrix stress and strain for $[0]_5$ (19% volume fraction) are very close to those of $[0]_8$ (24% volume fraction), where the strain to failure showed great improvement over the one-ply and the three-ply, and the 5-ply composite specimens. A fiber volume fraction of over 19% assures rule-of-mixtures-predicted composite behavior. Ultimate tensile strength increased with the fiber volume fraction for all composite specimens tested because it is primarily controlled by the bundle strength of the fibers.

Microcracks which may have existed in the linear region, can not be imaged because of limitations in resolution and detection capabilities of the x-ray system used. But, newly formed matrix cracks are readily imaged

after loading beyond the linear region. Multiple cracks are imaged as the specimen is further strained. When fibers start to pull out, the matrix cracks close until the final failure of the composite. At this stage fiber pullout, fiber matrix debonding and fiber breakage are imaged.

In the case of $[0]_8$ ceramic matrix composite, in-situ radiography imaged the matrix crack development throughout the tensile loading history. This enabled the use of the mean crack spacing method to determine the interfacial shear strength, and verification of the experimental procedure used for determining τ_f .

X-ray monitoring of the fracture process is preferred over optical methods because 1) optical methods are invasive in nature by using a crack enhancer agent and 2) they miss hidden cracks and anomalies located below the surface.

Microfocus radiography of failed specimens proved useful in detecting fiber pullout. Cracks and crack branchings that did not close after failure were imaged. This clearly showed the advantage of microfocus over conventional radiography in studying and explaining the behavior of composites under load. This further calls upon using a microfocus source to enhance the imaging capabilities of the in-situ system.

CHAPTER VIII

CONCLUSIONS

This dissertation encompassed development and application of x-ray attenuation measurement systems capable of 1) characterizing density variations in monolithic ceramics, ceramic and intermetallic matrix composites and 2) noninvasively monitoring damage accumulation and failure sequences in ceramic matrix composites tensile testing at room temperature. Volumetric density characterizations were performed on laboratory samples and on subscale engine components. In-situ monitoring of damage accumulation was only performed on tensile specimens.

This dissertation accomplished the development of 1) a point scan digital radiography system and 2) an in-situ x-ray material testing system. The former was used to characterize density variations in monolithic ceramics and ceramic composites and the latter was used to image the failure behavior of silicon carbide fiber reinforced reaction bonded silicon nitride matrix composites. To

extend the work to NDE of components, state of the art x-ray computed tomography was investigated to determine its capabilities and limitations in characterizing density variations of a silicon carbide rotor, a silicon nitride blade, and a silicon carbide fiber reinforced beta titanium matrix rod, rotor and ring. Microfocus radiography, conventional radiography, scanning acoustic microscopy, and metallography were used to corroborate x-ray computed tomography findings.

Point scan digital radiography was found to be a viable technique for characterizing density variations in monolithic ceramic specimens. But it was limited and time consuming in characterizing ceramic matrix composites. Precise x-ray attenuation measurements, reflecting minute density variations, were achieved by photon counting and by using micro-collimators at both source and the detector.

X-ray computed tomography was found to be a viable attenuation measurement technique for measuring cross sectional volumetric density variations in monolithic ceramics and metal matrix composites. Capabilities and limitations of x-ray computed tomography for characterizing monolithic ceramics were established. X-ray computed tomography was successfully applied to characterizing a variety of subscale components with relatively simple geometric shapes. Tomographic data provides the information needed to deduce material densities on a spatially-defined

basis. Tomographic findings were corroborated by radiographic, ultrasonic and optical microscopic data. Capabilities and limitations of x-ray computed tomography for characterizing metal matrix composite subscale engine components were defined. CT provides spatial density information which can be incorporated in finite element modeling of composite spatial stiffnesses and in geometric modeling of structural constituents. X-ray computed tomography can accelerate the development of composite components. X-ray computed tomographic imaging identifies problems associated with manufacturing processes, guides machining of components to final dimensions, and can lead structural design engineers to evolve realistic failure and life-prediction models.

In-situ radiography of room temperature tensile testing of SCS-6 silicon carbide fiber reinforced reaction-bonded silicon nitride (SiC/RBSN) composite specimens was found a useful and reliable method for (1) monitoring damage accumulation, (2) determining the interfacial shear strength between the SiC fiber and the RBSN matrix by the matrix crack spacing method, and (3) identifying principal failure mechanisms. Matrix cracking, fiber-matrix debonding, and fiber pullout were imaged during tensile loading of CMC specimens. Radiographic evaluation before, after, and during loading provided data on the effect of preexisting flaws, e.g., high density inclusions, and on the effect of

local density variations on the fracture behavior of composites. It is concluded that this approach can provide a basis for (1) identification of different failure mechanisms, (2) validation of analytical models, (3) verification of experimental procedures, and for (4) optimization of fabrication processes through proper feedback.

Results from such in-situ monitoring of coupon testing coupled with materials characterization of related subscale components can immensely improve component structural modeling and life prediction. This modeling and prediction would be otherwise non attainable, because of the enormous cost attached to modeling based on direct testing of subscale components.

CHAPTER IX

FUTURE RESEARCH

This dissertation identified potentials for extending the research activities in several areas:

From chapter III, point scan digital radiography can be improved by using a relatively high kV microfocus source, a multichannel analyzer for selective energy analysis, and by enlarging the collimation at the detector. This will enhance precision x-ray attenuation measurements for discerning minute material density/composition variations, for distinguishing thickness variations, and for detecting defects and differentiating between their chemical composition.

From chapters IV and V, further work in the high resolution and high energy x-ray tomography is needed 1) to extend the calibration density - CT number data, 2) to allow the characterization of thin and complex shaped ceramics, 3) to allow the characterization of thick and relatively dense MMC composites, 4) to eliminate the photon starvation

problem in complex shaped ceramic parts, and 5) to reduce the scanning time. Further, research in revolutionizing the XCT scanning geometry by placing the x-ray source inside the ring or rotor and the detector on the outside would call for simultaneous modification of existing reconstruction algorithms. This scanning geometry will permit the use of microfocus tubes at lower kV than their conventional counterparts because of the reduction in the x-ray path within the material under evaluation. In addition engineering tomography shall be pursued more aggressively for NDE to help in life prediction of real components.

From chapter VI, research should be extended to real time microfocus radiography and/or near real time digital radiography with an advanced area detector in order to monitor the mechanical behavior of emerging CMC and MMC with fibers (10 to 70 μm) much smaller than the SCS-6 fiber. Also scatter radiation rejection techniques (mechanical and/or electronic) need to be developed to better discriminate between fibers and matrices of similar densities and comparable x-ray mass attenuation coefficients. Further, similar in-situ work to chapter VI should be extended to braided and woven composites for better understanding of their damage tolerances and failure mechanisms. In addition, the research in chapter VI can be extended to study the work of pullout in order to characterize the fiber-matrix interface more closely.

Cone beam tomography and laminography need to be developed concurrently with high resolution and sizeable area sensors to provide cross-sectional information on the ply level of laminated braided and woven composites.

Standards by comparative characterization of composite samples that are fabricated differently or treated in different environments for varying time, temperature, and pressure, must be established in order for NDE to have a set of reference samples from which degradation assessment can be made during the life of the component.

BIBLIOGRAPHY

- Ackerman, J.L., et al.: The use of NMR Imaging to Measure Porosity and Binder Distributions in Green-State and Partially Sintered Ceramics. Nondestructive Testing of High Performance Ceramics, A. Vary, and J. Snyder, eds., American Ceramics Society, Westerville, OH, 1987, pp. 88-113.
- "Advanced Turbine Technology Applications Project (ATTAP)," NASA CR-185240, 1990.
- "Aeropropulsion 1991," NASA CP-10063, 1991.
- Agarwal, B.D. and Broutman, L.J., Analysis and Performance of Fiber Composites John Wiley & Sons, New York, 1979, Chapt. 2.
- "AGT (Advanced Gas Turbine) Technology Project," DOE/NASA/0168-11, NASA CR-182127, 1988.
- Andrews, H.C. and Hunt, B.R., Digital Image Restoration, Prentice-Hall, Inc., Englewood Cliffs, NJ, 1977.
- Armistead, R.A., "CT: Quantitative 3-D Inspection," Advanced Materials & Processes, Vol. 133, No. 3, Mar. 1988, pp. 42-43, 46-48
- Arnold, B.A., et al. "Digital Radiography: An Overview," Application of Optical Instrumentation in Medicine IX, J.E. Gray, et al., eds., SPIE Proc. Vol. 273, 1981, pp. 215-226.
- Arnold, B.A., "Digital Radiography: A Technology Overview," Application of Optical Instrumentation in Medicine X, G.D. Fullerton, et al., eds., SPIE Proc. Vol. 347, 1982, pp. 347.
- ASTM standards, Metals Test Methods and Analytical Procedures, Vol. 3.03, Nondestructive Testing, ASTM, 1991.
- Aveston, J., Cooper, G.A., and Kelly, A., "Single and Multiple Fracture," The Properties of Fibre Composites, IPC Science and Technology Press Ltd., Surrey, England, 1971, pp. 15-26.
- Azevedo, S.G., "Model Based Computed Tomography for Nondestructive Evaluation; An Overview and Proposal," UCID-21380, Lawrence Livermore National Laboratory, Jan. 1988.

- Baaklini, G.Y. and Roth D.J., "Probability of Detection of Internal Voids in Structural Ceramics using Microfocus Radiography," Journal of Material Research, Vol. 1, No. 3, May-June 1986, pp. 457-467.
- Baaklini, G.Y., Kiser, J.D., and Roth, D.J., "Radiographic Detectability Limits for Seeded Voids in Sintered Silicon Carbide and Silicon Nitride," Advanced Ceramic Materials, Vol. 1, No. 1, Jan. 1986, pp. 43-49.
- Baaklini, G.Y., "NDE Reliability and Process Control for Structural Ceramics," Journal of Engineering for Gas Turbines and Power, Vol. 109, No. 3, July 1987, pp. 263-266.
- Baaklini, G.Y. and Abel, P.B., "Radiographic and Ultrasonic Characterizations of Sintered Silicon Carbide," Materials Evaluation, Vol. 46, No. 11, Oct. 1988, pp. 1477-1483.
- Baaklini, G.Y., Generazio, E.R., and Kiser, J.D., "High Frequency Ultrasonic Characterization of Sintered Silicon carbide," Journal of the American Ceramics Society, Vol. 72, No. 3, 1989, pp. 383-387.
- Baaklini, G.Y. and Bhatt, R.T., "Preliminary X-Ray Monitoring of Damage Accumulation in SiC/RBSN," HITEMP Review-1990, NASA CP-10051, 1990, pp. 54-1 to 54-13.
- Baaklini, G.Y., et al., "Characterization of MMC Subscale Engine Components Using X-Ray Computed Tomography," HITEMP Review 1991, NASA CP-10082, 1991, pp. 33-1 to 33-14.
- Bederson, B. and Fite, W.L., eds., Atomic and Electron Physics, Academic Press, New York, 1968.
- Bendat, J.S. and Piersol, A.G., Engineering Applications of Correlation and Spectral Analysis, John Wiley & Sons, New York, 1980.
- Berland L.L., "Practical CT: Technology and Techniques," Raven Press Books, New York, 1987.
- Berthelot, A., Radiations and Matter, (English translation by F.R. Paulsen, Leonard Hill Limited, London, pp. 150-175, 1958.
- Bhatt, R.T., "Mechanical Properties of SiC Fiber-Reinforced Reaction-Bonded Si₃N₄ Composites," NASA TM-87085, 1985.
- Bhatt, R.T., "Method of Preparing Fiber-Reinforced Ceramic Materials," U.S. Patent No. 4,689,188, 1987.

- Bhatt, R.T. and Phillips, R.E., "Laminate Behavior for SiC Fiber-Reinforced Reaction-Bonded Silicon Nitride Matrix Composites," NASA TM-101350, 1988a.
- Bhatt, R.T., "The Properties of Silicon Carbide Fiber-Reinforced Silicon Nitride Composites," Whisker- and Fiber-Toughened Ceramics, R.A. Bradely, et al., eds., ASM International, Metals Park, OH, 1988b, pp. 199-208.
- Bhatt, R.T., "Influence of Interfacial Shear Strength on the Mechanical Properties of SiC Fiber Reinforced Reaction - Bonded Silicon Nitride Matrix Composites," NASA TM-102462, 1990.
- Birks, A.S., Green, R.E., Jr., and McIntire, P., eds.: Nondestructive Testing Handbook, Vol. 7, Ultrasonic Testing. American Society for Nondestructive Testing, Inc., 1991, pp. 258-266.
- Bowman, C.C. and Batchelor, B.G., "Automated Visual Inspection," Research Techniques in Nondestructive Testing, Vol. 8, R.S. Sharpe, ed., Academic Press, New York, 1985, pp. 361-444.
- Cappellini, V., Constantinides, A.G., and Emiliani, P., Digital Filters and Their Applications, Academic Press, New York, 1978.
- Cappellini, V., and Constantinides, A.G., eds., Digital Signal Processing, Academic Press, New York, 1980.
- "CATE, Ceramic Application in Turbine Engines," NASA CR-16559, Nov 1981.
- "CATE, Ceramic Application in Turbine Engines," NASA CR-174715, Oct 1984.
- "Ceramic Technology for Advanced Heat Engines Project," ORNL/TM-11859, Oak Ridge National Laboratory, Oct. 1990-Mar. 1991.
- Chulya, A., Baaklini, G.Y., and Bhatt, R.T., "Characterization of Damage and Fracture Mechanisms in Continuous Fiber-Reinforced SiC/RBSN Ceramic Matrix Composites by Acoustic Emission," HITEMP Review-1990, NASA CP-10051, 1990, pp. 55-1 to 55-15.
- Cormack, A.M., "Representation of a Function by Its Line of Integrals, with Some Radiological Applications," Journal of Applied Physics, Vol. 34, No. 9, Sept. 1963, pp. 2722-2727.

Cormack, A.M., "Representation of a Function by Its Line Integrals, with Some Radiological Applications. II," Journal of Applied Physics, Vol. 35, No. 10, Oct. 1964, pp. 2908-2913.

Eldridge, J.I., "The Mechanical Characterization of the Fiber/Matrix Interface by Fiber Push-Out Testing," HITEMP Review 1990, NASA CP-10051, 1990, pp. 64-1 to 64-11.

Eldridge, J.I., Bhatt, R.T., and Kiser, J.D., "Investigation of Interfacial Shear Strength in SiC/Si₃N₄ Composites," NASA TM-103739, 1991.

Ellingson, W.A., Ackerman, J.L., Garrido, L., Weyand, J., and DiMilia, R.A., "Characterization of Porosity in Green-State and Partially Densified Al₂O₃ by Nuclear Magnetic Resonance Imaging," Ceramic Eng. Sci. Proc., [8], pp. 503-512, 1987a.

Ellingson, W.A., Hentea, T., and Kriz, R.J., "Inspection of Advanced Ceramics with a Conventional Film-Based Tomography System: Preliminary Results," Nondestructive Testing of High Performance Ceramics, A. Vary, and J. Snyder, eds., American Ceramics Society, Westerville, OH, 1987b, pp. 132-147.

Ellingson, W.A., and Vannier, M.W., "X-ray Computed Tomography for Nondestructive Evaluation of Advanced Structural Ceramics," ANL-87-52, Argon National Laboratory, Sept. 1988.

Ellingson, W.A., Wong, P.S., Dieckman, S.L., Ackerman, J.L., Garrido, L., "Magnetic Resonance Imaging: A New Characterization Technique for Advanced Ceramics," The American Ceramic Society Bulletin, [68], pp. 1180-1186, 1989.

Evans, A.G., Kino, G.S., Khuri-Yakub, B.T., and Tittmann, B.R., "Failure Prediction in Structural Ceramics," Mater. Eval. 35 [4], 1977, pp. 85-96.

Evans, A.G., "Aspects of the Reliability of Ceramics," in Defect Properties and Processing of High Technology Nonmetallic Materials, J.H. Crawford, et al., eds., pp. 63-80, North-Holland, New York, 1984.

Evans, A.G. and Marshall, D.B., "The Mechanical Behavior of Ceramic Matrix Composites," Acta metall. Vol. 37, No. 10, pp. 2567-2583, 1989.

- Feldkamp, L.A. and Jesion, G., "3-D X-Ray Computed Tomography," Vol. 5A, D.O. Thompson, and D.E. Chimenti, eds., Plenum Press, New York, 1986, pp. 555-566.
- Friedman, W.D., Harris, R.D., Engler, P., Hunt, P.K., and Srinivasan, M., "Characterization of Green Ceramics with X-ray Tomography and Ultrasonics, Nondestructive Testing of High Performance Ceramics, A. Vary, and J. Snyder, eds., American Ceramics Society, Westerville, OH, 1987, pp. 128-131.
- Gardner, R.P. and Ely, R.L., Jr., Radioisotope Measurement Applications in Engineering, Reinhold Publishing Corporation, New York, 1967.
- Generazio, E.R., "The Role of the Reflection Coefficient in Precision Measurement of Ultrasonic Attenuation," Materials Evaluation, 43, no. 7, July 1985, pp. 995-1004.
- Generazio, E.R., Roth, D.J., and Baaklini, G.Y., "Acoustic Imaging of subtle Porosity Variations in Ceramics," Materials Evaluation, 46[10] 1338-1343, Sept. 1988.
- Geykenyesi, J.P., "Failure Analysis of Continuous Fiber Reinforced Ceramic Matrix Composite Laminates," HITEMP Review 1988, NASA CP-10025, 1988, pp. 145-162.
- Goebbels, K., "Structure Analysis by Scattered Ultrasonic Radiation," Research Techniques in Nondestructive Testing, Vol. 4, Sharpe, R.S., ed., Academic Press, New York, 1980, pp. 87-157.
- Gonzalez, R.C. and Wintz, P., Digital Image Processing, Addison-Wesley Publishing Company, 1977.
- Gopalsami, N., Dieckman, S.L., Ellingson, W.A., Botto, R.E., Wong, P.S., Yeh, H.C., and Pollinger, J.P., "Nuclear Magnetic Resonance Imaging of Green State Ceramics," Argonne National Laboratory, ANL-90/27, Aug. 1990.
- Halmshaw, R., Industrial Radiology: Theory and Practice, Applied Science Publishers, London and New Jersey, 1982.
- Harper, J.E., ARPA/NAVAIR Ceramic Gas Turbine Engine Demonstration Program, Ceramics for High Performance Applications III: Reliability, pp. 645-664, Plenum, New York, 1983.
- Hartsel, J.E. and Smith, C.J., "Advanced Materials: The Enabling Technologies for Future Ultra Bypass Engines," HITEMP Review 1990, NASA CP-10051, 1990, pp. 2-1 to 2-13.

Hemann, J.H. and Baaklini, G.Y., "Effect of Stress on Ultrasonic Pulses in Fiber Reinforced Composites," SAMPE Journal, Vol. 22, No. 4, 1986, pp. 9-13.

Heraud, L. and Spriet, P., High Toughness C-SiC and SiC-SiC Composites in Heat Engines: Whisker- and Fiber-Toughened Ceramics, R.A. Bradely, et al., eds., ASM International, Metals Park, OH, 1988, pp. 217-224.

Herman, G.T., "Principles of Reconstruction Algorithms, Section II: Advanced Principles of Reconstruction Algorithms," Radiology of the Skull and Brain: Technical Aspects of Computed Tomography, Vol. 5, T.H. Newton, and D.G. Potts, eds., C.V. Mosby, St. Louis, MO, 1981, pp. 3888-3917.

"HITEMP Review 1988: Advanced High Temperature Engine Materials Program," NASA CP-10025, 1988.

"HITEMP Review 1989: Advanced High Temperature Engine Materials Program," NASA CP-10039, 1989.

Hounsfield, G.N., "Computerized Transverse Axial Scanning (Tomography). I. Description of System," Br. J. Radiol, vol. 46, no. 552, 1973, pp. 1016-1022.

Hubbell, J.H., "Photon Cross-Sections, Attenuation Coefficients, and Mass Energy Absorption Coefficients from 10 keV to 100 GeV," NSRDS-NBS 29, National Bureau of Standards, 1969.

Hubbell, J.H., "Photon Mass Attenuation and Mass Energy-Absorption Coefficients for H, C, N, O, Ar, and Seven Mixtures from 0.1 keV to 20 MeV," Radiation Research, Vol. 70, no. 1, Apr. 1977. pp. 58-81

Hubbell, J.H., "Photon Mass Attenuation and Mass Energy-Absorption Coefficients from 1 keV to 20 MeV," International Journal of Applied Radiation Isot., Vol. 33, No. 11, Nov. 1982, pp. 1269-1290.

Hughes, J.W., "Benefits of Advanced Materials and Structures in a Mach 2.4 HSCT Turbine Bypass Engine," HITEMP Review 1991, NASA CP-10082, 1991, pp. 4-1 to 4-14.

Iwasaki, H. and Isumi, M., "Acoustic Characterization of Si_3N_4 Ceramics," J. Soc. Mater. Sci. Japan, vol. 30, no. 337, 1981, pp. 1044-1050.

- Joseph, P.M., "Artifacts in Computed Tomography," Radiography of the Skull and Brain: Technical Aspects of Computed Tomography, Vol. 5, T.H. Newton, and D.G. Potts, eds., 1981, pp. 3956-3992.
- Kak, A.C. and Slaney, M.; Principles of Computerized Tomographic Imaging, IEEE, New York, 1988.
- Kautz, H.E., and Lerch, B.A., "Preliminary Investigation of Acousto-Ultrasonic Evaluation of Metal-Matrix Composite Specimens," Materials Evaluation, Vol. 49, No. 5, 1991a, pp. 607-612.
- Kautz, H.E. and Bhatt, R.T., "Ultrasonic Velocity Technique for Monitoring Property Changes in Fiber-Reinforced Ceramic Matrix Composites," Ceramic Engineering and Science Proceedings, Vol. 12, No. 7-8, July-Aug. 1991b, pp. 1139-1151.
- Kemp, L.A.W. and Oliver, R., Basic Physics in Radiology, 2nd edition, Blackwell Scientific Publications, Oxford, pp. 215-232, 1970,
- Kerans, R.J., Hay, R.S., Pagano, N.J., and Parthasarathy, T.A., "The Role of the Fiber-Matrix Interface in Ceramic Composites," American Ceramic Society Bulletin, Vol. 68, No. 2, Feb. 1989, pp. 429-442.
- Kereiakes, J.G.; Thomas, S.R.; and Ortron, C.G., eds.: Digital Radiography Selected Topics. Plenum Press, New York, 1986.
- Kessler, L.W. and Yuhas, D.E., "High Resolution Real Time Acoustic Microscopy," Proc. ARPA/AFML Review of Progress in Quantitative Nondestructive Evaluation, D.O. Thompson, ed., AFML-TR-78-55, 1978.
- Khandelwal, P.K., "Detection of Failure Controlling Flaws By Photoacoustic Microscopy (PAM) in Silicon Nitride," Nondestructive Testing High Performance Ceramics, A. Vary, and J. Snyder, eds., American Ceramics Society, Westerville, OH, 1987, pp. 183-197.
- Khuri-Yakub, B.T., Kino, G.S., and Evans, A.G., "Acoustic Surface Wave Measurements of Surface Cracks in Ceramics," J. Amer. Ceram. Soc., vol. 63, no. 1-2, 1980, pp. 65-71.
- Khuri-Yakub, B.T., et al., "Nondestructive Evaluation of Ceramics," D.O. Thompson and D.E. Chimenti, eds., Review of Progress in Quantitative Nondestructive Evaluation, Vol. 1, Plenum Press, New York, 1982, pp. 601-606.

- Khuri-Yakub, B.T., et al., "Nondestructive Evaluation of Composite Materials Using Acoustic Microscopy," Review of Progress in Quantitative Nondestructive Evaluation, Vol. 5B., D.O. Thompson, and D.E. Chimenti, eds., New York, NY, Plenum Press, 1985, pp. 1093-1098.
- Kingery, W.D., Bowen, H.K., and Uhlmann, D.R., Introduction to Ceramics, 2nd edition, John Wiley & Sons, New York, 1976.
- Kinney, J.H., et al., "Nondestructive Imaging of Materials Microstructures using X-ray Tomographic Microscopy," Advanced Tomographic Imaging Methods for the Analysis of Materials, J.L. Ackerman and W.A. Ellingson, eds., Materials Research Society, MRS Symp. Proc. Vol. 217, 1990, pp. 81-95.
- Kinney, J.H., et al., "X-ray Tomographic Microscopy for Nondestructive Characterization of Composites," Review of Progress in Quantitative Nondestructive Evaluation, Vol. 10A, D.O. Thompson and D.E. Chimenti, eds., Plenum, 1991.
- Klima, S.J.; Baaklini, G.Y.; and Abel, P.B., "Nondestructive Evaluation of Structural Ceramics," NASA TM-88978, 1986.
- Klima, S.J.; et al., "Ultrasonic Velocity for Estimating Density of Structural Ceramics," NASA TM-82765, 1981.
- Kress, J.W., and Feldkamp, L.A., "X-ray Tomography Applied to NDE of Ceramics," ASME Paper 83-GT-206, Mar. 1983.
- Krestel, E., ed.: Imaging Systems for Medical Diagnostics. Siemens Aktiengesellschaft Co., Berlin, 1990.
- Kropas, C.V., Moran, T.J., and Yancey, R.N., "Effect of Composition on Density Measurement by X-ray Computed Tomography," Mater. Aval. April 1991, pp. 487-490.
- Lapp, R.E. and Andrews, H.L., Nuclear Radiation Physics, 3rd edition Prentice-Hall, Inc., Englewood Cliffs, NJ, 1963.
- Lemons, P. and Quate, C., "The Acoustic Microscope," Physical Acoustics: Principles and Methods, Vol. XIV, W. Mason, ed., Academic Press, 1979, pp. 1-92.
- London, B., Yancey, R.N., and Smith, J.A., "High-Resolution X-ray Computed Tomography of Composite Materials," Materials Evaluation, Vol. 48, No. 5, May 1990, pp. 604-608, 628.

- Macovsky, A., Medical Imaging Systems, Prentice-Hall, Inc., Englewood Cliffs, NJ, 1983.
- Mah, T., Mendirata, M.G., Katz, A.P., and Mazdiasni, K.S., "Recent Developments in Fiber-Reinforced High-Temperature Ceramic Composites," American Ceramic Society Bulletin, Vol. 66, No. 2, Feb. 1987, pp. 304-308, 317.
- McCauley, J.W., "Materials Testing in the 21st Century," Nondestructive Testing of High-Performance Ceramics, A. Vary, and J. Snyder, eds., American Ceramic Society, Westerville, OH, 1987, pp. 1-18.
- McIntire, P. and Bryant, L.E., eds., "Radiography and Radiation Testing," Nondestructive Testing Handbook, Vol. 3, American Society for Nondestructive Testing, Columbus, OH, 1985.
- McIntire, P., Birks, A.S., and Green, R.E., Jr., eds., Ultrasonic Testing, Nondestructive Testing Handbook, Vol. 7, 2nd ed., American Society for Nondestructive Testing, Columbus, OH, 1991.
- Newton, T.H. and Potts, D.G., eds., Radiology of the Skull and Brain: Technical Aspects of Computed Tomography, Vol. 5, The C.V. Mosby Company, St. Louis, 1987.
- Nikoonahad, M., "Reflection Acoustic Microscopy for Industrial NDE," Research Techniques in Nondestructive Testing, Vol. 7, R.S., Sharpe, ed., Academic Press, London, 1984, pp. 217-257.
- Nishida, K., "Silicon Nitride," The Development of Structural Fine Ceramics in Japan, The Japan Industrial and Technological Bulletin, Japan External Trade Organization, Tokyo, 1983, pp. 21-24.
- Oppenheim, A.V. and Schafer, R.W., Digital Signal Processing, Prentice-Hall, Inc., Englewood Cliffs, NJ, 1975.
- Parish, R.W., "High Resolution Radiography in the Aero-Engine Industry" Non-destructive Inspection Methods for Propulsion Systems and Components. AGARD-LS-L03 (Advisory Group for Aerospace Research and Development, Neuilly-sur-seine, France, 1979. (Avail. NTIS AD-A069901).
- Pfeiler, M., Marhoff, P., and Koch, R., "Effects of X-Ray Physics and Technology in Digital Radiography" Electromedica, vol. 53, no. 2, 1985, pp. 50-17.

Pratt, W.K., Digital Image Processing, John Wiley & Sons, New York, 1978.

Pullan, B.R., Ritchings, R.T., and Isherwood, I., "High-Resolution X-ray Computed Tomography Attenuation Values," Radiography of the Skull and Brain: Technical Aspects of Computed Tomography, Vol. 5, T.H. Newton, and D.G. Potts, eds., C.V. Mosby, St. Louis, MO, 1981, pp. 3904-3917.

Radiological Health Handbook, compiled and edited by the Bureau of Radiological Health and the Training Institute Environmental Control Administration, U.S. Government Printing Office, 1970.

Radon, J., "On the Determination of Functions from their Integrals Along Certain Manifolds," *Berichte Sachsische Akademie der Wissenschaften*, Leipzig, Math.-Phys. Kl., Vol. 69, 1917, pp. 262-267.

Rice, R.W., et al., Ceramics for High Performance Applications II, J.J. Burke, E.N. Leno, and R.N. Katz, eds., Brook Hill Publishing, 1977, pp. 669-687.

Richerson, D.W., Modern Ceramic Engineering: Properties, Processing, and Use in Design, Marcel Dekker Inc., New York, 1982.

Riederer, S.J., "Digital Radiography," *CRC Crit. Rev. Biom. Eng.*, vol. 12, no. 2, 1985, pp. 163-200.

Rosencwaig, A., "Thermal Wave Imaging," *Science*, vol. 218, no. 4569, 1982, pp. 223-228.

Roth, D.J., Klima, S.J., Kiser, J.D., and Baaklini, G.Y., "Reliability of Void Detection in Structural Ceramics by Use of Scanning Laser Acoustic Microscopy," *Materials Evaluation*, Vol. 44, No. 6, May 1986, pp. 762-769, 761.

Roth, D.J., Generazio, E.R., and Baaklini, G.Y., "Quantitative Void Characterization in Structural Ceramics by Use of Scanning Laser Acoustic Microscopy," *Materials Evaluation*, Vol. 45, No. 9, Aug. 1987, pp. 958-966.

Ruud, C.O. and Green, R.E., Jr., Nondestructive Methods for Material Property Determination, Plenum Press, New York, 1983.

Rzeszutarski, M. and Sones, R.: Class Notes in

- 'Fundamentals of Medical Imaging,' (EBME 410 at Case Western University), 1989.
- Sanders, W.A. and Baaklini, G.Y., "Correlation of Processing and Sintering Variables with the Strength and Radiography of Silicon Nitride," *Advanced Ceramic Materials*, Vol. 3, No. 1, 1988, pp. 88-94.
- Sanders, W.A., Kiser, J.D., and Freedman, M.R., "Slurry-Pressing consolidation of Silicon Nitride," *American Ceramic Society Bulletin*, Vol. 68, No. 10, Oct. 1989, pp. 1836-1841.
- Sawicka, B.D. and Ellingson, W.A., "Photon CT Scanning of Advanced Ceramic Materials," AECL-9384, Chalk River Nuclear Laboratories, Chalk River, Ontario, February 1987.
- Sawicka, B.D. and Palmer, B.J.F., "Density Gradients in Ceramic Pellets Measured by Computed Tomography," AECL-9261, Chalk River Nuclear Laboratories, Chalk River, Ontario, July 1986.
- Shepp, L.A., Computed Tomography, American Mathematical Society, Providence, RI, 1983.
- Simon, J.C., Haralick, R.M., and Reidel, D., Digital Image Processing, Publishing Company, Boston, 1980.
- Singh, J.P., "Effect of Flaws on the Fracture Behavior of Structural Ceramics: A Review," *Adv. Ceram. Mater.*, vol. 3, no. 1, 1988, pp. 18-27.
- Smathers, R.L.; and Brody, W.R., "Digital Radiography: Current and Future Trends," *Br. J. Radio.*, vol. 58, no. 68,
- Snell, A.H., ed., Nuclear Instruments and Their Uses, Vol. 1, John Wiley & Sons, Inc., New York, 1962. 1985, pp. 285-307, 1985.
- Stephens, J.R., "Hitemp Program Overview," *HITEMP Review* 1990, NASA CP-10051, 1990, pp. 1-1 to 1-23.
- Storm, E. and Israel, H.I., "Photon Cross sections from 1 keV to 100 MeV for Elements Z=1 to Z=100," Nuclear Data Tables Sect. A7, 565-681, 1970. (Also, LA-3753).
- "Structural Ceramics," NASA CP-2427, 1986.

- Tapiovaara, M.J., and Wagner, R.F., "SNR and DQE Analysis of Broad Spectrum X-ray Imaging," *Phys. Med. Biol.*, vol. 30, no. 6, 1985, pp. 519-529.
- Tittmann, B.R. et al., "Surface Wave Scattering from Elliptical Cracks for Failure Prediction," *J. App. Phys.*, vol. 51, no. 1, 1980, pp. 142-150.
- Vary, A., "Correlations Among Ultrasonic Propagation Factors and Fracture Toughness Properties of Metallic Materials," *Materials Evaluation*, Vol. 36, No. 7, 1978, pp. 55-64.
- Vary, A. and Klima, S.J., "Nondestructive Techniques for Characterizing Mechanical Properties of Structural Materials - An Overview," ASME Paper 86-GT-75, June 1986 (Also, NASA TM-87203).
- Vary, A., "Concepts for Intercorrelating Ultrasonic Attenuation, Microstructure, and Fracture Toughness in Polycrystalline Solids," *Materials Evaluation*, Vol. 46, No. 5, May 1988, pp. 642-649.
- Vary, A., "NDE Standards for High Temperature Materials," NASA TM-103761, 1991a.
- Vary, A. and Klima, S.J., "NDE of Ceramics and Ceramic Composites," NASA TM-104520, 1991b.
- Yancey, R.N., Klima, S.J., and Smith, J.A., "High Resolution Computed Tomography of Modern Ceramics," *Proceeding of the Topical Conference on Nondestructive Evaluation of Modern Ceramics*, sponsored by the American Society for Nondestructive Testing and the American Ceramic Society, Columbus, OH, July 1990, pp. 126-130.
- Yancey, R.N., Baaklini, G.Y., and Klima, S.J., "NDE of Advanced Turbine Engine Components and Materials by Computed Tomography," ASME Paper 91-GT-287, 1991.
- Yuhas, D.E., McGraw, T.E., and Kessler, L.W., "Scanning Laser Acoustic Microscope Visualization of Solid Inclusions in Silicon Nitride," *Proceedings of the DARPA/AFML Review of Progress in Quantitative Nondestructive Evaluation*, D.O. Thompson, ed., AFWAL-TR-80-4078, 1979, pp. 683-690.
- Zatz, L.M., "Basic Principles of Computed Tomography Scanning," Radiology of the Skull and Brain: Technical Aspects of Computed Tomography, T.H. Newton, and D.G. Potts, Vol. 5, C.V. Mosby, St. Louis, MO, 1981, pp. 3853-3876.

APPENDIX A

SLURRY-PRESSING OF NITRIDES

Slurry-pressing is used because a more homogeneous and dense microstructure with smaller critical flaws can be produced (Freedman and Millard 1986; Hurst and Dutta 1987). Figure A.1 shows the slurry processing flow chart. Table A.1 shows the slurry sieved characteristics. Agglomerates are removed from the ethanolic slurry of silicon nitride powder before vacuum drying. After milling for 100 hours, agglomerates and milling debris greater than 10 μm are removed. NH_4OH are added for PH slurry adjustments during another 100 hour grinding. Then the slurry is compacted between filter paper discs sandwiched between porous stainless steel disks. The solid is contained between the filter papers and the liquid escapes through the porous steel disks. The nitride disks are dried and sealed in evacuated thin-wall plastic tubing for cold isostatic pressing under 414 MPa.

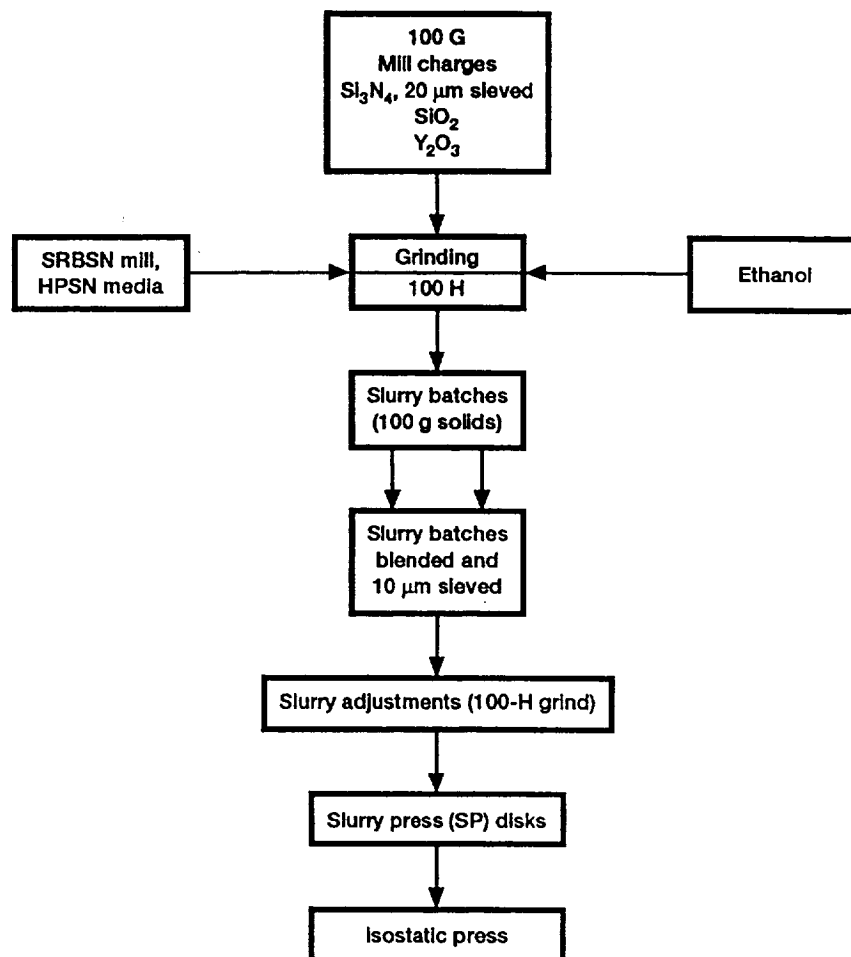


Figure A.1.—Processing of $\text{Si}_3\text{N}_4\text{-SiO}_2\text{-Y}_2\text{O}_3$ slurry (modified from Sanders et.al. 1989).

TABLE A.1—CHARACTERIZATION OF SILICON NITRIDE, OXIDE, AND SLURRY SANDERS (Sanders et al. 1989).

| Material | Source | Manufac- terer's designa- tion | Purity, percent | Specific surface area, m ² /g | X-ray diffraction analysis, percent | | | Chemical analysis | | |
|--------------------------------------|--------------------|---|--------------------|---|--|---------|------------|-------------------|-----------------|--|
| | | | | | α | β | Free Si | Oxygen, wt % | Carbon, wt % | Spectrographic analysis, ppm |
| Si ₃ N ₄ | AME | High purity | 99.5 | 3.72 | 82.9 | 16.4 | 0.7 | 0.71 | 0.08 | 980 Al, 110 Ca, 1900 Fe, 500 Mo, 220 Ni, 210 Pb, 170 Ti, 470 V |
| SiO ₂ | Apache Chemical | 6846 | 99.99 | 166 | --- | --- | --- | --- | .16 | 220 Al, 150 Ca, 30 Cr, 50 Cu, 50 Fe, 130 Mg, 90 Mn, 340 Na, 40 Ti |
| Y ₂ O ₃ | Molycorp | 5600 | 99.9 | 7.5 | --- | --- | --- | --- | .11 | 60 Cu, 60 Mg, 40 rare earth oxides |
| Slurry ^a (100-h grind) | ----- | ----- | ----- | 25.1 | --- | --- | --- | 4.76 | .11 | 1240 Al, 90 Ca, 1970 Fe, 510 Mo, 450 Ni, 120 Ti, 290 V, 5.5 wt % Y |
| Slurry (300-h grind) | ----- | ----- | ----- | 22.6 | --- | --- | --- | --- | --- | ----- |

^aGround slurry composition, 87.8 Si₃N₄ - 5.8 SiO₂ - 6.4 Y₂O₃, by weight percent; 88.4 Si₃N₄ - 12.8 SiO₂ - 3.8 Y₂O₃, by mole percent.

APPENDIX B

SINTERING OF NITRIDES

Sintering is technically the densification of a ceramic green compact. During sintering the volume of pores is reduced by the growth between adjacent particles. During sintering grain size and shape changes occur and pore size and shape are modified. Detailed information on ceramic sintering mechanisms can be found in Kingery et al. (1976).

The isostatically pressed nitride disks are sintered in a tungsten cup inside a water-cooled double-wall furnace. Sintering temperatures are monitored and controlled with W-5Re/W-26Re thermocouples. Disks are sintered at 2140 C for 3 hours. Heating from room temperature to 2140 C is done at a linear rate lasting 45 minutes. Nitrogen overpressure of 5 Mpa is used.

APPENDIX C

FABRICATION OF INJECTION-MOLDED SINTERED SILICON NITRIDE BLADE

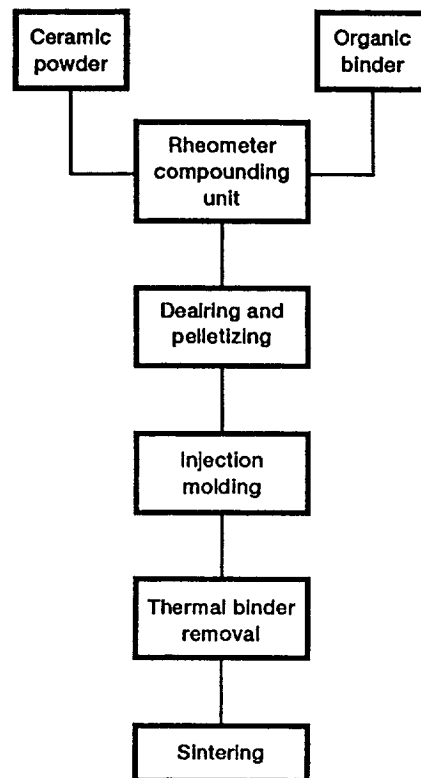


Figure C.1.—Fabrication of injection-molded sintered silicon nitride turbine blade (CATE 1981).

APPENDIX D

FABRICATION OF SCS-6 FIBER REINFORCED MMC ROD, RING, AND ROTOR

The MMC rod, ring and rotor are Pratt and Whitney hardware. Schematic representations of the fabrication procedures of the rod , ring and rotor follow in figures D.1, D.2, and D.3, respectively.

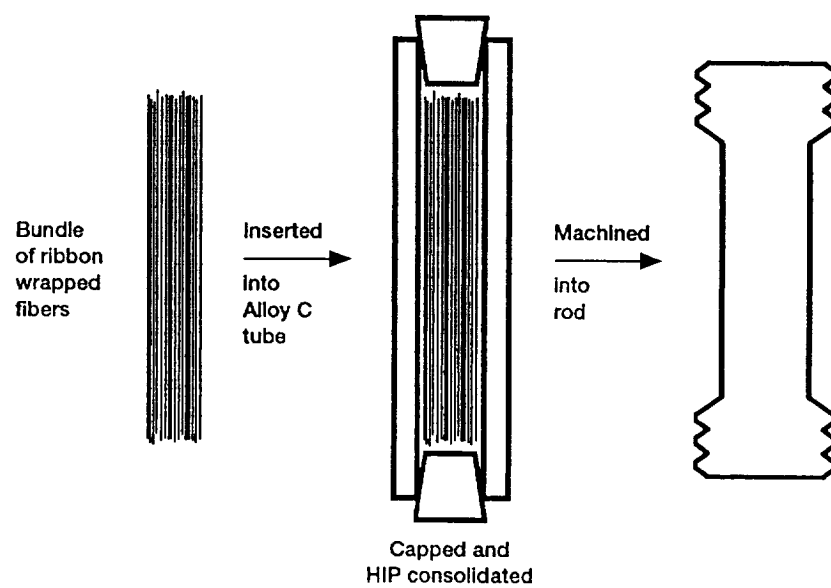


Figure D.1.—Fabrication of fiber reinforced MMC rod.

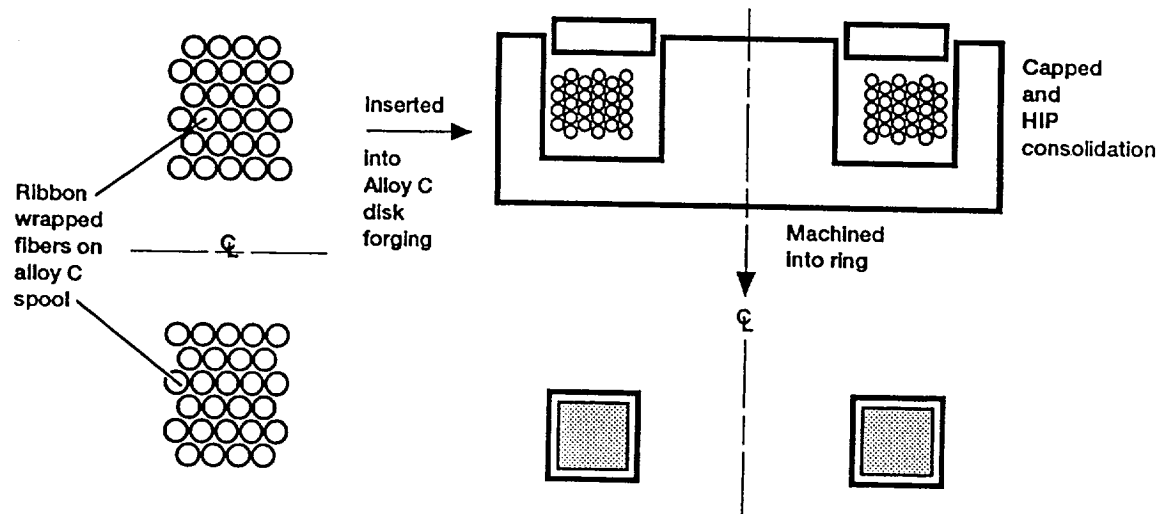


Figure D.2.—Fabrication of fiber reinforced MMC ring.

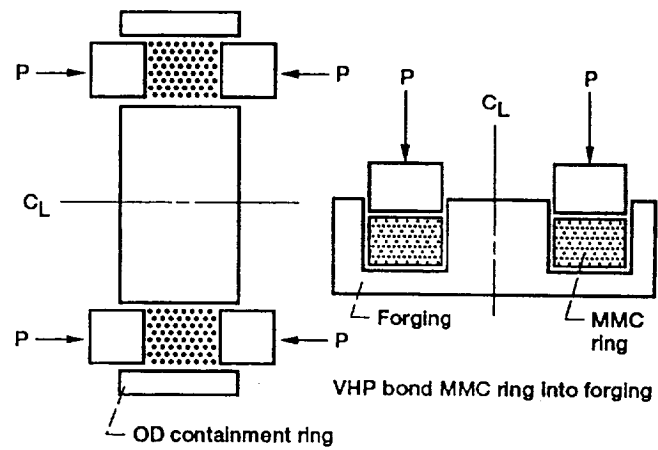


Figure D.3.—Fabrication of the integrally bladed MMC rotor.

APPENDIX E

X-RAY RADIOGRAPHY RELATED TOPICS

Table E.1 shows the electromagnetic spectrum. Table E.2 lists the computed total mass attenuation coefficients for Si_3N_4 , SiC , and Ti_3Al . Table E.3 lists the total mass attenuation coefficients for W , Si_3N_4 , SiC , and air.

| REPORT DOCUMENTATION PAGE | | | Form Approved OMB No. 0704-0188 | |
|--|--|--|------------------------------------|--|
| Public reporting burden for this collection of information is estimated to average 1 hour per response, including the time for reviewing instructions, searching existing data sources, gathering and maintaining the data needed, and completing and reviewing the collection of information. Send comments regarding this burden estimate or any other aspect of this collection of information, including suggestions for reducing this burden, to Washington Headquarters Services, Directorate for Information Operations and Reports, 1215 Jefferson Davis Highway, Suite 1204, Arlington, VA 22202-4302, and to the Office of Management and Budget, Paperwork Reduction Project (0704-0188), Washington, DC 20503 | | | | |
| 1. AGENCY USE ONLY (Leave blank) | 2. REPORT DATE March 1992 | 3. REPORT TYPE AND DATES COVERED Technical Memorandum | | |
| 4. TITLE AND SUBTITLE X-Ray Attenuation Measurements for High-Temperature Materials Characterization and In-Situ Monitoring of Damage Accumulation | | 5. FUNDING NUMBERS WU-510-01-50 | | |
| 6. AUTHOR(S) George Y. Baaklini | | | | |
| 7. PERFORMING ORGANIZATION NAME(S) AND ADDRESS(ES) National Aeronautics and Space Administration Lewis Research Center Cleveland, Ohio 44135-3191 | | 8. PERFORMING ORGANIZATION REPORT NUMBER E-6652 | | |
| 9. SPONSORING/MONITORING AGENCY NAMES(S) AND ADDRESS(ES) National Aeronautics and Space Administration Washington, D.C. 20546-0001 | | 10. SPONSORING/MONITORING AGENCY REPORT NUMBER NASA TM-105577 | | |
| 11. SUPPLEMENTARY NOTES Report was submitted as a dissertation in partial fulfillment of the requirements for the degree of Doctor of Engineering, Cleveland State University, Cleveland, Ohio 44115 in 1991. Responsible person, George Y. Baaklini, (216) 433-6016. | | | | |
| 12a. DISTRIBUTION/AVAILABILITY STATEMENT Unclassified - Unlimited Subject Categories 38 and 24 | | 12b. DISTRIBUTION CODE | | |
| 13. ABSTRACT (Maximum 200 words) The scope of this dissertation is to develop and apply x-ray attenuation measurement systems that are capable of 1) characterizing density variations in high-temperature materials, e.g., monolithic ceramics, ceramic and intermetallic matrix composites and 2) noninvasively monitoring damage accumulation and failure sequences in ceramic matrix composites under room temperature tensile testing. This dissertation results in the development of 1) a point scan digital radiography system and 2) an in-situ x-ray material testing system. The former is used to characterize silicon carbide and silicon nitride specimens and the latter is used to image the failure behavior of silicon carbide fiber reinforced reaction bonded silicon nitride matrix composites. Further, state of the art x-ray computed tomography is investigated to determine its capabilities and limitations in characterizing density variations of subscale engine components, e.g., a silicon carbide rotor, a silicon nitride blade, and a silicon carbide fiber reinforced beta titanium matrix rod, rotor, and ring. Microfocus radiography, conventional radiography, scanning acoustic microscopy, and metallography are used to substantiate the x-ray computed tomography findings. Point scan digital radiography is a viable technique for characterizing density variations in monolithic ceramic specimens. But it is very limited and time consuming in characterizing ceramic matrix composites. Precise x-ray attenuation measurements, reflecting minute density variations, are achieved by photon counting and by using micro collimators at the source and the detector. X-ray computed tomography is found to be a unique x-ray attenuation measurement technique capable of providing cross sectional spatial density information in monolithic ceramics and metal matrix composites. X-ray computed tomography is proven to accelerate generic composite component development. Radiographic evaluation before, during and after loading shows the effect of preexisting volume flaws on the fracture behavior of composites. Results from one-ply, three-ply, five-ply and eight-ply ceramic composite specimens, shows that x-ray film radiography can monitor damage accumulation during tensile loading. Matrix cracking, fiber-matrix debonding, fiber bridging, and fiber pullout are imaged throughout the tensile loading of the specimens. Further in-situ film radiography is found to be a practical technique for estimating interfacial shear strength between the silicon carbide fibers and the reaction bonded silicon nitride matrix. It is concluded that pre-test, in-situ, and post-test x-ray imaging can provide for greater understanding of ceramic matrix composite mechanical behavior. | | | | |
| 14. SUBJECT TERMS X-radiography; NDE; Ultrasonics; X-tomography; In-situ monitoring; Damage accumulation; Digital radiography; Composites; Ceramics; CMC; MMC* | | | 15. NUMBER OF PAGES 284 | |
| | | | 16. PRICE CODE A13 | |
| 17. SECURITY CLASSIFICATION OF REPORT Unclassified | 18. SECURITY CLASSIFICATION OF THIS PAGE Unclassified | 19. SECURITY CLASSIFICATION OF ABSTRACT Unclassified | 20. LIMITATION OF ABSTRACT | |